NTNU
Norwegian University of
Science and Technology

Modelling and Analysis of a Floating Bridge

Eirik Breisnes Vika

Marine Technology

Submission date:	June 2018
Supervisor:	Bernt Johan Leira, IMT
Co-supervisor:	Xu Xiang, Statens vegvesen

Norwegian University of Science and Technology
Department of Marine Technology

NTNU
Norwegian University of Science and Technology
Department of Marine Technology

Master Thesis, Spring 2018
for
Stud. Techn. Eirik Breisnes Vika

Modelling and Analysis of a Floating Bridge

Modellering og Analyse av en Flytebro

Floating bridges are relevant for crossing of very deep and wide lakes or fjord systems. In order to compute the static and dynamic response of these bridges, the joint properties of the whole hydro-elastic system need to be accounted for. The objective of the present project is to outline methods for response analysis and illustrate the calculation procedure for a particular example structure.

The following subjects are to be addressed as part of this work:

1. Give an introduction to the Ferry Free E39 project and some of the proposed floating bridge concepts for this project. A few examples of existing floating bridges should also be presented. Similarities and differences between the different bridges are to be highlighted.

2. Important loads which are acting on such bridges are to be described and associated structural models are discussed. Corresponding methods for both static and dynamic response analysis are elaborated and relevant numerical algorithms are described.

3. A specific example of a marine bridge structure is to be selected for the purpose of illustrate the modelling aspects and the calculation procedures. A static, eigenmode and dynamic analysis are performed. The results obtained in the eigenmode analysis are compared with results obtained by project groups for the chosen bridge concept. The dynamic analysis should be performed for regular waves and characteristics in the global response described. The selection of the example structure is to be made based on discussion with the supervisor.

The work scope may prove to be larger than initially anticipated. Subject to approval from the supervisor, topics may be deleted from the list above or reduced in extent.

In the thesis the candidate shall present his personal contribution to the resolution of problems within the scope of the thesis work. Theories and conclusions should be based on mathematical derivations and/or logic reasoning identifying the various steps in the deduction.

The candidate should utilise the existing possibilities for obtaining relevant literature.

The thesis should be organised in a rational manner to give a clear exposition of results, assessments, and conclusions. The text should be brief and to the point, with a clear language. Telegraphic language should be avoided.

The thesis shall contain the following elements: A text defining the scope, preface, list of contents, summary, main body of thesis, conclusions with recommendations for further work, list of symbols and acronyms, references and (optional) appendices. All figures, tables and equations shall be numbered.

The supervisor may require that the candidate, in an early stage of the work, presents a written plan for the completion of the work. The original contribution of the candidate and material taken from other sources shall be clearly defined. Work from other sources shall be properly referenced using an acknowledged referencing system.

Supervisor: Bernt J. Leira

Professor Bernt J. Leira

Co-supervisor: Xu Xiang, Statens vegvesen

Start-up: January 15th, 2018

Deadline: June 25th, 2018

Preface

This master thesis in marine structural engineering is written at the Department of Marine Technology at the Norwegian University of Science and Technology. The work was carried out during the spring semester of 2018.

The topic of this thesis is modelling and analysis of a straight floating bridge concept for the Bjørnafjorden crossing, which was developed in 2016 on behalf of the NPRA as a part of the Ferry Free E39 project. The report also contains an introduction to this project and a presentation of other bridge concepts and existing floating bridges. Parts of the theory and the background on floating bridges have been modified and extended from my work on the project thesis, which was carried out in the fall semester of 2017.

I would like to thank my supervisor Professor Bernt J. Leira and co-supervisor Xu Xiang from the National Public Road Administration for guidance and help during the thesis work. I would also like to express great appreciation to PhD Candidate Thomas Hansen Viuff and Postdoctoral Fellow Zhengshun Cheng for their time and effort on helping me troubleshoot my bridge model regards to the inconsistencies in the eigenvalue analysis. This process turned out to be time-consuming. Finally, I would like to thank Erlend Flatøy for proofreading, and my friends and fellow students at marine technology for five memorable years in Trondheim.

Bergen, June 24, 2018

Eirik B. Vika

Eirik B. Vika

Summary

The Norwegian National Public Road Administration is working on a project to improve the coastal road E39, connecting the cities along the west coast of Norway. Today, this road has seven ferry crossings which are to be replaced by permanent connections, to a total expected cost of 340 billion NOK.

Several of these fjords are wider and deeper than what existing designs can manage, such that new technology needs to be developed. For some of the fjord crossings, floating bridge concepts have been developed and concluded to be feasible solutions. For the about 4500 meters wide Bjørnafjorden, south of Bergen, there are two floating bridge concepts which are in the process of being further assessed.

One of these concepts is a straight bridge, laterally supported by pre-tensioned mooring lines. This concept was modelled in the software SIMO-RIFLEX, where a static, eigenvalue and dynamic analysis were performed in order to illustrate modelling aspects and calculation procedures. Panel models of the pontoon were modelled in GeniE and imported into HydroD where hydrodynamic analyses were carried out in Wadam.

From the eigenvalue analysis, a significant limitation was identified in the eigenvalue calculation codes in SIMO-RIFLEX, as the catenary mooring lines were not properly accounted for. Therefore, a second model was made where the mooring system was replaced by a linearised implementation. For this model, the eigen periods and mode shapes were coinciding well with those obtained by the NPRA. The first 30 eigen periods were differing with a mean value of 3.9 % when only the infinite-frequency added mass matrix was considered. By updating the added mass for a selected set of modes, differences of less than about 2 % were found.

The eigenvalue calculations revealed several modes that can be triggered by environmental loads. Laterally dominated modes at high periods with negligible damping, which can be important for the response in slowly varying wind, and laterally dominated modes close to the peak period for the 100-year wind waves, were identified. Additionally, modes dominated by pontoon motions along the bridge girder close to this period were found, possibly important for the dynamic weak axis bending moments in the high bridge.

From the dynamic analyses in regular waves, response patterns related to the identified modes were present when the bridge was subjected to waves from different directions, respectively. The maximum weak axis bending moment in the bridge girder for the conditions examined was found in the high bridge for a response pattern related to the mentioned modes dominated by pontoon motions along the bridge girder. This moment had a magnitude of $9.1 \cdot 10^5$ kNm, where the dynamic moment only contributed with 15 %. The results from the analyses performed were therefore seen to give indications on possible room for girder length to girder height ratio optimisation and should be further assessed based on analyses performed for the actual environmental conditions in the fjord.

Sammendrag

Statens vegvesen har startet et prosjekt for å forbedre Europavei E39, veien som knytter sammen byene langs vestkysten av Norge. I dag har E39 syv fergekrysninger, og målet er at disse skal erstattes av faste forbindelser, til en total forventet kostnad på 340 milliarder kroner.

Flere av disse fjordene er bredere og dypere til at eksisterende bro- eller tunnelløsninger kan brukes. Derfor må ny teknologi utvikles. For noen av fjordkrysningene har flytebro-konsepter blitt utviklet og fastslått til å være mulige løsninger. Statens vegvesen har nå to flytebro-konsepter som de holder på å videreutvikle for den omtrent 4500 meter lange krysningen over Bjørnafjorden.

Et av disse konseptene er en rett flytebro som bruker forspente forankringsliner til å sikre tilstrekkelig tverrgående stivhet. Dette konseptet ble modellert i programvaren SIMO-RIFLEX, hvor en statisk-, egenverdi- og dynamisk analyse ble utført for å illustrere modelleringsaspekter og beregningsmetoder. Panelmodeller av pongtongen ble modellert i GeniE og importert til HydroD hvor hydrodynamiske analyser ble utført i modulen Wadam.

Fra egenverdi-analysen ble det funnet en betydelig begrensning i beregningsalgoritmene for egenverdi-analyse i SIMO-RIFLEX, da forankringslinene ikke ble korrekt inkludert. Det ble derfor laget en ny modell hvor forankringssystemet ble linearisert. Denne modellen ga egenperioder og svingeformer som stemte godt overens med resultatene til Statens vegvesen. De første 30 egenperiodene hadde et gjennomsnittlig avvik på 3,9 % ved å kun inkludere tilleggsmassen for uendelig frekvens. Differanser på mindre enn omlag 2 % ble oppnådd ved å inkludere den korrekte tilleggsmassen for noen utvalgte moder.

Egenverdi-analysen identifiserte flere svingeformer som kan trigges av miljølaster. Lateralt dominerte svingeformer ved høye perioder hvor dempningen er neglisjerbar, som kan være viktige for responsen i langsomt varierende vind, og lateralt dominerte svingeformer nær toppperioden for 100-års vindbølger, ble identifisert. I tillegg ble det funnet svingeformer dominert av pongtongbevegelser langs brobjelken nær denne perioden, som muligens kan føre til store bøyemomenter om svak akse i høybroen.

Fra de dynamiske analysene i regulære bølger var responsmønstre relatert til de identifiserte svingeformene tilstede da broen ble utsatt for bølger fra ulike retninger. Det maksimale bøyemomentet i brobjelken om svak akse ble funnet i høybroen for et responsmønster relatert til svingeformene som var dominert av pongtongbevegelser langs brobjelken. Dette momentet hadde en størrelse på $9{,}1 \cdot 10^5$ kNm, hvor det dynamiske momentet kun bidro med 15 %. Resultatene fra analysene som ble utført ga derfor indikasjoner på at avstanden mellom pongtongene burde reduseres. Dette bør vurderes ytterligere ved å kjøre analyser hvor de faktiske sjø- og vindforholdene i fjorden inkluderes.

Contents

List of Figures

List of Tables

Nomenclature

Roman Letters

A	Cross sectional area
a_i	Acceleration in i-direction
A_{kj}	Added mass in k-direction due to acceleration in the j-direction
A_{wp}	Water plane area
B_{kj}	Damping in k-direction due to motion in the j-direction
C	Shape coefficient
C_D	Drag coefficient
C_L	Lift coefficient
D	Characteristic cross-sectional length
f	Eigenfrequency
F_k	Force in k-direction
F_m	Current force
F_q	Gust force
g	Gravitational acceleration
H	Projected area of structure
H	Wave height
h	Water depth
H_s	Significant wave height
I_u	Turbulence intensity
I_{44}	Roll area moment of inertia
I_{55}	Pitch area moment of inertia

k	Wave number
q	Distributed force
s	Span length
T	Eigen period
T	Wave period
T_p	Peak period
V_m	Time-averaged wind velocity

Matrices and Vectors

$\mathbf{A}$	Added mass matrix
$\mathbf{A}_\infty$	Infinite-frequency added mass matrix
$\mathbf{h}$	Retardation function matrix
$\mathbf{i}$	Unit vector along x-axis
$\mathbf{j}$	Unit vector along y-axis
$\mathbf{K}_I$	Incremental stiffness matrix
$\mathbf{K}$	Global stiffness matrix
$\mathbf{k}$	Unit vector along z-axis
$\mathbf{M}$	Mass matrix
$\mathbf{Q}$	External load vector
$\mathbf{R}$	Global load vector
$\mathbf{r}$	Nodal displacement vector

Greek Letters

α	Mass proportionality coefficient
α	Wind direction angle
β	Stiffness proportionality coefficient
λ	Wave length
ω	Circular frequency
ω	Eigenfrequency
ϕ	Eigenvector
ϕ	Velocity potential
ρ	Sea water density

ρ_a	Air density
τ	Time lag integration variable
ξ	Critical damping ratio
ζ	Wave elevation
ζ_a	Wave amplitude

Abbreviations

COB	Centre of Bouyancy
COG	Centre of Gravity
DNV	Det Norske Veritas
Jonswap	Joint North Sea Wave Project
NPRA	National Public Road Administration
TLP	Tension Leg Platform
Wadam	Wave Analysis by Diffraction And Morison theory

Chapter 1

Introduction

1.1 Motivation and Background

European route E39 is a road starting just south of Trondheim, running along the west coast of Norway, all the way to Kristiansand. The total distance of the route today is around 1100 km, including 7 ferry connections, and has the corresponding travel time of 21 hours. A map of the road, with its fjord crossings marked, is shown in figure 1.1.

The Ferry Free E39 project is led by the National Public Road Administration (NPRA) and has the purpose of improving this road, in terms of replacing the ferry connections by tunnels, cable-stayed bridges, floating bridges or submerged tunnels and upgrading parts of the existing road sections on land [1]. By these measures, the goal is to reduce the travel time to around 11 hours. Moreover, the ambitions of the supreme legislature of Norway is that the project shall be finished by 2035, and the total project is expected to have a cost of 340 billion NOK.

Bjørnafjorden, south of Bergen, is one of the ferry connections which shall be replaced in this project. The fjord has a width of about 4500 metres and a maximum depth of 580 metres at the location planned for the crossing [2]. In comparison, the current world's longest floating bridge has a length of 2350 metres, crossing Lake Washington in the USA [3]. Several concepts have been considered for the Bjørnafjorden crossing, i.e. a submerged floating bridge concept, cable-stayed bridges with towers on TLP foundations concept and floating bridge concepts. Today, two concepts are chosen for further assessment by the NPRA: a straight floating bridge which is laterally supported by mooring lines and a curved end-anchored floating bridge [4]. The straight bridge concept is chosen as a basis for the work performed in this thesis.

Figure 1.1: Map of the Norwegian part of E39 and its fjord crossings [5]

1.2 Objective

The objective of the thesis work is to perform global response analyses on a floating bridge model, which is to be modelled as a coupled SIMO-RIFLEX model in SIMA, in order to illustrate modelling aspects and calculation procedures. The analyses to be included are a static analysis due to permanent loads, an eigenvalue analysis and dynamic analyses in regular waves. The results of the eigenvalue analysis are to be compared with the results obtained on behalf of the NPRA.

1.3 Limitations

Several limitations were introduced in the thesis work and can be divided into three main categories: simplifications done in modelling, limitations in the analyses performed and software limitations.

In the first category, it should be mentioned that the vertical curvature of the bridge girder was not included and the tower in the cable-stayed bridge was simplified. For the pontoons only first order forces due to wave loading were included, hence no second order nor viscous forces were considered.

The dynamic analyses performed were limited to harmonic wave loading, meaning that realistic implementations of the environmental loads were not done.

In the last category, it should be mentioned that the catenary mooring system was not properly accounted for in the eigenvalue calculation codes in SIMO-RIFLEX. These codes did also not consider frequency dependent added mass.

1.4 Structure of the Report

- Chapter 1: Introduction to the Ferry Free E39 project, objective and limitations
- Chapter 2: Characteristics of floating bridges and examples of floating bridges, both concepts for the Ferry Free E39 project and existing bridges
- Chapter 3: Presenting the bridge concept used as a basis for the bridge model
- Chapter 4: Describing the main steps done in the modelling of the floating bridge and relevant simplifications and assumptions. The modelling included making a panel model of the pontoon in GeniE, running hydrodynamic analyses on this model in Wadam in HydroD, alterations of hydrodynamic results in SIMO and modelling the bridge structure and mooring lines in RIFLEX.
- Chapter 5: Presenting and discussing results from the hydrodynamic analyses of the pontoon and the results from the static, eigenvalue and dynamic analyses of the complete coupled bridge model in SIMO-RIFLEX
- Chapter 6: Conclusion
- Chapter 7: Recommendations for further work

Chapter 2

Background on Floating Bridges

The advantage of floating bridges is that they can be cost-efficient solutions to lake or fjord crossings where conventional bridges or subsea tunnels are not suited [6]. This can be the case for deep sea, wide crossings or soft bottom conditions.

2.1 Characteristics of Floating Bridges

Floating bridges are bridges where the bridge girder is supported in the vertical direction by floating elements, commonly called pontoons. The pontoons can be placed continuously, where the pontoons are linked directly together, or placed separately.

General considerations for the pontoons are that they should consist of waterproof compartments in order to ensure redundancy in case of accidents, and the material should be suited for the corrosive environment. Furthermore, the pontoons and the bridge itself should be built lightweight and thereby reduce the necessary buoyancy. In this way, the volume of the pontoons can be reduced in order to reduce the environmental loads acting on the bridge [7].

In any case, the bridge girder will be subjected to relatively large lateral loads due to current and waves acting on the pontoons and wind acting on the whole system. Consequently, there are two traditional ways of ensuring satisfying stiffness in the lateral direction: by use of mooring systems or by placing the bridge in a curve.

By use of mooring systems the bridge can be placed straight, with the mooring lines attached directly to the pontoons. The mooring lines are placed in an angle to the sea bottom by use of anchors.

The other main option used by existing bridges is placing the bridge in a curve in the horizontal plane with its two ends as the only connections, hence no use of mooring systems. The curved design enables the bridge girder to carry the lateral loads from wind, currents and waves to its two land abutments as axial forces.

Another challenge by use of floating bridges is that they can be a restriction for marine traffic. Several methods are used to mitigate this problem, such as an elevation of the bridge beam for smaller boats and movable spans or a navigational channel for larger ships.

2.2 Existing Floating Bridges

Throughout the study of floating bridges, bridges of special attributes were sought for. In general, it was found that existing bridges are limited to locations with calm wave conditions. This is not the case for some of the crossings considered for the Ferry-Free E39 project, in which the crossings are significantly wider and with more challenging environmental conditions. A selection of these concepts will be further described in section 2.3.

The following review of existing floating bridges is therefore limited to three bridges: the two and only Norwegian floating bridges and the world's longest floating bridge. These bridges highlight several of the characteristics presented in section 2.1, where the latter mentioned differ significantly from the Norwegian bridges.

2.2.1 Bergøysund Bridge

Bergøysund Bridge was built in 1992 and was the first Norwegian floating bridge, and the world's first permanent floating bridge without any side anchoring [7]. The bridge was a part of the National Public Road Administration's project *Krifast* for a section of the road E39 in the county of *Møre og Romsdal*, where it is one of the mainland connections for the city of Kristiansund. The crossing has a maximum depth of about 320 metres.

The bridge has a total length of 931 metres, a span of 845 metres and is placed in a curve of radius 1300 metres. Furthermore, the bridge has 7 pontoons of high strength lightweight concrete and has a maximum vertical water clearance of 6 metres. From figure 2.1 it can be seen that the superstructure of the bridge consists of tubular steel trusses and pipe junctions.

Figure 2.1: Bergøysund Bridge [8]

2.2.2 Nordhordaland Bridge

The Nordhordaland bridge was opened for traffic in 1994 and became the longest floating bridge in the world without side anchoring [9]. This is a record which still holds since the mentioned bridges are the only permanent floating bridges of the curved end-anchored type. The main reason for this type of end-anchoring was because the existing mooring techniques at the time of construction could not be used, due to the crossing's maximum depth of about 500 metres.

The Norhordaland bridge is also a part of the road E39 and is connecting Bergen- and Meland municipality. In 1994 the bridge replaced the most heavily used ferry service in Norway at the time, which in 1993 carried 1.68 million cars across the fjord [9].

The bridge has a total length of 1615 metres and consists of a cable-stayed bridge and a floating bridge, as can be seen in figure 2.2. The floating bridge has a length of 1246 metres, is placed in a curve with a radius of 1700 metres and has a total of 10 pontoons equally spaced along its length. Its cross section is a steel box, which has a width of 15.9 metres and height of 5.50 metres.

The pontoons are made of lightweight concrete and have a length and width of 42.0 and 20.5 metres, respectively. The heights of the pontoons are in the range of 7.0 to 8.6 metres and differ mainly due to the differences in the span lengths at the respective ends. Furthermore, the bridge can be trimmed by use of solid ballast in the pontoons, whereas each pontoon consists of 9 waterproof compartments, where two neighbouring compartments can be filled with water without endangering the bridge [9].

The high bridge has a length of 369 metres and a maximum span of 99.3 metres, which provides a minimum navigation channel of 32 metres vertical clearance and width of 50 metres [9]. The floating bridge has a vertical clearance of 5.5 metres.

Figure 2.2: Nordhordaland Bridge [10]

2.2.3 Govenor Albert D. Rosellini Bridge

The Governor Albert D. Rosellini Bridge is the world's longest floating bridge, and also the widest, with its length and maximum width of 2350 and 35 metres, respectively [3]. The bridge is crossing Lake Washington, from Medina to Seattle, in the USA, and was opened for traffic in 2016 as a replacement for the 53 years old previous world's longest floating, which was 40 meters shorter. This was done as a consequence of its increasing age, due to two main reasons: its approaches were increasingly vulnerable to earthquakes and the pontoons vulnerable to windstorms [3].

The current bridge has a total of 77 box-shaped concrete pontoons, where 21 of these are longitudinal pontoons and 54 supplementary pontoons. The former pontoons have a weight of about 11 000 tons and length, width and draft of about 110, 23 and 8.5 metres, respectively [3]. These are placed continuously and linked directly together along the bridge, except at the bridge's two ends. The supplementary pontoons have a weight of about 2 700 tons and are attached to the outermost sides of the aforementioned pontoons in order to increase the stability of the structure. These can be seen in figure 2.3. Due to the continuous placements of the longitudinal pontoons, the bridge has one navigational channel at each end in order to allow passage of marine traffic. The highest of these gives a vertical clearance of about 21 metres [3].

Furthermore, the bridge is supported in the lateral direction by 58 mooring lines, where every longitudinal pontoon has at least two cables attached. These are anchored to the up to 61 metres deep lake bottom, leading to mooring line lengths of maximum 300 metres. Despite the small water depth, a floating bridge was considered to be the optimal solution for the crossing, as a result of the lake bottom consisting of an about 61 metres thick layer of soft lake sediments. Conventional fixed bridges were expected to be more expensive, as well as their massive support towers out of character with the surroundings [3].

Figure 2.3: The Governor Albert D. Rosellini Bridge [3]

2.3 Bridge Concepts in the Ferry Free E39 Project

On December 1st, 2017, the ferry crossing replacement project *Rogfast* was signed, as the first of the ferry replacements in the Ferry Free E39 project. *Rogfast* is the name of the Boknafjorden ferry replacement project as shown in figure 1.1. This will be the world's longest and deepest subsea tunnel [11].

The remaining fjord crossing sub-projects are still in the planning or development phase. For some of the crossings existing technology can be used, namely regular subsea tunnels or cable-stayed bridges, but for the deepest and widest crossings new technology needs to be developed. There are mainly four categories of bridge concepts which have been considered for these crossings: cable-stayed bridges, floating bridges, submerged tunnels, cable-stayed bridges on TLP foundations and combinations of these.

The Sognefjorden crossing is considered as the most challenging crossing because of its maximum depth of 1250 metres, width of 3.7 km and its environmental conditions. However, a feasibility study from 2012 concluded that all the mentioned solutions are feasible [5].

2.3.1 Hordfast

Hordfast is the name of the ferry replacement project for the Bjørnafjorden crossing. As already mentioned, Bjørnafjorden is located just south of Bergen and has a maximum depth of around 580 metres and a width of around 4.5 km on the planned site of crossing.

Initially, all the categories of bridge concepts have been considered, but there are now two floating bridge concepts which will be further developed: a straight floating bridge with pre-tensioned lateral mooring lines and a curved floating bridge only connected at its two ends. Both of these are developed on behalf of the NPRA by a project group consisting of COWI, Aas-Jakobsen, Johs Holt and Global Maritime as the main contributing companies.

Curved Bridge Concept

The curved floating bridge concept consists of a cable-stayed bridge at one end and a floating bridge, and has a straight line distance between its abutments of about 4600 metres. The bridge girder is placed in a curve of radius 5000 metres in the horizontal plane, in order to carry lateral loads through arc action [12]. To let larger ships pass, it is planned a cable-stayed bridge with a height of approximately 50 metres and a main span of 490 metres, providing a navigational channel of minimum 400 m x 45 m. The floating part of the bridge consists of 19 identical pontoons with an equal horizontal spacing of 197 m [12]. All pontoons are faced in the same direction.

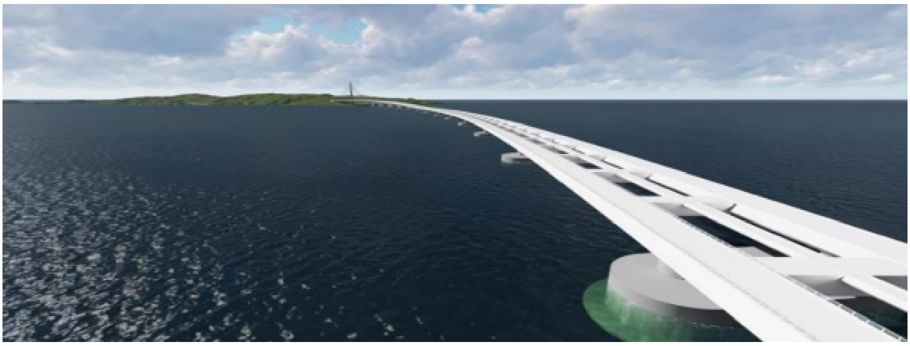

Figure 2.4: Illustration of the end-anchored curved floating bridge concept across Bjørnafjorden [13]

The pontoon is made of lightweight concrete and has a cigar shape, with a length, width and height of 68, 28 and 14 metres, respectively. It has a flange in its bottom in order to increase added mass in heave and is the same pontoon as will be used in the straight bridge alternative. The bridge girder is a Vierendel Beam, consisting of two parallel steel boxes, a smaller steel box where the pedestrian lane is placed, and cross beams [12]. The cross-sections are different in the high bridge and low bridge, as well as the bridge girder being re-enforced at the girder-tower and girder-column intersections. A visual representation of the expected design is illustrated in figure 2.4.

Updated Designs

The straight bridge concept will be used as an example model in the analysis in this thesis and will therefore be described in detail in chapter 4. However, it should be mentioned that according to the NPRA improved versions of both designs presented in this section have been made [4]. The main changes are that the number of pontoons has been doubled and the concrete pontoons have been replaced by steel pontoons. The end-anchored bridge has also been curved in the opposite direction and the bridge girder reduced from a Vierendel Beam to a single steel box. For the side anchored bridge further work have been done regarding the mooring system. An illustration of the updated design on this bridge is shown in figure 2.5. Technical reports have not been made publicly available on the updated designs, consequently, the previous design on the straight bridge concept will be used as a basis for the continued work in this thesis.

Figure 2.5: Illustration of the updated design on the straight bridge concept [13]

Chapter 3

Theory

In this section, important theory regarding global static- and dynamic response analysis of floating bridges will be revised. First, a list of the structural loads will be given, followed by a description of the first five items, including how they can be implemented in the analyses. The remaining items will not be further assessed in this report.

3.1 Structural Loads

The loads acting on a floating bridge can be summarised as:

- Permanent loads
- Traffic loads
- Wind loads
- Wave loads
- Current loads
- Loads due to tidal variations
- Accidental loads
- Marine growth
- Water absorption in concrete
- Other environmental loads (temperature, snow and ice, earthquake, etc.)

3.1.1 Permanent Loads

By permanent loads it is referred to the self-weight of the complete structure and includes the weight of all components, equipment, railings, asphalt, pontoons and permanent ballast.

3.1.2 Traffic Loads

Traffic loads are by nature dynamic but can be simplified as uniformly distributed and concentrated loads as described by Eurocode 1 [14], which is the same set of technical rules as used by the NPRA for the bridge concept to be studied. In the following, a short description of determining the traffic loads according to the load case *Load Model 1 (LM1)* is described. This is the governing load case for elements with influence lengths up to 500 m [14].

The first step is to divide the carriageway into *notional lanes* and *remaining area* according to figure 3.1.

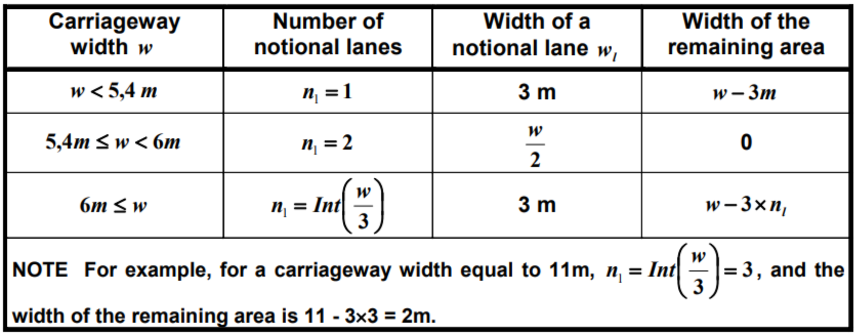

Carriageway width w	Number of notional lanes	Width of a notional lane w_l	Width of the remaining area
$w < 5{,}4\,m$	$n_1 = 1$	3 m	$w - 3m$
$5{,}4m \leq w < 6m$	$n_1 = 2$	$\frac{w}{2}$	0
$6m \leq w$	$n_1 = Int\left(\frac{w}{3}\right)$	3 m	$w - 3 \times n_l$
NOTE For example, for a carriageway width equal to 11m, $n_1 = Int\left(\frac{w}{3}\right) = 3$, and the width of the remaining area is 11 - 3×3 = 2m.			

Figure 3.1: Excerpt from Eurocode 1: dividing carriageway into notional lanes [14]

For the respective parts of the carriageway characteristic values for the loads are defined for the *Load Model 1* as given in figure 3.2. These values are representing a traffic scenario of heavy industrial international traffic, such that scaling factors can be used to represent a realistic scenario for the given bridge to be designed [14]. In the case of the straight bridge concept, the design team has chosen a scaling factor of 0.6 on the distributed load for notional lane number 1 and unity for the others. By multiplying the distributed loads by their mentioned factors and their respective widths, equivalent line loads are obtained. Finally, these line loads can be summed in order to implement the distributed traffic loads in the analyses of the bridge model as force or mass per meter acting on the bridge girder. In global analyses, the axle loads given by the *Tandem System* in figure 3.2 are to be applied in pairs centrally on the notional lanes, with two axles in each notional lane.

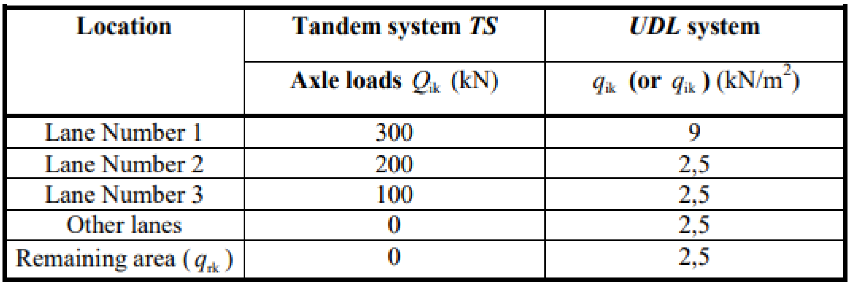

Location	**Tandem system *TS***	***UDL* system**
	Axle loads Q_{ik} (kN)	q_{ik} **(or** q_{ik}) (kN/m^2)
Lane Number 1	300	9
Lane Number 2	200	2,5
Lane Number 3	100	2,5
Other lanes	0	2,5
Remaining area (q_{rk})	0	2,5

Figure 3.2: Excerpt from Eurocode 1: characteristic traffic loads [14]

3.1.3 Wind Loads

Wind-induced loads are also by nature dynamic loads, due to the fluctuations in the wind velocity. The wind forces can thereby be stated in terms of a time-averaged wind force and a gust force [15]. The time-averaged wind force per meter can be expressed as:

$$F_m(z) = \frac{1}{2}\rho_a V_m^2(z) C_D(\alpha) H \tag{3.1}$$

where V_m is a time-averaged wind velocity at a given height z, ρ_a the air density and C_D a shape or drag coefficient. This coefficient is dependent on the angle of the wind direction, α, relative to the projected area, H. According to DNV [15] commonly used averaging times for the wind speed are 1 minute, 10 minutes and 1 hour for each given height. The wind speed is generally increasing with height above sea level.

Furthermore, the lift force due to wind should be considered for a bridge structure, as it can induce weak axis bending moments and accelerations. The time-averaged lift force can be expressed in a similar manner as the time-averaged drag force:

$$F_{L,m}(z) = \frac{1}{2}\rho_a V_m^2(z) C_L(\alpha) H_L \tag{3.2}$$

where C_L is a shape or lift coefficient. This coefficient is dependent on the angle of the wind direction, α, relative to the chosen reference area, H_L, for which this coefficient was calculated for. Both the drag and lift coefficients can be determined through tabular values or empirical formulas for simple geometries. For complex cross-sections and structures, these can be obtained through Computational Fluid Dynamics (CFD) or preferably model tests [15].

For simplified static calculations a gust drag force can be expressed in terms of the time-averaged wind force as [2]

$$F_q(z) = [1 + 7 \cdot I_u(z)] \cdot F_m(z) \tag{3.3}$$

where I_u is a turbulence intensity.

Finally, for a floating bridge also the time dependency of the wind is expected to be of importance, as the structure will exhibit considerable dynamic response. Since the natural frequencies of the bridge structure can be in the range of frequencies containing significant energy in the wind field frequency spectrum, this should be included as a part of the dynamic analyses [15].

3.1.4 Current Loads

The tidal current velocities in narrow points in fjords can be high, but usually floating bridges are not used for these types of crossings as other options are cheaper. According to Larsen [2], the current forces acting on the pontoons in the Bjørnafjorden bridge concept can be neglected for simplicity, due to their relative sizes compared to the first order wave forces.

For slender structures, such as mooring lines, the forces acting from current, which mainly are viscous forces, can be calculated by the drag term from the Morison's equation. When assuming negligible velocities of the mooring lines it can be written as

$$F_c(z) = \frac{1}{2}\rho C_D D v|v| \tag{3.4}$$

where C_D is the drag coefficient, D is a typical cross-section dimension and v is the current velocity.

In general, the current velocity is a sum of current components, where the most common types of currents are wind-generated currents, tidal currents, circulational currents, loop and eddy currents, soliton currents and longshore currents [15]. The current velocity depends on the position, water depth and time. The latter because of flow fluctuations due to turbulence. However, for most applications, the current can be assumed to only be dependent on the water depth [15].

3.2 Description of Regular Waves

In order to determine the forces acting from waves on the pontoons and mooring lines, a general description of regular waves will be given.

3.2.1 Use of the Velocity Potential

According to linear wave theory, often called Airy theory, the velocity potential for a long-crested regular wave in finite water depth in two dimensions can be written as [16]

$$\Phi = \frac{g\zeta_a}{\omega}\frac{cosh(k(h+z))}{cosh(kh)}cos(\omega t - kx) \tag{3.5}$$

where z is the distance from the sea surface, defined positive in the vertical direction, h the average water depth, g the gravitational acceleration and ω the circular wave frequency. The conditions for the velocity potential are given in section 3.2.2. The velocity potential is useful in order to obtain water particle velocities, accelerations and dynamic pressure, which are necessary for the calculations of wave loads as will be described in section 3.3.

For waves propagating in the x-direction, the surface elevation can be expressed as

$$\zeta = \zeta_a \ sin(\omega t - kx) \tag{3.6}$$

where ζ_a is the wave amplitude, equal to half the wave height H, k is the wave number, defined as k= $2\pi/\lambda$. From equation 3.6 it can be seen that the wave is propagating with a repetitive motion such that a constant wave period $T = 2\pi/\omega$ and wavelength λ can be obtained.

The relation between the wave number, or the wavelength, and the wave frequency, known as the dispersion relation can be expressed as

$$\omega^2 = kg \cdot tanh(kh) \tag{3.7}$$

The expressions presented for finite water depths can be simplified when assuming deep water. This assumption is in mathematical terms a consideration of when the corresponding depth dependent term from the velocity potential goes toward the term from the deep water velocity potential with sufficient accuracy. The same applies for the dispersion relation.

These approximations can be expressed as

$$\frac{cosh(k(h+z))}{cosh(kh)} \rightarrow e^{kz} \tag{3.8}$$

$$tanh(kh) \rightarrow 1 \tag{3.9}$$

such that the velocity potential and dispersion relation for infinite water depth can be written as

$$\Phi = \frac{g\zeta_a}{\omega} e^{kz} cos(\omega t - kx) \tag{3.10}$$

$$\omega^2 = kg \tag{3.11}$$

As a rule of thumb, it is reasonable to assume deep water when h $> \lambda/2$ [16]. By using the dispersion relation for deep water, this rule of thumb can be re-written in order to relate the water depth to the wave period.

$$T < 2 \cdot \sqrt{\frac{\pi h}{g}} \tag{3.12}$$

In the hydrodynamic analyses performed on the pontoons in this thesis, a water depth of 500 metres has been assumed for all pontoons when analysed in the hydrodynamic solver Wadam. According to the *Design Basis* [17] for Bjørnafjorden, the minimum depth for any of the pontoon locations in the straight bridge concept is about 55 meters and is found for the first pontoon in the northern end of the bridge. By the use of equation 3.12, it is reasonable to assume deep water for this pontoon at wave periods lower than 8.4 seconds. For the sea states analysed in this thesis, the assumption of a water depth of 500 meters for all pontoons is therefore expected to be of negligible significance for the results. Further considerations on this topic were not done.

3.2.2 Conditions for the Velocity Potential

In short, the velocity potential is obtained based on the assumption that sea water is incompressible and inviscid, hence satisfying the Laplace equation.

$$\nabla^2\Phi = 0 \tag{3.13}$$

In addition, the velocity potential has to satisfy a boundary, a kinematic and a dynamic condition, respectively, as presented in the following [16, 18].

Impermeability condition at the sea bottom, i.e. no fluid velocity into the sea bottom:

$$\left(\frac{\partial\Phi}{\partial z}\right)_{z=-h} = 0 \tag{3.14}$$

where h is the water depth of the flat sea bottom.

At the free surface the fluid particles are assumed to stay at the free surface. By further assuming the wave heights to be small this can be expressed by the kinematic condition as

$$\frac{\partial \zeta}{\partial t} = \left(\frac{\partial \Phi}{\partial z} \right)_{z=0} \tag{3.15}$$

Finally, the dynamic condition is set by demanding the pressure at the free surface to be equal to the ambient pressure, as well as still assuming the wave heights to be small.

$$g\zeta + \left(\frac{\partial \Phi}{\partial t} \right)_{z=0} = 0 \tag{3.16}$$

3.3 Wave Induced Forces

In the following section, the forces due to regular waves by use of linear theory will be described. In order for linear theory to give a realistic approximation, the waves' steepness has to be small, thus, the waves are far from breaking [18].

The consequence of linear theory is that the load amplitude is linearly proportional to the wave amplitude. Furthermore, this means that the response frequency of the structure is the same as for the wave loads acting on it. This applies to a steady state condition, i.e. no transient effects due to initial conditions [18]. Therefore, the response in irregular sea can be found by superimposing regular waves, and the irregularity is hence obtained due to the combinations of the individual amplitudes, periods and wave directions.

For a regular wave acting on a structure in a steady state condition, the hydrodynamic forces and moments can be divided into two sub-problems [18]:

- Wave excitation loads
- Added mass, damping and restoring forces and moments

3.3.1 Wave Excitation Loads

When the structure of consideration is restrained from oscillating, the forces and moments induced by incident regular waves are called wave excitation forces. These can further be divided into two components, namely Froude-Kriloff and diffraction forces and moments. Physically the former term can be related to the force due to the undisturbed pressure field and the latter term because the presence of the structure is changing the pressure field.

The wave excitation load acting on a body can be given by [18]:

$$\mathbf{F} = F_1\mathbf{i} + F_2\mathbf{j} + F_3\mathbf{k} \tag{3.17}$$

where

$$F_i = -\iint_S p n_i d\mathbf{s} + A_{i1}a_1 + A_{i2}a_2 + A_{i3}a_3 \tag{3.18}$$

where n_i is the unit vector normal to the body surface, S is the wet surface and A_{ij} is an added mass coefficient as will be described in the next subsection. The first term in equation 3.18 is the Froude-Kriloff force and p is therefore as stated the undisturbed pressure field, which can be calculated by finding the dynamic pressure from the velocity potential as

$$p = -\rho\frac{\partial\phi}{\partial t} \tag{3.19}$$

Furthermore, the acceleration terms can be found from the velocity potential as

$$a_1 = \frac{\partial^2\phi}{\partial x\partial t}, \qquad a_2 = \frac{\partial^2\phi}{\partial y\partial t}, \qquad a_3 = \frac{\partial^2\phi}{\partial z\partial t} \tag{3.20}$$

3.3.2 Added Mass, Damping and Restoring Forces and Moments

Added mass, damping and restoring forces and moments are the hydrodynamic loads acting on the structure when there are no incident waves, but the structure is forced to oscillate in any rigid body motion with the wave excitation frequency [18]. Due to the forced excitations, the structure generates outgoing waves and thereby oscillating fluid pressure on the body surface. The forces and moments acting on the structure can then be obtained by integration of the fluid pressure forces on the surface. When the structure is forced to move in a harmonic motion mode n_j the linear part of the added mass, damping and restoring forces can be expressed as

$$F_k = -A_{kj}\frac{d^2\eta_j}{dt^2} - B_{kj}\frac{dn_j}{dt} - C_{kj}n_j \tag{3.21}$$

Where A_{kj}, B_{kj} and C_{kj} are added mass-, damping- and hydrostatic restoring force coefficients, respectively. The indices k and j refers to the coordinate axis such that η_1, η_2 and η_3 refers to rigid body modes in the x-, y- and z-directions, respectively, and η_4, η_5 and η_6 to the corresponding rotational rigid body modes.

The mentioned coefficients are all dependent on the shape of the body. The added mass and damping coefficients are also dependent on the oscillation frequency and the speed of the body. The latter due to the occurrence of an encounter frequency.

The hydrostatic restoring coefficients can be found from geometry and mass considerations. For a freely floating body the vertical stiffness coefficient can simply be expressed as

$$C_{33} = \rho g A_{wp} \tag{3.22}$$

where A_{wp} is the body's water plane area.

The restoring coefficients in roll and pitch are given by [18]:

$$C_{44} = \rho g \nabla z_b - mgz_g + \rho g \iint_{A_{WP}} y^2 ds = \rho g \nabla \overline{GM}_T \tag{3.23}$$

$$C_{55} = \rho g \nabla z_b - mgz_g + \rho g \iint_{A_{WP}} x^2 ds = \rho g \nabla \overline{GM}_L \tag{3.24}$$

where z_b and z_g are the vertical coordinates of the centre of buoyancy and centre of gravity, respectively. ∇ is the body's displacement and finally, $\overline{GM}_T$ and $\overline{GM}_L$ are the transverse and vertical metacentric heights, respectively. From the latter equations, it should be stressed that the respective integrals are recognised as the roll and pitch area moments of inertia as given by equation 3.25 and 3.26.

$$\rho g I_{44} = \rho g \iint_{A_{WP}} y^2 ds \tag{3.25}$$

$$\rho g I_{55} = \rho g \iint_{A_{WP}} x^2 ds \tag{3.26}$$

For a double symmetric body, such as the pontoons, the remaining restoring coefficients are zero.

As presented, the stiffness matrix comprises of two effects: a moment arm effect due to the difference in locations of the centre of buoyancy and centre of gravity and the change in load due to the change in the submerged volume of the body. This matrix is in general non-linearly related to the body's position and orientation. For small changes, it is commonly assumed to be constant.

In analyses, the exact shape of the outer surface of the body has to be accounted for if non-linear changes in the area moments of inertia and centre of buoyancy should be included. Moreover, for a coupled model, the mass properties of the structure will contribute to the moment arm effect. A non-linear change in the location of the centre of gravity can be captured in a coupled model if the mass properties of the body and the structure are accounted for in their instantaneous positions.

3.3.3 Morison's Equation

The horizontal force acting on a strip, dz, of a small volume rigid vertical cylinder can be expressed by Morison's equation as [18]

$$dF = \rho \frac{\pi D^2}{4} dz\ C_m a_1 + \frac{\rho}{2} C_D D dz |u| u \tag{3.27}$$

where D is the diameter, C_m is a mass coefficient, a_1 the horizontal acceleration and u the horizontal velocity.

The first term of the equation represents the wave excitation force. By assuming no viscous forces it can be shown from potential theory that C_m is 2 for a circular cylinder, where the Froude-Kriloff force and the diffraction force, as presented in 3.3.1, contribute equally [18].

The second term is the viscous force, as used to estimate the drag force due to wind in section 3.1.3. Morison's equation is therefore commonly used in order to calculate the forces acting on small volume cylindrical members where viscous forces matter. This is also the case for RIFLEX, where a generalisation of Morison's equation is used to calculate the forces acting on the mooring lines [19]. The formula is then re-written in order to account for the velocities of the mooring lines, as well as their inclines.

3.4 Static Analysis

In this section methods for obtaining the static response will be presented and discussed.

3.4.1 Simplified Approach

For the floating bridge spans the self-weight and the girder properties are symmetric about the girder-column intersections, such that the span ends can be simplified as fixed. When further neglecting the cross-sectional differences at the support sections close to the girder-column intersections and averaging the self-weight as evenly distributed, the floating spans can be approximated as in figure 3.3a.

In this figure, s is the span length of a bridge section in the floating part of the bridge and q is the assumed evenly distributed force per meter of the section due to self-weight. This simplified approach will give an approximation of the magnitudes of the bending moments and shear forces, as well as their respective distributions, but is a too simple approach to obtain the exact representation when taking the cross-sectional differences into account.

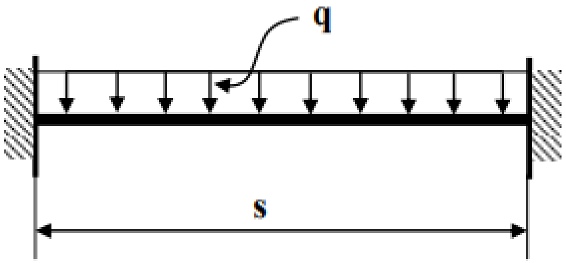

(a) Fixed beam subject to a uniform load

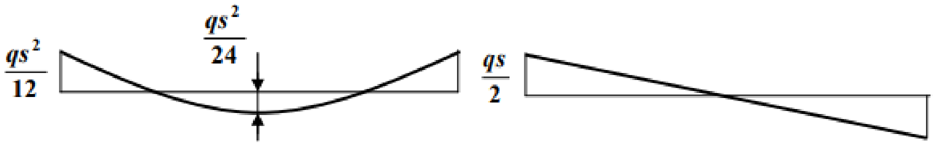

(b) Moment diagram

(c) Shear force diagram

Figure 3.3: Approximation of the bridge girder for a span section in the floating part of the bridge [20]

3.4.2 Static Linear Analysis

For the linear case, the static response of the structure can be found by solving

$$\mathbf{Kr} = \mathbf{R} \tag{3.28}$$

where $\mathbf{R}$ is the global load vector, $\mathbf{K}$ the global stiffness matrix and $\mathbf{r}$ the global nodal displacement vector. Equation 3.28 is based on the assumptions that the material is behaving linearly and elastic and that the displacements are small, such that the equilibrium equation can be based on the initial configuration [21].

3.4.3 Static Non-Linear Analysis

For the non-linear case, these assumptions are no longer valid due to the geometric, material or non-linearities due to changes of the boundary conditions. Consequently, the global stiffness matrix is then dependent on the nodal displacements such that the new relation becomes

$$\mathbf{K}_I(\mathbf{r})d\mathbf{r} = d\mathbf{R} \tag{3.29}$$

where $\mathbf{K}_I$ is the incremental stiffness. Equation 3.29 can be solved by the use of load incremental methods, iterative methods or a combination of these. RIFLEX uses a combination of Euler Cauchy method and Newton-Raphson iteration [19].

Euler-Cauchy Method

This is a load incremental method, thus based on a stepwise application of external loading, starting from the unloaded condition [21]. The new displacement at a step can then be found by adding the displacement increment obtained by the given load step by use of the previous incremental stiffness in equation 3.29.

As the previous incremental stiffness is used, this leads to an approximation, thus the true relation is not obtained as can be seen in figure 3.4. The latter implies that a smaller deviation can be obtained by reducing the size of the load increments at regions where the incremental stiffness is non-linear.

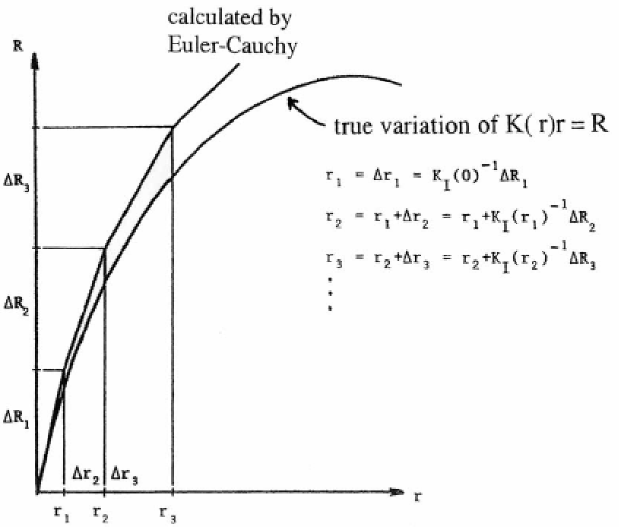

Figure 3.4: Euler Cauchy method [21]

Newton-Raphson Method

Newton-Raphson method is an iterative method and applied to the structural non-linear problem it can be written as [21]:

$$\mathbf{r}_{n+1} = \mathbf{r}_n - \mathbf{K}_I^{-1}(\mathbf{r}_n)(\mathbf{R}_{int} - \mathbf{R}) \tag{3.30}$$

Where n is the iteration step and $\mathbf{R}_{int}$ is the internal load vector. The procedure for a single degree of freedom system is illustrated in figure 3.5.

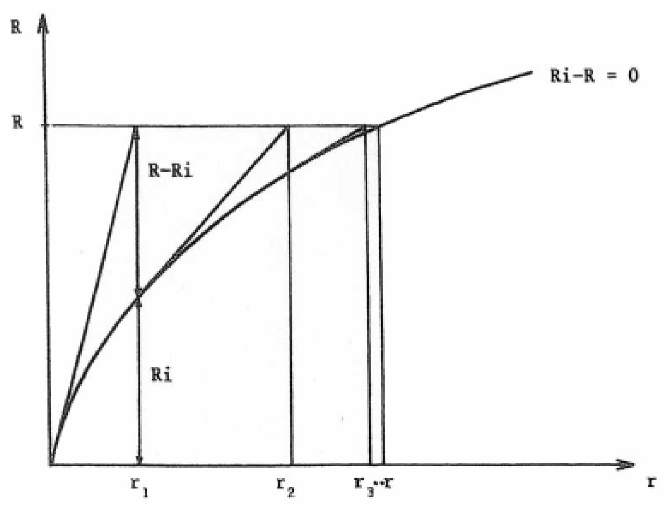

Figure 3.5: Newton-Raphson iteration for a single degree of freedom system [21]

From figure 3.5 it can be seen that the incremental stiffness is updated for each iteration step. The advantage of this method is a high convergence rate, but the updating of the incremental stiffness can be time-consuming. A modified version of Newton-Raphson can thereby be obtained by the choice of how often the incremental stiffness is updated. This method leads in general to a computational more efficient method where the convergence rate is somewhat slower [19].

In both cases, the iteration is stopped when the demanded accuracy is achieved and can be expressed by

$$||\mathbf{r}_{n+1} - \mathbf{r}_n|| < \epsilon \tag{3.31}$$

where ϵ is the demanded maximum absolute difference between the change of displacement from one iteration to the next [21].

3.4.4 Combined Method

RIFLEX uses a combination of Euler Cauchy method and Newton-Raphson iteration in an incremental-iterative procedure in order to find the static equilibrium [19]. The number of load steps, the maximum number of iterations and the accuracy are all user-specified for each load type in the static calculation procedure. The relevant load types for the bridge model were *volume forces*, *body forces*, *initially pre-stressed segments* and *specified displacements*. Figure 3.6 shows an example of the mentioned method whereas a modified Newton-Raphson iteration procedure is used. According to the RIFLEX Theory Manual [19] a full Newton-Raphson procedure is generally preferred. The number of iterations is commonly in the range of 5 to 15 iterations, where few load steps normally increase the number of iterations needed.

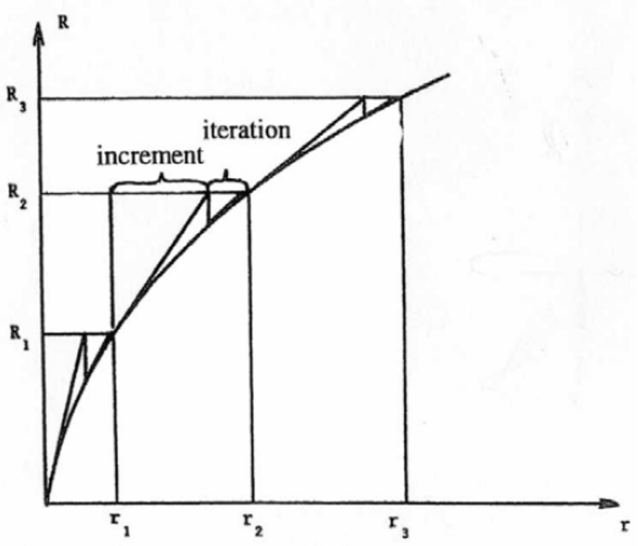

Figure 3.6: Euler-Cauchy incrementation with modified Newton-Raphson iteration [21]

3.5 Eigenvalue Analysis

Finding the natural frequencies and the corresponding mode shapes are of great importance for floating bridges due to the numerous loads acting on the total system. If an oscillating load acting in a given direction coincides with a natural frequency and the associated mode shape, the result can be large dynamic amplifications.

3.5.1 The General Eigenvalue Problem

The natural frequencies and the corresponding mode shapes can be obtained by solving the general eigenvalue problem, which can be derived by evaluations of the dynamic equilibrium equation given as [22]

$$\mathbf{M}\ddot{\mathbf{r}} + \mathbf{C}\dot{\mathbf{r}} + \mathbf{K}\mathbf{r} = \mathbf{Q}(t) \tag{3.32}$$

where **M**, **C** and **K** are the mass, damping and stiffness matrices, respectively. **Q**(t) is the time dependent external load vector and **r** is the nodal displacement vector, such that $\dot{\mathbf{r}}$ corresponds to the nodal velocity vector and $\ddot{\mathbf{r}}$ to the nodal acceleration vector.

For free and un-damped vibration the damping term and the external load vector are zero and equation 3.32 is simplified to

$$\mathbf{M}\ddot{\mathbf{r}} + \mathbf{K}\mathbf{r} = \mathbf{0} \tag{3.33}$$

When assuming harmonic vibration the nodal displacement and acceleration vectors can be expressed as

$$\mathbf{r} = \boldsymbol{\phi} \cdot sin(\omega t) \tag{3.34}$$

$$\mathbf{r} = -\omega^2 \boldsymbol{\phi} \cdot sin(\omega t) \tag{3.35}$$

where $\boldsymbol{\phi}$ is the displacement amplitude vector, ω the circular frequency and t the time. Finally, the *eigenvalue problem on general form* can be written as

$$(\mathbf{K} - \omega^2 \mathbf{M})\boldsymbol{\phi} = \mathbf{0} \tag{3.36}$$

For the non-trivial solutions of equation 3.36, ω is called the eigenfrequency, ω^2 the eigenvalue and $\boldsymbol{\phi}$ the corresponding eigenvector. Furthermore, the mode shape gives a description of the shape of the vibration of all parts of the system in terms of relative amplitudes, as given by the eigenvector [22]. The number of each of the mentioned properties is equal to the total number of degrees of freedom of the system.

3.5.2 Implementation in Analyses

The eigenvalue problem on general form, equation 3.36, can be re-written in order to describe the contributions in analyses performed in SIMO-RIFLEX:

$$((\mathbf{K} + \mathbf{k}) - \omega^2(\mathbf{M} + \mathbf{A}_\infty))\boldsymbol{\phi} = \mathbf{0} \tag{3.37}$$

where $\mathbf{A}_\infty$ is the infinite-frequency added mass matrix, as will be described in section 3.6.1, and **k** is the hydrostatic stiffness matrix. It should be noted that the mass matrix, **M**, will include the mass properties of the complete system, including the pontoons and mooring lines. Furthermore, the stiffness properties of the mooring system are included in the stiffness matrix **K**.

The implementation of non-linear catenary mooring systems in solution algorithms are dependent on some sort of linearisation of the stiffness terms, as the magnitudes of the vibrations are not known [22]. This is also the case for the system stiffness matrix. The incremental mooring stiffness in the static condition is a possible method, however, the calculation procedures used by RIFLEX are not included in the RIFLEX Theory Manual [19]. Therefore, also further descriptions of possible solution algorithms will not be given.

The following items should be stressed about the eigenvalue calculation codes used by SIMO-RIFLEX:

- There is great uncertainty on how catenary mooring systems are implemented in the calculations
- The calculations do not include frequency dependent added mass

These will be addressed in more detail throughout the report.

3.6 Dynamic Analysis

When the external loads are no longer applied in a very slow manner, dynamic effects are present and need to be accounted for.

When subject to dynamic loading, there will also be developed inertia forces, damping forces and external time-dependent forces as given by the dynamic equilibrium equation [22]:

$$\mathbf{M}\ddot{\mathbf{r}} + \mathbf{C}\dot{\mathbf{r}} + \mathbf{K}\mathbf{r} = \mathbf{Q}(t) \tag{3.38}$$

Where the terms are the same as described for equation 3.32. For a floating system the damping matrix, $\mathbf{C}$, can be written as

$$\mathbf{C} = \mathbf{C_s} + \mathbf{C_h} \tag{3.39}$$

where $\mathbf{C}_s$ and $\mathbf{C}_h$ are the structural and hydrodynamic damping matrices, respectively.

3.6.1 Dynamic Modelling of the Pontoons

In SIMO, which is used for modelling the pontoons in the coupled SIMO-RIFLEX model, the dynamic equation of motion is solved in the time domain by use of convolution integrals. By this technique the dynamic equation of motion for the pontoon can be expressed as [23]:

$$(\mathbf{M}+\mathbf{A}_\infty)\ddot{\mathbf{x}}(t)+\mathbf{D}_1\dot{\mathbf{x}}(t)+\int_0^t \mathbf{h}(t-\tau)\dot{\mathbf{x}}(\tau)d\tau+\mathbf{K}\mathbf{x}(t)=\mathbf{F}(t) \tag{3.40}$$

where **M** is the pontoon's mass matrix, $\mathbf{A}_\infty$ the added mass infinite frequency matrix, **x**, $\dot{\mathbf{x}}$ and $\ddot{\mathbf{x}}$ are the displacement, velocity and acceleration vectors of the pontoon, respectively. **K** is the stiffness matrix for the pontoon, which consists of the hydrostatic stiffness matrix and stiffness contributions from the bridge girder. **F**(t) is the excitation force vector and $\mathbf{D}_1$ is the linear damping matrix. For the case of the modelling done in this thesis, the excitation force vector only includes the first order wave force transfer functions. The last term in equation 3.40, i.e. **h**(t-τ), is the retardation function matrix, where t is the time and τ the time lag.

The infinite-frequency added mass matrix is used in the eigenvalue calculations in the coupled SIMO-RIFLEX model and is defined as [23]

$$\mathbf{A}_\infty=\mathbf{A}(\omega=\infty) \tag{3.41}$$

and can therefore physically be understood as the pontoon's instantaneous response to acceleration. The same type of definition yields for the infinite frequency damping matrix.

$$\mathbf{C}_\infty=\mathbf{C}(\omega=\infty)=\mathbf{0} \tag{3.42}$$

The matrices presented in equation 3.41 and 3.42 are related to the frequency dependent added mass and damping matrix as

$$\mathbf{A}(\omega)=\mathbf{A}_\infty+\mathbf{a}(\omega) \tag{3.43}$$

$$\mathbf{C}(\omega)=\mathbf{C}_\infty+\mathbf{c}(\omega) \tag{3.44}$$

The relation between the retardation functions and the frequency dependent added mass and damping can then be expressed as [23]

$$\mathbf{h}(\tau)=\frac{1}{\pi}\int_0^\infty(\mathbf{c}(\omega)\ cos(\omega\tau)+\omega\mathbf{a}(\omega)\ sin(\omega\tau))d\omega \tag{3.45}$$

and is the way frequency dependent added mass and damping are included in the dynamic analyses of the coupled model in the time domain.

By investigating the convolution integral in equation 3.40, it can be seen that the retardation functions represent a fluid memory effect. For every time step this integral will be solved from the start of the simulation until the given time, t.

This means that the simulation will be increasingly slower as the simulation time progresses.

In SIMO, the user has to specify a cut factor for the retardation functions, but the SIMO Theory Manual [23] does not specify how this factor is included in these functions. However, the cut factor is expected to be a way of truncating the retardation functions in the mentioned convolution integral. This can be done with small errors for a large cut factor as the retardation functions are seen to go towards zero as the time lag, τ, goes to infinity.

For the case of the modelling, the details on this truncating procedure are of secondary interest. This is because the effect of the choice of the cut off factor can be evaluated by comparing the re-calculation of the frequency dependent added mass and damping with the corresponding values used as input in SIMO. This trade-off between approximation and simulation time is further discussed in section 5.2.1. The mentioned re-calculations are done in SIMO based on equations 3.46 and 3.47 [23].

$$\mathbf{a}(w) = -\frac{1}{\omega}\int_0^\infty \mathbf{h}(\tau)\ sin(\omega\tau)d\tau \tag{3.46}$$

$$\mathbf{c}(w) = -\int_0^\infty \mathbf{h}(\tau)\ cos(\omega\tau)d\tau \tag{3.47}$$

3.6.2 Structural Damping

Structural damping is according to Langen [22] mainly damping related to friction and sliding within the material, called material damping, and damping related to the connections between different members in the structure. The material damping is therefore proportional to the deformation of the material.

The Global Rayleigh Damping Model

The global Rayleigh damping model is widely used, and also used by RIFLEX, in order to model structural damping in fixed structures [19]. The Rayleigh damping formulation is expressed as a linear combination of the global structural mass and stiffness matrix, as given in equation 3.48.

$$\mathbf{C} = \alpha\mathbf{M} + \beta\mathbf{K} \tag{3.48}$$

The damping proportionality coefficients α and β are related to the critical damping ratio, ξ, as

$$\xi = \frac{1}{2}(\frac{\alpha}{\omega} + \beta\omega) \tag{3.49}$$

where ω is the response frequency.

For two damping ratios known at their respective response frequency, equation 3.49 can be used to express the damping coefficients as

$$\alpha = 2\left(\xi_1\omega_2 - \xi_2\omega_1\right)\frac{\omega_1\omega_2}{\omega_2^2 - \omega_1^2} \tag{3.50}$$

$$\beta = \frac{2\left(\omega_2\xi_2 - \omega_1\xi_1\right)}{\omega_2^2 - \omega_1^2} \tag{3.51}$$

Chapter 4

Bridge Concept

In this section, the straight floating bridge concept used as a basis for the modelling will be presented, with focus on relevant aspects. The concept chosen was made in cooperation by COWI, Aas-Jakobsen, Johs Holt AS and Global Maritime, released 19.02.2016 [2]. This work was done on behalf of the NPRA as a part of the Ferry-Free E39 project. All data used in the modelling in the thesis are presented in this chapter and are gathered from the mentioned report [2], referred to as the *reference report*, and the separate appendix *Bilag B* [24].

Figure 4.1: Illustration of the straight bridge concept [26]

4.1 Coordinate System

The definition of the rigid body motion modes of the pontoon and the global coordinate system are given in figure 4.2, and are the coordinate systems used throughout this thesis. All pontoons are placed in the west-east direction, such that pontoon surge motion is positive along the global x-axis and sway motion along the y-axis. The origin of the pontoon's local coordinate system is placed at the centre of its waterplane area. Also the origin of the global coordinate system is placed at the waterplane, with its horizontal reference at the south end of the bridge, and positive z-direction upwards. Finally, the incoming wave directions are defined by the blue arrows as shown in figure 4.2b.

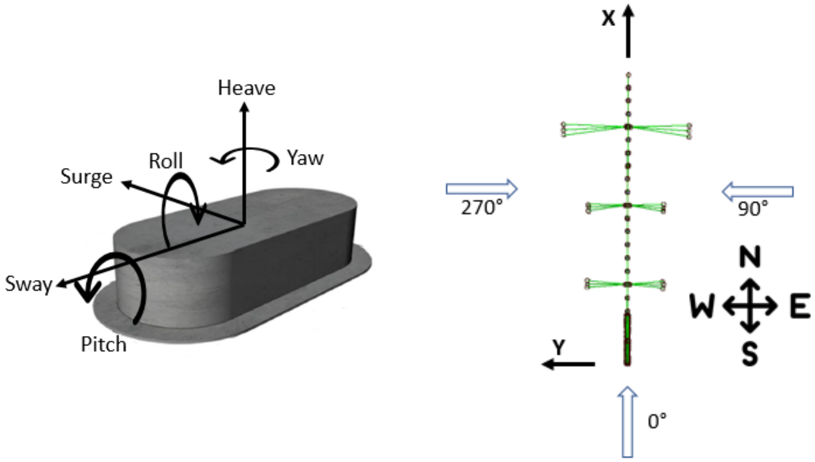

(a) Rigid body motion modes of the pontoon

(b) Global coordinate system and directions

Figure 4.2: Definition of the rigid body motion modes of the pontoon and the global coordinate system. The blue arrows define the direction convention used for incoming waves.

4.2 Main Dimensions

The concept is a 4454 metres long straight floating bridge across Bjørnafjorden and has 18 pre-tensioned mooring lines supporting the bridge in the lateral direction. The bridge consists of a cable-stayed bridge and a floating bridge, where the latter has a total of 18 identical pontoons, with an equal spacing of 203 metres. The cable-stayed bridge has a side span of 350 metres and a main span of 450 metres, ensuring a navigational channel of minimum 400 m x 45 m. An overview of the concept and a definition of its components are presented in figure 4.3.

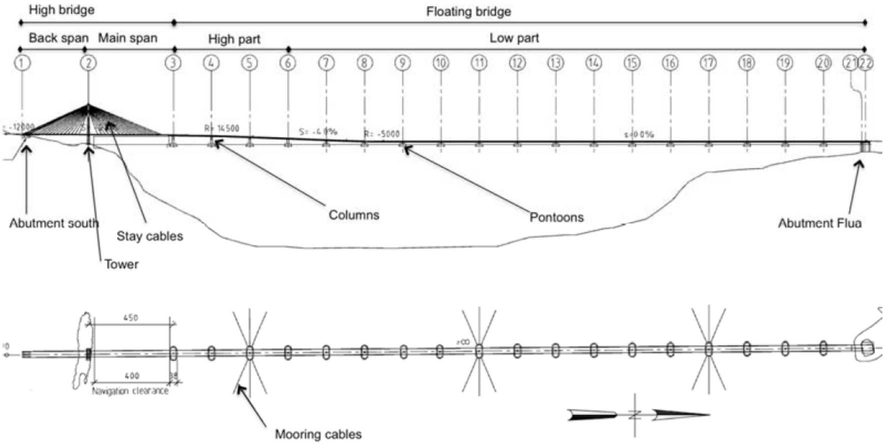

Figure 4.3: Side and top view of the bridge concept, including a nomenclature [2]

4.3 Bridge Girder

The bridge girder consists of a steel mono box girder, where a total of four cross-sections are used. Two are used in the high bridge and are denoted H1 and H2, where the latter is used at the tower intersection. Similarly, for the low bridge S1 is at the intersections with the columns from the pontoons and F1 in the spans. H2 and S1 are re-enforced versions of H1 and F1, respectively. The exact way the cross-sections are distributed is shown in table 4.1.

Table 4.1: Distribution of the cross-sections in the bridge girder [24]

Cross-section	Longitudinal location
Abutment south	X=0m to X=40m
H1	X=40m to X=340m
H2	X=340m to X=360m
H1	X=360m to X=770m
S1	X=770m to X=800m
S1 (25 m) - F1 (153m) - S1 (25m)	X=800m to X=4454m

The cross-section used in the spans in the low bridge, F1, can be seen in figure 4.4. The height of F1 and S1 is 6.5 metres, while the height of the cross-sections in the high bridge is 3.5 metres. Their remaining relevant cross-sectional properties are given in table 4.2. The Young's modulus used for the steel in the bridge girder was $2.1 \cdot 10^8\ kN/m^2$.

Table 4.2: Cross-sectional properties of the bridge girder [2]

Parameter	Unit	H1	H2	S1	F1
Area	m^2	1.41	2.55	2.21	1.55
Iy (weak axis)	m^4	3.35	6.09	18.06	12.77
Iz (strong axis)	m^4	114.94	212.36	184.60	126.31
It (torsion)	m^4	11.63	21.24	57.02	39.62
Total steel weight	tons/m	12.3	21.2	19.4	14.2
Asphalt, railings, etc.	tons/m	5.54	5.54	5.54	5.54
Total permanent weight	tons/m	17.8	26.7	24.9	19.7

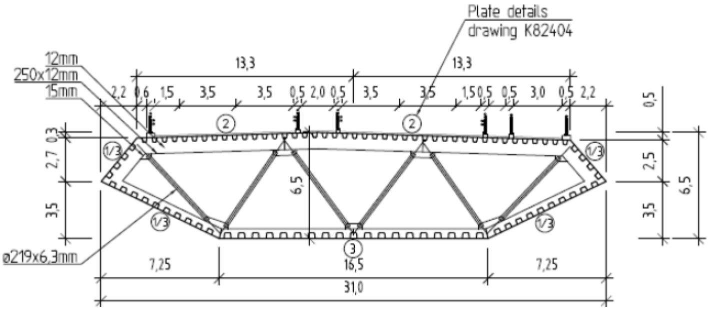

Figure 4.4: Low bridge cross-section, F1 [2]

4.4 Columns

From each pontoon, there is a single column of diameter 10 metres supporting the bridge girder. These are made of steel and are placed centrally on the pontoons and intersect the bridge girder in its neutral axis. The columns' relevant cross-sectional properties are given in table 4.3, whereas their lengths vary as given in table 4.4.

Table 4.3: Cross-sectional properties of the columns [2]

Parameter	Unit	Axis 3-6	Axis 7-20
Area	m^2	2.1	1.6
I (bending)	m^4	26.31	20.03
I_t (torsion)	m^4	52.62	40.06
Weight	tons/m	19.0	14.3

Table 4.4: Column lengths [2]

	Axis 3	Axis 4	Axis 5	Axis 6	Axis 7	Axis 8	Axis 9-20
Length [m]	43.27	38.37	31.97	23.85	15.73	8.59	7.56

4.5 Abutments and the Girder-Tower Connection

Both the northern and the southern abutments consist of concrete caissons which are filled with sand ballast. The southern abutment is 40 metres long and is a part of the side span of the high bridge, leaving this span to a free length of 310 metres. The bridge girder is connected to this abutment through shear stud connections.

The northern abutment is not considered a part of the first span of 203 metres, is 48 metres long and also wider and deeper than the southern. The forces from the bridge girder are transferred to this abutment by the use of two vertical and horizontal bearings with a spacing of 40 metres, allowing the bridge girder to move in the longitudinal direction. Within the 48 metres caisson, the bridge girder is filled with 5000 m^3 rock ballast.

The bridge girder is connected to the tower in the cable-stayed bridge by the use of four multi-directional elastomeric pot bearings. Two are supporting the girder in the vertical direction and two in the lateral direction. The girder is allowed to move freely in the longitudinal direction in order to avoid large bending moments in the tower due to changes in temperature.

4.6 Pontoons

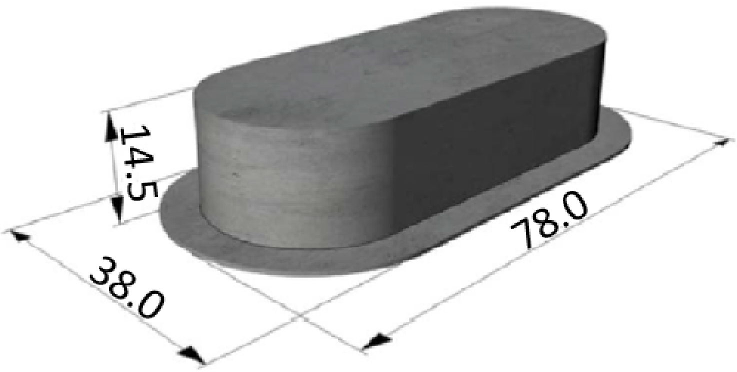

Figure 4.5: Pontoon main geometry [2]

As mentioned in section 4.2, the bridge has 18 pontoons which are equal with respect to dimensions and material. All pontoons are spaced with a distance of 203 metres. The main geometry is shown in figure 4.5.

Furthermore, the pontoons are built up by compartments, such that flooding of one or two compartments should not be critical. In normal operation, solid ballast is planned to be used. As seen in figure 4.5, a flange has been added to the pontoon, which was done in order to increase the added mass in heave. The main relevant pontoon parameters are given in table 4.5.

Table 4.5: Main relevant pontoon parameters [2]

Parameter	Unit	Value
Displacement	tons	18 300
Mass	tons	11 300
Roll inertia	tons·m^2	4 900 000
Pitch inertia	tons·m^2	1 360 000
Yaw inertia	tons·m^2	5 700 000
Roll water plane stiffness	MNm/rad	5700
Pitch water plane stiffness	MNm/rad	1000
Heave stiffness	MN/m	17.5
COG_z^*	m	-4.2
COB_z^*	m	-5.37
Draft	m	10.5
Height	m	14.5
Length	m	28.0
Width	m	68.0
Flange width	m	5.0

*Relative to the waterline

4.7 Mooring System

The mooring system consists of a total of 18 mooring lines, whereas three sets of 6 mooring lines are attached to pontoon number 3, 9 and 15, respectively. The anchors for the mooring lines for the two first pontoons are placed at a depth of 500 metres and for pontoon number 15 they are placed at a depth of 350 metres. The anchor locations are visualised in figure 4.6 together with the mooring spread. The exact anchor locations are given in table 4.6. The anchors are assumed to be fixed, as limited information on the soil conditions is known at this stage.

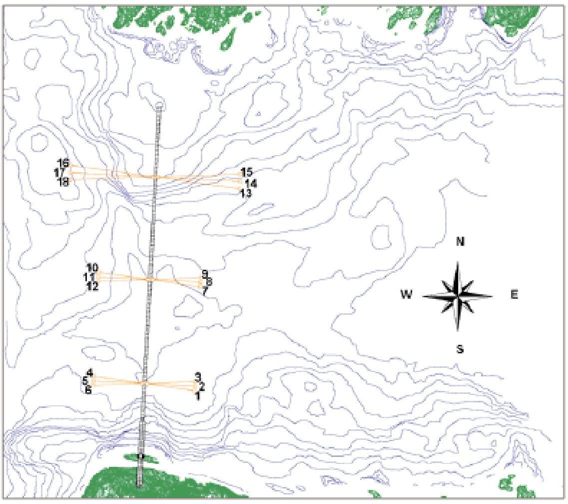

Figure 4.6: Overview of the mooring system [2]

Table 4.6: Anchor locations [2]

Mooring line no [-]	Pontoon [-]	X-coordinate [m]	Y-coordinate [m]
1	3	1153.7	-597.7
2	3	1206.0	-600.0
3	3	1258.3	-597.7
4	3	1258.3	597.7
5	3	1206.0	600.0
6	3	1153.7	597.7
7	9	2371.7	-597.7
8	9	2424.0	-600.0
9	9	2476.3	-597.7
10	9	2476.3	597.7
11	9	2424.0	600.0
12	9	2371.7	597.7
13	15	3554.8	-996.2
14	15	3642.0	-1000.0
15	15	3729.2	-996.2
16	15	3729.2	996.2
17	15	3642.0	1000.0
18	15	3554.8	996.2

The fairlead positions for the pontoons are identical for the three pontoons. They are placed at the waterline, z=0. The locations in the horizontal plane can be seen in figure 4.7. The fairleads are not placed at the pontoon ends in the analyses. The black lines in the figure do not show the outer skin of the pontoon, only the shape of the pontoon, since the width is 68 metres.

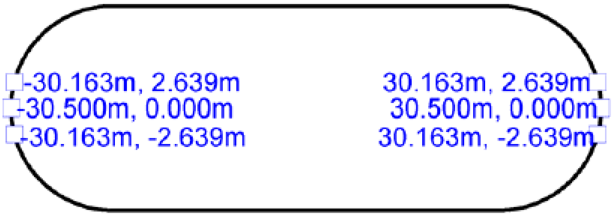

Figure 4.7: Fairlead positions [2]

The mooring lines consist of 20 metres of top chain of grade R5 studless and 100 metres of bottom chain of grade R4 studless. Pontoon 3 and 9 have mooring lines consisting of 641 metres of wire and pontoon 15 has lines of 920 metres of wire. This leads to a total mooring line length of 761 metres for the lines connected to pontoon 3 and 9 and a length of 1040 metres for those connected to pontoon 15. The mooring line component properties are given in table 4.7.

Table 4.7: Mooring line component properties [2]

Parameter	Unit	Bottom chain	Wire	Top chain
Nominal diameter	mm	175	175	175
Axial stiffness	kN	$2.41{\cdot}10^6$	$1.59{\cdot}10^6$	$2.41{\cdot}10^6$
Minimum breaking load	kN	25 200	24 300	27 900
Marine growth	mm	40	60	80
Weight in air*	kg/m	685	203	783
Normal drag coefficient*	-	3.5	3.0	4.6
Axial drag coefficient*	-	1.7	0.01	2.2

* Including the contribution from marine growth.

4.8 Cable-Stayed Bridge

The cable-stayed bridge consists of a side span of 350 metres, a main span of 450 metres, a tower with a height of 215 metres and 2x18 cable stays for each span. The road line's height above sea level decreases from about 56.5 metres at the southern abutment to 52.5 metres above the first pontoon. The stay cables consist of high strength steel strands and are pre-tensioned in order to minimise the weak axis bending moments in the bridge girder. Their relevant properties and pre-tensions are given in table 4.8 and 4.9. Furthermore, the tower is made of concrete and is fixed on an island 5 metres above sea level. Its cross-sectional properties and geometry will not be modelled in detail.

Table 4.8: Stay cable properties, side span [24]

No [−]	Dist. tower [m]	Length [m]	Mass [tons]	Area [mm^2]	Axial Stiffness [kN]	Force [kN]
1	350	385.0	26.6	8790	$1.71 \cdot 10^6$	4753
2	340	374.8	25.0	8494	$1.66 \cdot 10^6$	4557
3	330	364.8	23.4	8187	$1.60 \cdot 10^6$	4358
4	320	354.7	21.9	7869	$1.53 \cdot 10^6$	4157
5	310	344.6	20.4	7539	$1.47 \cdot 10^6$	3953
6	290	325.6	18.9	7389	$1.44 \cdot 10^6$	3851
7	270	306.8	17.0	7076	$1.38 \cdot 10^6$	3682
8	250	288.1	15.3	6758	$1.32 \cdot 10^6$	3523
9	230	269.7	13.6	6433	$1.25 \cdot 10^6$	3366
10	210	251.5	12.1	6104	$1.19 \cdot 10^6$	3210
11	190	233.7	10.6	5771	$1.13 \cdot 10^6$	3051
12	170	216.3	9.2	5436	$1.06 \cdot 10^6$	2890
13	150	199.3	8.0	5102	$9.95 \cdot 10^5$	2727
14	130	183.1	6.9	4773	$9.31 \cdot 10^5$	2568
15	110	167.6	5.9	4453	$8.68 \cdot 10^5$	2415
16	90	153.3	5.0	4151	$8.09 \cdot 10^5$	2272
17	70	140.4	4.3	3877	$7.56 \cdot 10^5$	2139
18	50	129.3	3.7	3643	$7.10 \cdot 10^5$	2011

Table 4.9: Stay cable properties, main span [24]

No [−]	Dist. tower [m]	Length [m]	Mass [tons]	Area [mm^2]	Axial Stiffnes [kN]	Force [kN]
1	50	129.8	3.7	3641	$7.10 \cdot 10^5$	2011
2	70	141.0	4.3	3871	$7.55 \cdot 10^5$	2139
3	90	154.0	5.0	4141	$8.07 \cdot 10^5$	2272
4	110	168.5	5.9	4437	$8.65 \cdot 10^5$	2415
5	130	184.0	6.9	4749	$9.26 \cdot 10^5$	2568
6	150	200.3	8.0	5070	$9.89 \cdot 10^5$	2727
7	170	217.3	9.2	5394	$1.05 \cdot 10^6$	2890
8	190	234.8	10.5	5718	$1.12 \cdot 10^6$	3052
9	210	252.7	12.0	6040	$1.18 \cdot 10^6$	3211
10	230	270.9	13.5	6358	$1.24 \cdot 10^6$	3367
11	250	289.4	15.2	6671	$1.30 \cdot 10^6$	3523
12	270	308.1	16.9	6977	$1.36 \cdot 10^6$	3683
13	290	326.9	18.7	7277	$1.42 \cdot 10^6$	3851
14	310	346.0	20.6	7569	$1.48 \cdot 10^6$	3952
15	330	365.1	22.5	7855	$1.53 \cdot 10^6$	4156
16	350	384.3	24.5	8133	$1.59 \cdot 10^6$	4358
17	370	403.7	26.6	8405	$1.64 \cdot 10^6$	4556
18	390	423.1	28.8	8669	$1.69 \cdot 10^6$	4744

Chapter 5

Modelling

The bridge model was made as a coupled SIMO-RIFLEX model in SIMA. The goal was to make the model as close as possible to the drawings and parameters as given in the reference report by Larsen [2] on behalf of the NPRA.

In this chapter the whole procedure of making the model will be described. This includes how the hydrodynamic analysis was done in order to provide input for the pontoons modelled as SIMO bodies, the modelling of the bridge structure and mooring lines in RIFLEX and how these were merged to a SIMO-RIFLEX model.

5.1 Hydrodynamic Analysis of the Pontoon

The pontoons were implemented in SIMA as SIMO bodies. These were in turn based on the hydrodynamic results obtained by analysing the pontoon separately in the module Wadam in HydroD. This analysis perquisites a panel model of the pontoon and its mass properties. The mentioned steps will be described in detail in the following sections.

5.1.1 Panel Model

The panel model was made in GeniE by making one-quarter of the outer skin of the pontoon. Only one-quarter was made as Wadam can utilise the double symmetry in order to save computational time and disk space resources, both when running the hydrodynamic analysis in Wadam and also when running analyses in SIMA [27]. The geometry was made in accordance with the parameters given in table 4.5. The origin of the coordinate system was set at the centre of the waterplane area, which also was the origin used in the hydrodynamic analysis. The thickness of the flange was not specified in the reference report. A thickness of 0.5 metres was chosen based on comparisons of the converged results obtained in Wadam with the hydrodynamic results obtained by the NPRA.

After the outer skin of the pontoon had been made in GeniE, wet sides had to be defined, a dummy hydrodynamic pressure applied and the mesh size chosen. The mesh size applied in GenieE is also the mesh size used by Wadam. In order to determine the mesh size to be used in the final model, a convergence analysis was carried out. This is described in section 6.1. Finally, the pontoon was exported from GeniE as a SESAM Finite Element File.

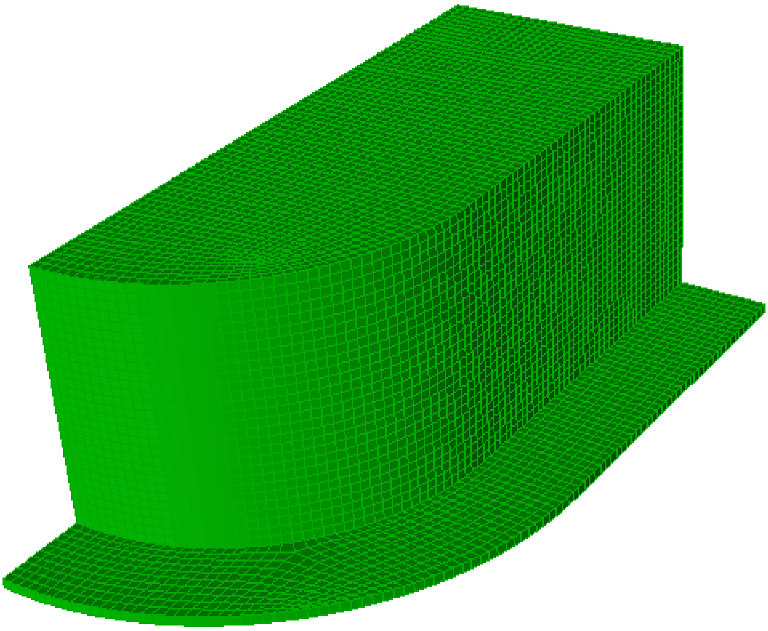

Figure 5.1: Panel model with an element size of 0.5 m x 0.5 m made in GeniE

5.1.2 Hydrodynamic Analysis in Wadam

In order to perform the hydrodynamic analysis, Wadam was run from the HydroD workbench and the option to use a Wadam wizard was chosen. The setup for the first and second order 3D potential theory for large volume structures was used.

The analysis was executed in the frequency domain, where the corresponding periods were chosen in a range from 0.2 seconds and up to 1000 seconds. At the lowest periods the frequency dependent results are changing most rapidly, hence small intervals were chosen. The intervals were made increasingly coarser with increasing periods. Both the computational time and memory usage increase with the number of periods chosen, such that the number was held well within the permitted 200. In retrospect, it was clear that for the analyses carried out, periods up to the first eigen period would have been sufficient.

The wave propagating directions were chosen from 0 to 90 degrees with an interval of 5 degrees. Due to the double symmetry, the direction set was only chosen in the first quadrant. The pontoon was analysed at its design draft and with the origin at the waterline. For all pontoons, the water depth was assumed to be 500 metres.

The mass model part of the wizard was filled based on the pontoon mass properties as given in table 4.5. Finally, the Hydrodynamic Results Interface File from Wadam was exported as a formatted sequential file (SIF) [27]. Also the Wadam print file (LIS) was saved in order to be used in the convergence analysis of the hydrodynamic results and to read added mass coefficients in the eigenvalue analysis, as described in 6.3.

5.2 Alteration of Hydrodynamic Results in SIMO

The hydrodynamic results were imported to SIMA as a SIMO body, in which was copied within SIMA to obtain the correct number of initially equal pontoons. The unaltered SIMO body contained:

- Mass properties
- Linear damping matrix
- Hydrostatic stiffness matrix
- First order motion transfer functions
- First order wave force transfer functions
- Frequency dependent added mass and damping and retardation functions
- Added mass zero and infinite-frequency matrix

To ensure realistic modelling of the pontoons in the global model, some modifications of the data imported from Wadam had to be done due to the calculation methods within SIMO, as well as the fact that only the pontoon itself was analysed in Wadam.

5.2.1 Retardation Functions

The retardation functions were calculated in SIMO based on the frequency dependent added mass and damping obtained in Wadam. A cut factor and the time step were given as user input in SIMO. The retardation functions were used in the time domain analyses in the coupled model, consequently, the frequency dependent added mass and damping were not used directly. The time step specified for the retardation functions had to be smaller than the time step chosen for the time domain analysis [23].

The cut factor was chosen in an iteration procedure where the trade-off between approximation and time was considered. The approximation was evaluated by comparing the diagonal terms of the recalculation of added mass and damping from the retardation functions with the values obtained in Wadam.

5.2.2 Buoyancy Force

Initially, as the pontoons are imported to SIMA, but not yet connected to the bridge, SIMO assumes the bodies to be placed at their stiffness references, respectively [23]. When specifying *include gravity* the pontoon will carry its weight by the restoring forces, hence no buoyancy force is automatically applied. Therefore, the displacement of the pontoon at its design draft was applied manually by means of a specified force acting at the pontoon's vertical centre of buoyancy, -5.37 m, as calculated in Wadam.

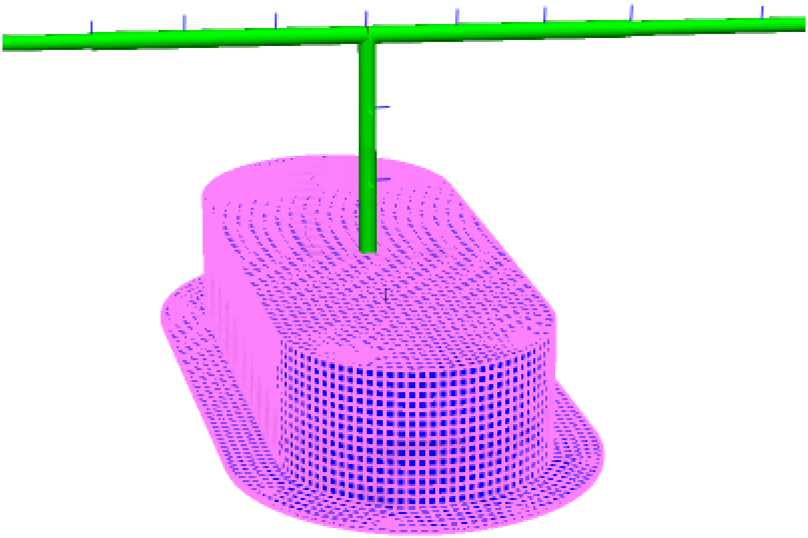

Figure 5.2: Pontoon attached to the global model

Finally, as the pontoons were connected to the global model, see figure 5.2, they were ballasted such that the weight of the bridge girder, the columns, the mooring lines and the self-weight of the pontoons, including the ballast, were carried by these buoyancy forces at the pontoons' design draft.

5.2.3 Ballasting

The amounts of ballast which were required to obtain the design draft for all pontoons are seen in table 5.1. A margin of 2 mm was used, such that the freeboard of all pontoons was within 4 m ± 0.002 m. The amounts of ballast needed proved to be in accordance with the amounts specified by the separate appendix, *Bilag B* [24], of the reference report. Therefore, the vertical centre of gravity of the added ballast for each pontoon was chosen as specified by the same document.

Table 5.1: Ballast required and its effect on the vertical centre of gravity

Pontoon no [−]	Mass [tons]	% of pontoon mass	VCG*$_{ballast}$ [m]	VCG*$_{pontoon}$ [m]
1	3639	32.2	-10.1	-5.62
2	2412	21.3	-10.2	-5.24
3 (mooring)	1012	9.0	-10.4	-4.69
4	2845	25.2	-10.2	-5.39
5	2982	26.4	-10.1	-5.43
6	3079	27.2	-10.1	-5.46
7-8, 10-14, 16-18	3096	27.4	-10.1	-5.46
9 (mooring)	1286	11.4	-10.4	-4.81
15 (mooring)	1655	14.6	-10.3	-4.96

*Relative to the waterline

Table 5.2: Mass moment of inertia of the pontoons, including ballast, relative to the waterline

Pontoon no [−]	Roll inertia [10^6 tons·m^2]	Pitch inertia [10^6 tons·m^2]	Yaw inertia [10^6 tons·m^2]
1	6.46	1.94	7.11
2	5.94	1.75	6.64
3 (mooring)	5.34	1.53	6.09
4	6.13	1.82	6.80
5	6.19	1.84	6.86
6	6.23	1.86	6.90
7-8, 10-14, 16-18	6.23	1.86	6.90
9 (mooring)	5.46	1.57	6.20
15 (mooring)	5.62	1.63	6.34

From table 5.1 it can be seen that the pontoons have a significant amount of excess buoyancy. This is because the pontoons were originally designed for the curved bridge alternative [12]. The mass moment inertia terms of the ballast about the ballast vertical centre of gravity as specified in *Bilag B* [24] were added to the mass moment inertia terms for the un-ballasted pontoons as specified in table 4.5 by the use of Steiner's Theorem. The resulting mass moment inertia terms of the pontoons, including ballast, about the waterline are given in table 5.2.

Finally, all changes of the mass properties of the pontoons due to ballast were implemented in the SIMO-RIFLEX model by modifying the structural mass in the SIMO bodies according to the tables presented.

5.2.4 Hydrostatic Stiffness Matrix

As only the pontoon itself, or specifically only the mass properties of the pontoon itself, were included in the analysis in Wadam, the hydrostatic stiffness matrix obtained had to be modified. The moment arm terms due to the difference in locations of the centre of buoyancy and gravity are calculated automatically by RIFLEX, including the contributions from the RIFLEX elements. Consequently, only the roll and pitch area inertia terms should be specified in the SIMO bodies. These are given by table 4.5. Alternatively, these can be calculated by excluding the displacement and mass dependent terms from the equations for the roll and pitch hydrostatic stiffness:

$$C_{44}^{SIMA} = C_{44}^{Wadam} - \rho g \nabla z_b + mgz_g = \rho g I_{44} \tag{5.1}$$

$$C_{55}^{SIMA} = C_{55}^{Wadam} - \rho g \nabla z_b + mgz_g = \rho g I_{55} \tag{5.2}$$

where z_g is COG_z and z_b is COB_z of the pontoon when analysed separately in Wadam. The heave stiffness, C_{33}, is unaltered, as it is only dependent on the water plane area of the pontoons.

5.2.5 Body Specification

As a consequence of the modifications of the stiffness matrix, the first order motion transfer functions obtained in Wadam are not correct, as these are dependent on the mentioned coefficients. Additionally, when the *6 DOF - time domain* body type is chosen in SIMO, the first order motion transfer functions are not used [23]. Another important characteristic of this body type is that it uses the *infinite-frequency added mass matrix* in the eigenvalue analysis. SIMO does not support using frequency dependent added mass in the eigenvalue analysis.

When the eigenvalue analyses were carried out this problem was partly bypassed by running several eigenvalue analyses. For each analysis a MATLAB-script was used to read added mass coefficients from the Wadam print file (LIS), for a selected frequency, to replace the original infinite frequency added mass matrix. However, this led to a time-consuming procedure and was only included for a few frequencies for illustration purposes.

5.2.6 Final SIMO Properties

Eventually, the pontoon properties defined in SIMO, which were used in the coupled SIMO-RIFLEX model, were reduced to:

- Modified mass properties
- Modified hydrostatic stiffness matrix
- Linear damping matrix
- First order wave force transfer functions
- Retardation functions
- Infinite-frequency added mass matrix

It should be recalled that the hydrodynamic results were obtained in Wadam by analysing the pontoon with the origin of the coordinate system at the waterline, such that the results in SIMO were given for the same coordinate system. The SIMO bodies were therefore connected to the respective columns of the bridge structure made in RIFLEX at the waterline.

5.3 RIFLEX: Bridge Structure and Mooring Lines

Modelling the RIFLEX part of the model, which only excludes the pontoons, was done by defining *supernodes*, which are the basis for the creation of lines. All lines were set as straight, whereas the original design has some slightly curved girders in the vertical plane in the transition from the high bridge to the lower floating part of the bridge.

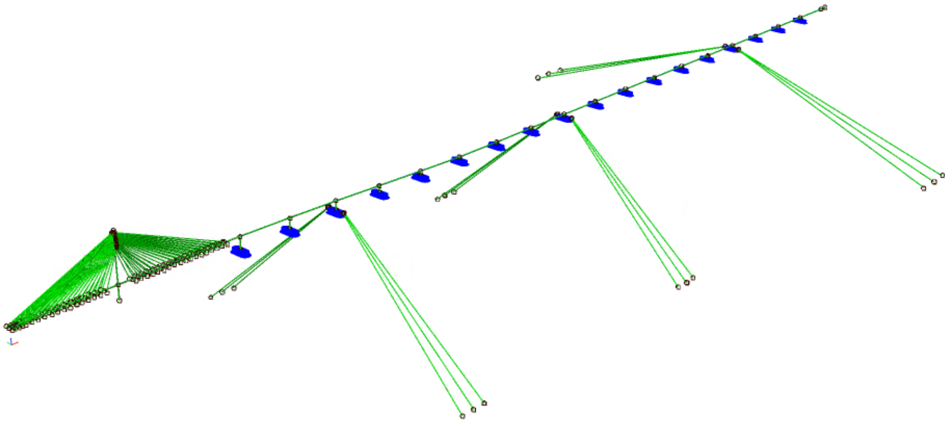

Figure 5.3: The complete model in SIMA

There was placed one supernode in every intersection, both bridge ends, land connection of the tower and at each pontoon top and at z=0 in the pontoons. It was also used supernodes to define the anchors and the fairleads for the mooring system, as well as an extensive amount of supernodes to model the cable-stayed bridge, as will be described in section 5.3.5. All supernodes in the bridge girder, except its ends, were set as free. The tower foundation was set as fixed. The complete model can be seen in figure 5.3

5.3.1 Abutments

A simplification of the modelling of the abutments described in section 4.5 was performed. In the south end of the bridge, the first five supernodes in the bridge girder were set to fixed in all translations and rotations. These were placed at the longitudinal intersections with the first four stay cables, i.e. each 10 metre, and were therefore a part of the abutment of 40 metres length as specified.

At the northern bridge end, the abutment was modelled by fixing all degrees of freedom, except translation in the longitudinal direction, for the supernode defined as the end of the last floating bridge span.

5.3.2 Girder-Tower Connection

The bridge girder was connected to the tower in the vertical and lateral direction, as well as for longitudinal rotation about the bridge girder. This was done in a similar procedure as described and visualised in *Bilag B* [24] in the reference report, i.e. by use of approximate methods. RIFLEX does not have a specific connection joint or supernode for this purpose.

Two 10 metres long bars and a 1 metre long beam were added, providing a lateral and vertical stiffness of $1.0{\cdot}10^9$ kN/m and rotational stiffness. The beam was defined along the bridge girder, with each end 0.5 metres away from the intersection. The ends of the beam were slaved to the tower at the connection point and the midpoint was connected to the bridge girder. The torsional stiffness was set to $1.0 \cdot 10^{12}\ kNm^2$ in order to fix the longitudinal rotation of the bridge girder at the intersection.

For each bar, one end was connected to the bridge girder at the girder-tower intersection location. The other end was set 10 metres laterally for one bar and 10 metres vertically for the other, relative to this location. These ends were set as slaved, whereas the supernode in the tower at the intersection point was modelled as a master degree of freedom. The axial stiffness for both bars was set to $1.0 \cdot 10^{10}$ kN/m

5.3.3 Assigning Cross-Sectional Properties

After the main geometry had been established, the lines, i.e. the respective girders, cable stays, columns and mooring lines were assigned cross-sectional properties, according to table 4.2 for the bridge girder, table 4.8 and 4.9 for the cables stays and table 4.7 for the mooring system. To do this, first the *line types* had to be defined. These are essentially defining the unstressed length of the corresponding lines, the number of segments, elements and have a cross-section attached. Thereby, a unique line type had to be defined for each line which had a unique length or cross-sectional property. This was the case for each pair of stay cables.

5.3.4 Mooring System

The eigen periods obtained from the eigenvalue analysis of the complete coupled model, which includes the catenary mooring system, proved to give large deviations compared to those obtained by the NPRA. As a part of the troubleshooting process a model with a linearised mooring system was made and included in the eigenvalue analyses. This model was identical to the original model except for its mooring system.

Catenary Mooring System

For the original model, the mooring lines were modelled in RIFLEX, where the pre-tensions were implemented by specifying the stress-free lengths of the mooring lines relative to the respective distances between the anchors and the fairleads. In order to account for the stiffness contributions from the mass of the mooring lines, an iteration procedure was needed to obtain the correct pre-tensions.

The fairlead positions were set by defining supernodes in their global coordinates by the use of master-slave supernode connections, whereas the fairlead supernodes were set as slaves and the respective pontoon supernodes as master. This ensured the fairleads to be rigidly connected to the respective pontoons.

Linearised Mooring System

When the model with the linearised mooring system was used in the eigenvalue analyses, the catenary mooring lines from the original model were de-selected in SIMA and replaced by a linear implementation. This was done by modifying the hydrostatic stiffness matrices for the pontoons originally holding the catenary mooring lines. The stiffness terms presented in table 5.3 were added to the original stiffness matrix given for pontoon 3 and 9, and matrix 5.4 to pontoon 15. The mentioned stiffness terms were gathered from the mooring characteristics as given in *Bilag B* [24] in the reference report.

Table 5.3: Linearised mooring stiffness terms for pontoon 3 and 9 [24]

	Surge	Sway	Heave	Roll	Pitch	Yaw
Surge	0	0	0	0	0	0
Sway	0	1013 kN/m	0	0	0	0
Heave	0	0	827 kN/m	0	0	0
Roll	0	25800 kN	0	696300 kNm	0	0
Pitch	0	0	0	0	0	0
Yaw	0	0	0	0	0	0

Table 5.4: Linearised mooring stiffness terms for pontoon 15 [24]

	Surge	Sway	Heave	Roll	Pitch	Yaw
Surge	0	0	0	0	0	0
Sway	0	826 kN/m	0	0	0	0
Heave	0	0	133 kN/m	0	0	0
Roll	0	8690 kN	0	116800 kNm	0	0
Pitch	0	0	0	0	0	0
Yaw	0	0	0	0	0	0

5.3.5 Cable-Stayed Bridge

Stay Cable Arrangements

The cable-stayed bridge was also modelled by use of master-slave supernode connections. For each pair of stay cable intersections at the bridge girder, three supernodes were defined. Slaved supernodes were modelled in the actual stay cable intersections, i.e. 13.8 meters east and west of the bridge girder neutral axis, respectively. For each pair of intersections, a master supernode was modelled in the bridge girder at the same longitudinal coordinate, ensuring the stay cable intersections to be rigidly connected to the bridge girder. The mentioned supernodes can be seen in figure 5.4.

In the tower it was done in a similar manner, except the top of the tower was set as the master node, hence simplifying the stay cables to be rigidly connected to the tower top. The arrangement can be seen in figure 5.5. The simplifications of the tower are further described in the following subsection.

The pre-tensions in the cables were set according to table 4.8 and 4.9. This was done in an iteration procedure where the stress-free lengths of the cables were changed. Iterations were needed mainly due to the change in deflection of the bridge girder. Some adjustments were needed in order to account for the mass of the cables.

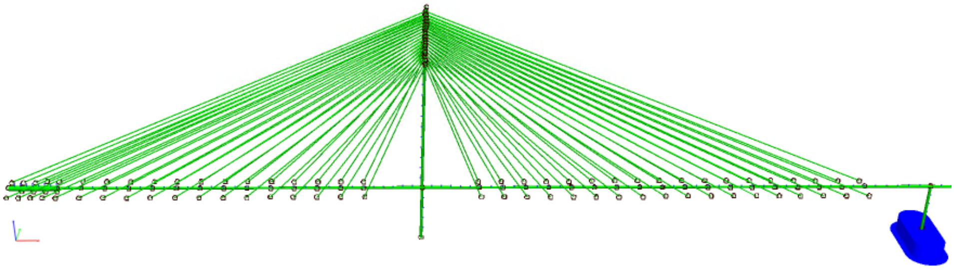

Figure 5.4: Side view of the cable stayed bridge showing the supernodes in the bridge girder

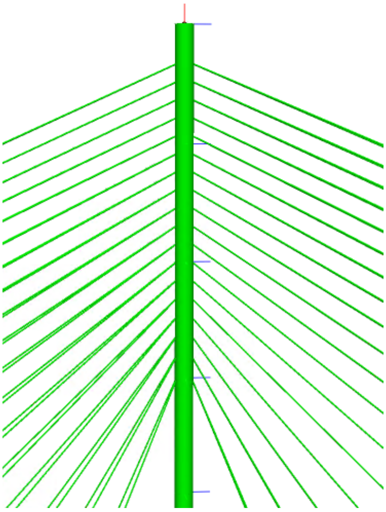

Figure 5.5: The arrangement of the stay cables in the tower

Tower

The placements of the stay cables in the tower and bridge girder, as well as the cable properties and tensions, were modelled based on the geometry and values specified for the bridge concept as given in *Bilag B* [24]. However, the tower was simplified due to its complex geometry. In the original concept, the tower has an A-shape, with varying cross-sectional properties along its height.

In the modelling performed in this thesis, the tower was simplified as a single beam with cross-sectional properties as given in table 5.5. These values were derived based on rough estimations from the detailed tower cross-sections presented in *Bilag B* [24]. The consequences of these simplifications are not assessed in detail in this report, as the response in the floating part of the bridge was considered to be of highest importance.

Table 5.5: Assumed cross-sectional properties of the tower

Parameter	Unit	Value
Axial stiffness	kN	$1.0 \cdot 10^9$
Bending stiffness	kNm^2	$5.0 \cdot 10^{10}$
Torsion stiffness	kNm^2	$5.0 \cdot 10^{10}$
Weight	tons/m	89.9

5.3.6 Structural Damping

According to the *Design Basis* [25] used by the design team for the concept, the values for the structural damping ratio for the steel parts of the bridge, i.e. the complete RIFLEX part of the model, should be between 0.5% and 0.8%.

The structural damping was as mentioned in 3.6.2 implemented in RIFLEX in terms of the Rayleigh-damping model. Consequently, a constant value for the structural damping ratio was not feasible. Therefore, the values of the proportional damping coefficients, α and β, in the Rayleigh formulation were chosen such that the damping ratio for a largest possible part of the expected response frequencies was held within the specified values of 0.5% and 0.8%.

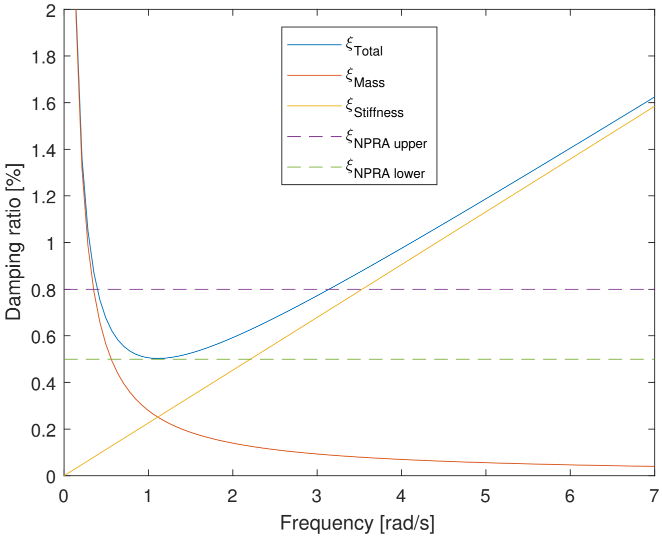

Figure 5.6: Rayleigh damping as included in the coupled SIMO-RIFLEX model

The damping coefficients were calculated by equation 3.50 and 3.51 at the ends of an increasingly larger frequency interval. This iteration procedure was stopped when the lower bound proposed for the damping ratio of 0.5% was the minimum value within this frequency interval.

This resulted in damping coefficients to be used in the time domain analyses of $\alpha = 0.0056$ and $\beta = 0.0045$, where α is the global mass proportional damping factor. As seen in figure 5.6, this ensured the structural damping ratio to be between 0.5% and 0.8% for response frequencies between 0.39 rad/s and 3.14 rad/s, oppositely corresponding to periods of 2 s and 16 s. By this procedure, the structural damping ratio at the period used in the regular wave analyses, T=6s, is 0.51%. For periods outside this range, the system will be over-damped.

Chapter 6

Results

In this chapter, first the hydrodynamic results of the pontoons will be presented, followed by a static, eigenvalue and dynamic analysis of the complete bridge model. Emphasis will be put on the response of the pontoons and the bridge girder. For all results plotted along the bridge girder, the vertical grid lines are placed such that each line goes through an initial pontoon location, except for the first line which goes through the tower in the cable-stayed bridge.

Results will be presented, described and discussed consecutively in order to ease referrals to figures and tables.

6.1 Hydrodynamic Results for the Pontoons

The properties of the pontoons play an important role when designing a floating bridge, not at least for a bridge of this record-breaking size when considering the environmental conditions in this specific fjord.

In order to ensure realistic results of the hydrodynamic analysis performed for the pontoon in Wadam, a convergence analysis was carried out, as presented in the next section. More results from the hydrodynamic analysis with the final mesh size are found in appendix A. This includes the diagonal terms of the frequency dependent added mass and damping and first order wave force transfer functions in all six rigid body modes for a wave direction of 225 degrees.

6.1.1 Convergence of Hydrodynamic Results

The convergence analysis was carried out by considering some of the characteristic frequency dependent coefficients since the non-frequency dependent results have been altered in SIMO. The coefficients chosen were the added mass and damping in surge, sway and heave, respectively, and the first order wave force transfer function in sway for the direction 90 degrees relative to the pontoon local x-axis, i.e. normal to the bridge.

The convergence analysis was performed by running four separate hydrodynamic analyses on panel models in Wadam with element sizes of 0.5 m x 0.5 m, 1 m x 1 m, 2 m x 2 m and 4 m x 4 m. Comparisons of the results for the chosen mesh sizes are shown in the following figures.

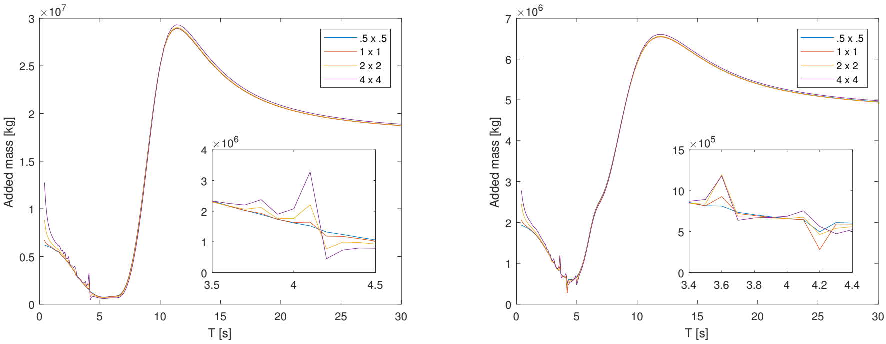

(a) Added mass in surge, A_{11}

(b) Added mass in sway, A_{22}

Figure 6.1: The added mass in surge and sway for four choices of mesh size

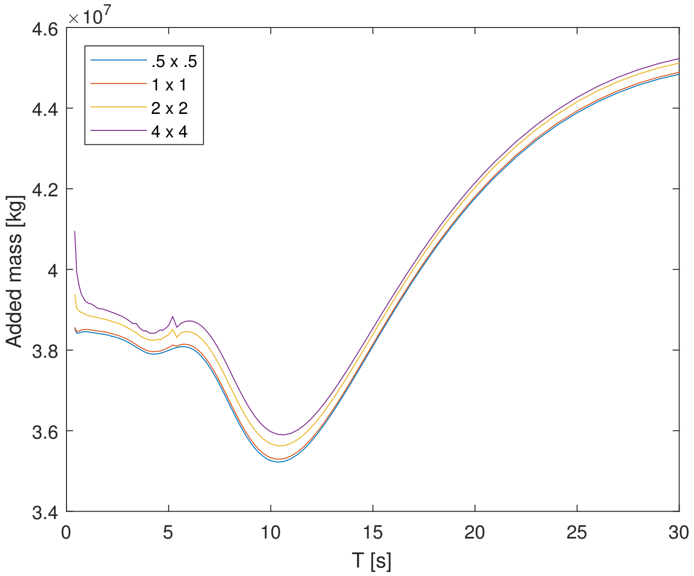

Figure 6.2: Added mass in heave, A_{33}, for four choices of mesh size

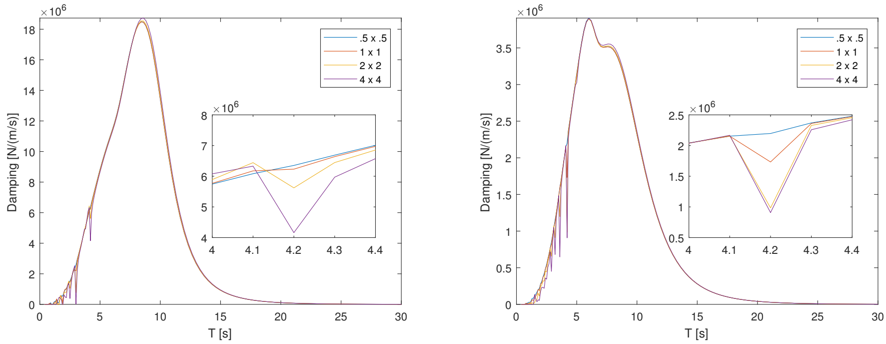

(a) Damping in surge, B_{11}

(b) Damping in sway, B_{22}

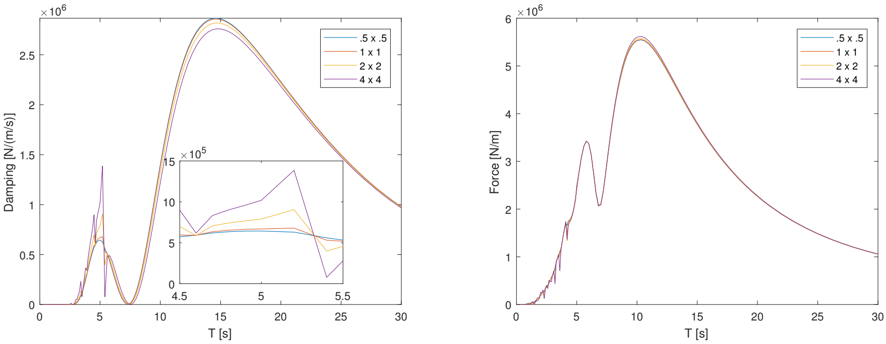

(c) Damping in heave, B_{33}

(d) First order wave force transfer function in sway for waves normal to the bridge

Figure 6.3: The radiation damping in surge, sway and heave and a first order transfer function in sway for four choices of mesh size

From figure 6.1, 6.2 and 6.3 it is seen that the results for all mesh sizes coincide well for periods above 7 seconds. The largest difference between the results for the coarsest and finest mesh size above this period is 5 %, and was found for the damping in heave.

For lower periods the results are seen to be far more sensitive on the mesh size, as the results for the coarser mesh sizes are fluctuating considerably due to irregular frequencies [27]. Also the results for the 1 m x 1 m mesh are fluctuating. The results for the finest mesh are fluctuating negligibly and are considered to be converged, except for at the period 4.2 s for added mass in sway. This leads to an underestimation of added mass of 22 % at this particular period. However, as frequency dependent added mass and damping are implemented in the time domain analyses by use of retardation functions, the deviations due to a few irregular frequencies are small. For the added mass in sway, the approximation errors introduced in general by the retardation function for the given choice of cut factor of

200 are larger than the error at the peak for the irregular period 4.2 second. This is shown in figure 6.4.

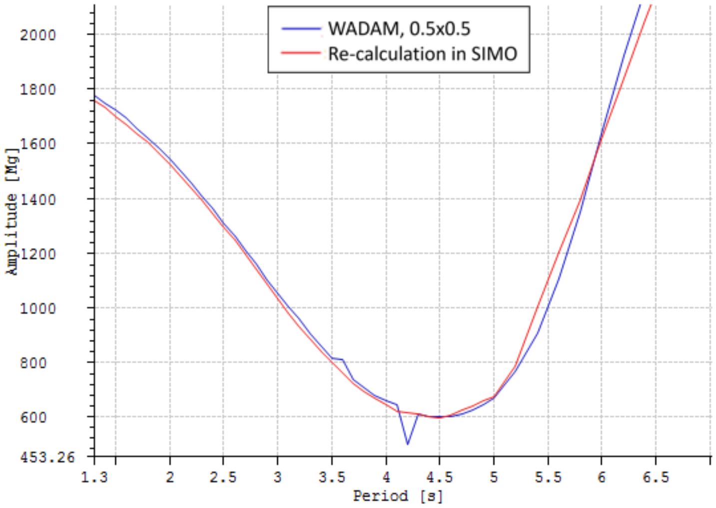

Figure 6.4: Added mass in sway as obtained in Wadam for the mesh size 0.5 m x 0.5 m and by the re-calculation in SIMO from the corresponding retardation function

In retrospect, it was discovered that Wadam has an option to remove these irregular frequencies which cause the mentioned local extreme values, and possibly the 1 m x 1 m mesh size would have been sufficient to ensure convergence. New analyses were not run due to the previous arguments and the fact that a small mesh size used by Wadam do not increase the simulation time in SIMO-RIFLEX.

The hydrodynamic results for the mesh size 0.5 metres x 0.5 metres were therefore used in the SIMO bodies in the coupled SIMO-RIFLEX model. The run times of the hydrodynamic analyses in Wadam are presented in table 6.1.

Table 6.1: Run time of hydrodynamic analyses performed in Wadam

Mesh size	Run time [s]
4 m x 4 m	71
2 m x 2 m	280
1 m x 1 m	630
0.5 m x 0.5 m	10600

6.2 Static Analysis

In the following section, the static results obtained for the bridge structure will be presented and discussed consecutively. Emphasis will be put on the results for the bridge girder due to its permanent loads, which as mentioned comprise of its steel weight and weight due to asphalt, railings, equipment, etc. The displacement of the bridge girder due to 70 % of the characteristic traffic load will be compared to criteria specified for the concept by its design team. Finally, the mooring system characteristics due to west-east displacement will be presented in order to justify the linearisation procedures used for the second model in the eigenvalue analysis.

6.2.1 Vertical Displacement

Figure 6.5 shows the displacement of the bridge girder relative to its initial position, whereas the initial position is the position of the structure as if it was infinite stiff. Therefore, it can be seen that the pontoons are ballasted such that the actual pontoon drafts differ from their design draft of 10.5 meters with a maximum of 2 mm.

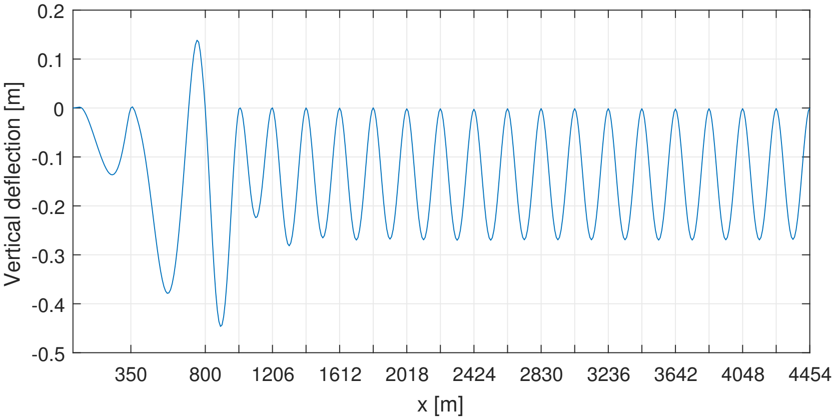

Figure 6.5: The vertical displacement of the bridge girder due to self weight

The maximum displacements of the bridge girder in the part of the bridge with a constant initial girder height, i.e. from x = 1815 m, are as expected seen to be equal, and with a magnitude of 27 cm. The overall maximum displacement is found in the first floating bridge span with a magnitude of 45 cm. This can be explained by the uplifting of the bridge girder at the end of the main span of the cable-stayed bridge, leading to less rotational stiffness at the first girder-column intersection about the girder weak axis, as well as a slight initial angle.

6.2.2 Bending Moments

The weak axis bending moments in the low part of the bridge, as seen in figure 6.6, are somewhat different than what one could expect by simplifying each girder span as a fixed beam with evenly distributed mass. The magnitude of the moments at the midspans is found to be 3.0 $\cdot 10^5$ kNm, whereas the absolute value of the moments at the girder-column intersections is 7.1 $\cdot 10^5$ kNm. This corresponds to 2.4 times the magnitude of the midspan moments, which is considered reasonable as the stiffest and heaviest cross-section of the bridge girder is located at these intersections.

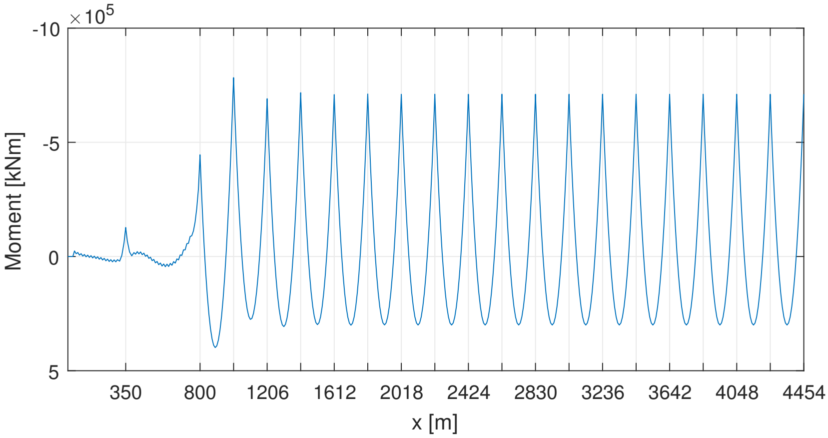

Figure 6.6: Weak axis bending moments in the bridge girder

The maximum moment is found at the end of the first floating bridge span, at the girder-column intersection above pontoon 2, with an absolute value of 7.9 $\cdot 10^5$ kNm. The reason why the largest moment is found here is as explained for the displacement pattern, due to the reduced rotational stiffness about the opposite girder-column intersection, as a consequence of the uplifting of the bridge girder.

The weak axis bending moments in the high bridge are seen to not be perfectly minimised, which is because the pre-tensions in the stay cables were not fully optimised accordingly. However, it should be noted that due to the previous arguments the main span is seen to affect the bending moments in the first few floating bridge spans, in which perfect main span moment minimisation would further increase the absolute value of the current maximum bending moment.

The bending moments about the bridge girder strong axis are negligible when the bridge is only subjected to self-weight. The same applies for the horizontal shear forces and the torsional moments in the bridge girder.

6.2.3 Shear Forces

The vertical shear forces in the bridge girder are seen to correspond to the distribution of the weak axis bending moments presented. The largest absolute value of the shear force in the low bridge is $2.0 \cdot 10^4$ kN and is found at the girder-column intersections. At the midspans, the shear forces are zero.

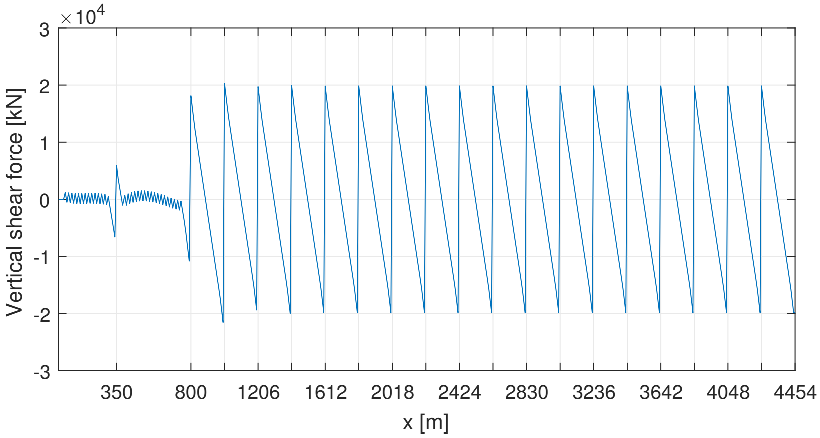

Figure 6.7: Vertical shear forces in the bridge girder

The largest absolute value of the shear force is as expected found at the same girder-column intersection as the largest bending moment, with an absolute value of $2.2 \cdot 10^4$ kN. When comparing the two graphs it should be noted that the y-axis for the bending moments is reversed.

6.2.4 Axial Forces

The axial force in the floating part of the bridge is negligible, as seen in figure 6.8, which means that the self-weight is carried by bending action. This was expected by investigating the shape of the bending moment graphs, as well as considering the relatively small vertical girder deflections.

In the cable-stayed bridge compression forces in the bridge girder are arising due to the horizontal components of the stay cables. Furthermore, it is seen that the tower is not absorbing any of the axial loads from the girder, as intended with the girder tower connection described in section 5.3.2.

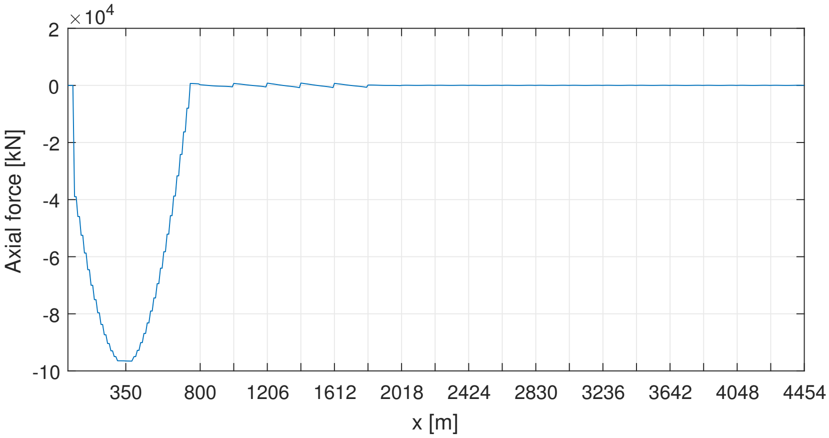

Figure 6.8: Axial forces in the bridge girder

6.2.5 Deflection due to Traffic

A motion criterion specified by the design team for the straight bridge concept is that the maximum displacement of the pontoons due to 70 % of the characteristic traffic load should be less than approximately 1 m. The distributed traffic load for the concept, found based on the Eurocodes presented in section 3.1.2, is 58.7 kN/m [2].

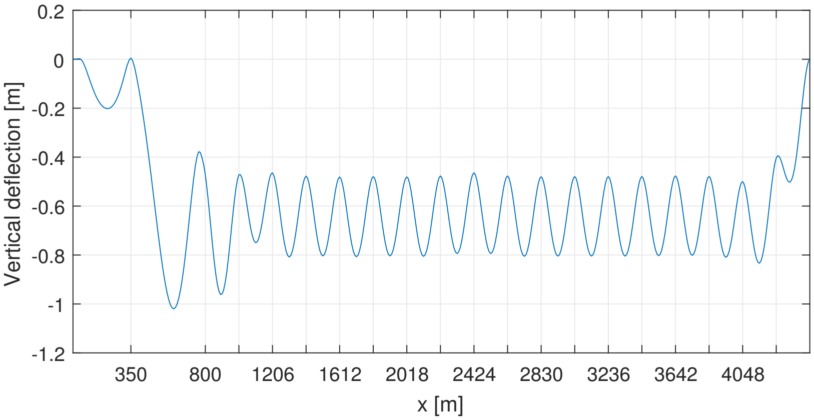

Figure 6.9: Vertical deflection of the bridge girder due to 70 % of the characteristic distributed traffic load

In figure 6.9 the maximum additional pontoon deflection is seen to be 0.51 metres, and is found for pontoon 17 at x = 4048 m. By simplifying the loads to be evenly carried by the pontoons in the floating bridge, the expected pontoon deflections are found to be similar from hand calculations.

$$Displacement = \frac{Load}{C_{33}} = \frac{70\% \cdot 58.7kN/m \cdot 203m}{17\ 477kN/m} = 0.48m \tag{6.1}$$

From the figure and hand calculations, it is clear that this criterion was not governing the design of the pontoon. According to Larsen [12], the pontoon was optimised with respect to the heave response for the curved bridge alternative.

6.2.6 Mooring Line Characteristics

As will be seen in the eigenvalue analysis, the complete coupled model, which includes the catenary mooring system as modelled in RIFLEX, proved to give large deviations in the eigenvalues compared to those obtained by the NPRA for the modes above number six.

Consequently, some of the mooring line characteristics are analysed in this section in order to verify that the mooring system has been implemented as specified in the original bridge concept.

Mooring Line Tensions

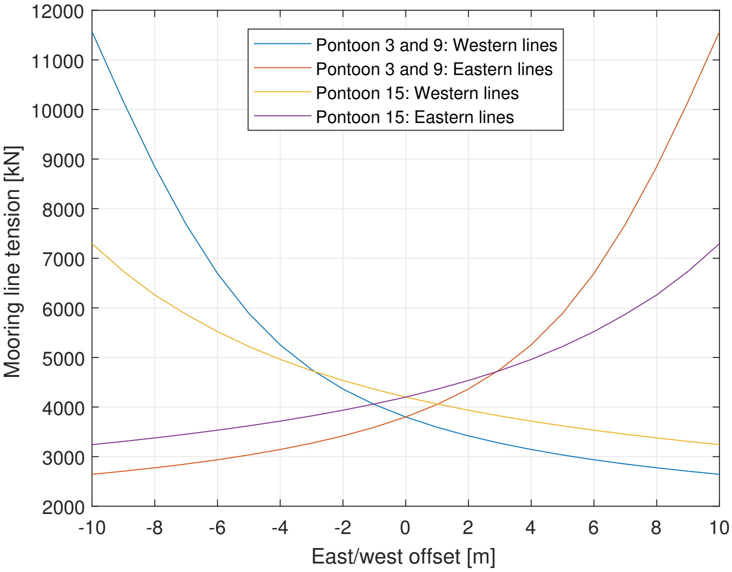

Figure 6.10: Individual mooring line tension due to east-west pontoon displacement

Figure 6.10 shows the individual mooring line tensions at the fairleads due to east-west pontoon displacement. It is seen that the pre-tensions at the design offset are 3800 kN and 4200 kN, respectively, as specified by the NPRA [2].

Resulting System Stiffness

By including the mooring line angles at the fairleads, the horizontal and vertical mooring forces can be calculated. Figure 6.11 shows the resulting mooring system force for the respective pontoons in the east-west direction due to east-west pontoon displacement. It is seen that the mooring system characteristics are non-linear. This is quantified by table 6.2, which shows the resulting mooring stiffness calculated at intervals of 0.5 metres and 1 metre for pontoon 3 and 9. The stiffness for the first metre, 1066 kN/m, is differing by 5 % compared to the value obtained by the NPRA, 1013 kN/m.

The stiffness term for the first metre of offset for pontoon 15 is seen to be 872 kN/m, compared to the value of 827 kN/m obtained by the NPRA [24]. The stiffness terms obtained by the NPRA were as mentioned used in the linearisation of the mooring system. The small differences obtained by RIFLEX might be due to the number of elements chosen in the analysis, which the mooring lines' vertical angle at the fairleads, as well as the tension forces, are dependent on.

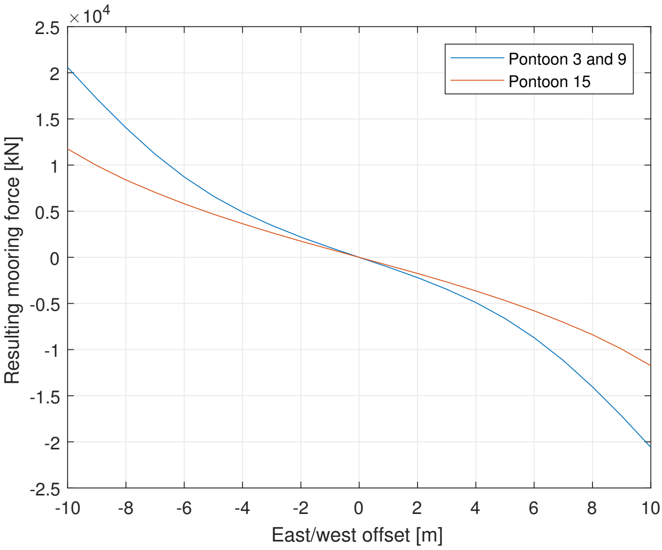

Figure 6.11: Resulting mooring force in the east-west direction due to east-west pontoon displacement

Table 6.2: Resulting mooring stiffness for pontoon 3 and 9 in the east-west direction due to east-west displacement

Step	Stiffness [kN/m]
0-0.5 m	1061
0.5-1 m	1071
0-1 m	1066
1-2 m	1131
2-3 m	1264
3-4 m	1436
4-5 m	1727
5-6 m	2084
6-7 m	2466
7-8 m	2865
8-9 m	3154
9-10 m	3395

The resulting mooring moments about the bridge girder longitudinal axis due to east-west pontoon displacement, see figure 6.12, were found by summing the vertical mooring force components multiplied by the respective lateral distances from the pontoon centre to the fairleads. The mooring moment stiffness for the first metre of offset for pontoon 3 and 9 and pontoon 15 are found to be 27541 kNm/m and 9074 kNm/m, respectively.

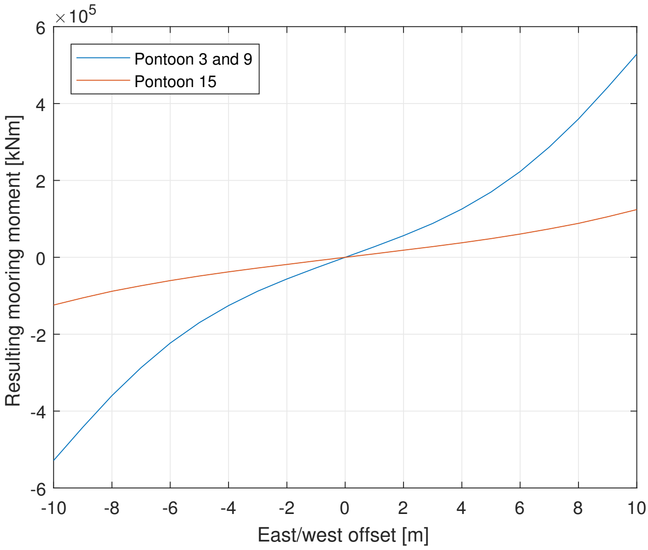

Figure 6.12: Resulting mooring moments about the girder longitudinal axis due to east-west pontoon displacement

Also the mooring moments are seen to be non-linearly related to the offset. In general, the non-linear characteristics of the mooring system can be explained by the catenary shapes of the mooring lines, caused by the large self-weight.

6.3 Eigenvalue Analysis

In this section, the results from the eigenvalue analyses performed for the model with the catenary mooring system and the model with the linearised mooring system will be presented and discussed. It should be stressed that these models are identical, except for their mooring systems.

As shown in table 6.4, the original model, which includes the catenary mooring system as modelled in RIFLEX, proved to give large deviations in the eigen periods compared to those obtained by the NPRA for mode 7 and higher. As part of a troubleshooting process, a linearised mooring system was implemented in a second model, as described in section 5.3.4, which gave eigen periods considerably closer to those obtained by the NPRA.

The reason why the two models gave significantly different results was not identified. A possible reason is that RIFLEX is not able to fully account for the catenary mooring lines in the calculation procedures in the eigenvalue analysis. However, the eigenvalue analysis chapter in the RIFLEX Theory Manual [19] is not written, such that further details were not found.

Additionally, since SIMO-RIFLEX does not consider frequency dependent added mass in the eigenvalue calculations, the eigen periods for the models, as given in the columns *Cat. mooring* and *Lin. mooring* in table 6.4, were obtained by the use of the infinite-frequency added mass matrix as calculated by SIMO. This matrix is given in table 6.3, where *te* is tons.

Table 6.3: The infinite-frequency added mass matrix as calculated by SIMO

	Surge [te]	Sway [te]	Heave [te]	Roll [te·m]	Pitch [te·m]	Yaw [te·m]
Surge	12049	0	0	0	$-1.08 \cdot 10^5$	0
Sway	0	3252	0	40979	0	0
Heave	0	0	40706	0	0	0
Roll [m]	0	40992	0	$1.17 \cdot 10^7$	0	0
Pitch [m]	$-1.08 \cdot 10^5$	0	0	0	$3.22 \cdot 10^6$	0
Yaw [m]	0	0	0	0	0	$1.86 \cdot 10^6$

The *added mass iterated* eigen periods were calculated in SIMO-RIFLEX by the use of the model with the linearised mooring system, where the added mass infinite frequency matrix was manually changed for each eigenvalue analysis specifying a new T_A. This procedure is a time-consuming process, such that it was only included for a few periods for illustration purposes. For each T_A the added mass coefficients were read from the Wadam result file by a MATLAB script. These coefficients are as mentioned also plotted in appendix A.

The eigen periods presented in the NPRA column are those obtained in the reference report and include the contribution from frequency dependent added mass [28].

6.3.1 Eigen Periods and Dominating Mode Motions

Table 6.4: The first 35 eigen periods compared with the values obtained by the NPRA

	NPRA[a]	Cat. mooring[b]		Lin. mooring[b]		Added mass iterated[c]		
Mode	T [s]	T [s]	Diff [%]	T [s]	Diff [%]	T [s]	Diff [%]	$T_A[s]$
1	78.25	74.66	−4.7	74.83	−4.5	77.52	−0.9	78.25
2	71.21	68.23	−4.3	68.48	−3.9	70.92	−0.4	78.25
3	40.78	39.85	−2.3	38.94	−4.6	40.32	−1.1	78.25
4	32.48	31.51	−3.0	30.91	−5.0	31.95	−1.6	78.25
5	23.44	22.72	−3.1	22.49	−4.1			
6	17.69	16.95	−4.3	16.90	−4.6			
7	14.09	16.24	14.2	13.16	−6.8	14.22	0.9	14.09
8	14.09	16.23	14.1	12.33	−13.3	13.82	−2.0	14.09
9	13.06	16.23	21.6	12.15	−7.3			
10	11.45	16.22	34.5	11.59	1.2			
11	11.32	16.22	35.6	11.57	2.2			
12	10.92	16.22	39.1	11.54	5.5	11.09	1.5	10.88
13	10.89	13.33	20.1	11.54	5.8	11.06	1.5	10.88
14	10.88	13.10	18.5	11.49	5.4	11.03	1.4	10.88
15	10.87	13.08	18.5	11.45	5.2	11.01	1.3	10.88
16	10.87	13.08	18.4	11.29	3.8	10.99	1.1	10.88
17	10.84	13.08	18.7	11.11	2.4	10.97	1.2	10.88
18	10.76	13.07	19.4	11.04	2.6	10.85	0.8	10.88
19	10.66	13.07	20.3	11.01	3.3	10.83	1.6	10.88
20	10.50	13.07	21.8	10.84	3.2	10.72	2.1	10.88
21	10.32	13.06	23.5	10.55	2.2			
22	10.02	13.06	26.4	10.26	2.4			
23	9.79	13.06	28.6	10.23	4.4			
24	9.73	13.06	29.2	9.84	1.2			
25	9.51	13.06	31.5	9.51	0.0			
26	9.08	12.66	32.9	9.50	4.5			
27	8.85	12.13	31.2	9.10	2.8			
28	8.61	11.73	30.7	8.70	1.0			
29	8.33	11.68	33.5	8.64	3.7			
30	8.21	11.63	34.4	8.30	1.1			
31	7.84	11.58	38.6	8.16	4.0			
32	7.62	11.54	40.9	8.02	5.2			
33	7.45	11.48	42.6	7.65	2.7			
34	7.08	11.35	46.3	7.52	6.1			
35	6.49	11.25	53.7	7.08	8.7			

[a] Frequency dependent added mass considered

[b] Only the infinite-frequency added mass matrix considered

[c] Added mass considered at periods specified by T_A for the model with the linearised mooring system. See appendix A for the diagonal added mass coefficients.

As seen in table 6.4, the eigen periods for the linearised mooring system where the added mass coefficients were updated, yield small deviations from the values obtained by the NPRA. The significance of added mass is especially obvious for mode 8. As expected from the former observations and as seen in table 6.5, also the dominant motions and mode shapes are dependent on the added mass. The small deviations obtained when updating added mass give implications that the stiffness and mass properties of the bridge structure and pontoons, as well as the boundary conditions, were modelled correctly.

In the dominant motions calculations, only the translational motions of the bridge girder were considered for the motions obtained for the *catenary mooring system* and *linearised mooring system* columns. Rotations were not included due to uncertainty regarding the choice or choices of a or several characteristic lengths to multiply with the rotational motions, given in radians per second, when comparing to the translational motions in metres. The determination of the rotational motions for the *added mass iterated* column was done by visual inspection of the mode shapes in SIMA, and are seen to coincide well with the dominant motions obtained by the NPRA, which also considered rotational motions.

As shown in the table containing the first 75 eigen periods in appendix B.1, the differences between the eigen periods calculated for the model with the linearised mooring system and the NPRA increase from 10 % at mode 56 and up to 46.4 % at mode 75. Only differences of a few percentages can be explained by the implementation of added mass, as tested by setting the added mass to zero. Higher values of the added mass yield larger differences, as expected from equation 3.37.

Sensitivity tests to most parameters defining the model in SIMO-RIFLEX were performed, however, the reason for the differences at higher modes was not found. As seen in the appendices [28] for the reference report, these modes are coupling of motions in at least two degrees of freedom. A possible reason can be that some stiffness terms were neglected for the linearised mooring system, whereas only the terms specified in section 5.3.4 were included. In addition, the linearisation of the catenary mooring system in the eigenvalue calculation codes in the software used by the NPRA could possibly lead to some differences.

Table 6.5: Comparison of dominant motions for the first 35 modes

Mode	NPRA[a]	Cat. mooring sys.[b]	Lin. mooring sys.[b]	Added mass it.[c]
1	Y	Y	Y	Y
2	Y	Y	Y	Y
3	Y	Y	Y	Y
4	Y	Y	Y	Y
5	Y	Y	Y	Y
6	Y	Y	Y	Y
7	X	X	Y	X
8	Y	Y	Y	Y
9	RX	X	Z	RX
10	Z	Y	Z	Z
11	RX	Y	Z	RX
12	Z	Y	Z	Z
13	Z	Y	Z	Z
14	Y	Z	Z	Z
15	Z	Z	Z	Z
16	Z	Y	Z	Z
17	Z	Y	Z	Z
18	Z	X	Z	Y
19	Z	Z	Y	Z
20	Z	Y	Z	Z
21	Z	Y	Z	Z
22	Z	Y	Y	Z
23	Z	Y	Z	Z
24	RX	Y	Z	Z
25	Z	Y	Y	RX
26	Z	Y	Z	Z
27	Y	Z	Z	Y
28	Z	Z	Z	Z
29	RX	Z	Y	Z
30	Z	Z	Z	RX
31	Z	Z	Y	Z
32	Z	Z	Z	Y
33	Y	Z	Z	Z
34	RX	Z	Y	Z
35	Y	Y	Y	RX

[a] Frequency dependent added mass considered

[b] Only the infinite-frequency added mass matrix and the translational motions of the bridge girder were considered

[c] The model with the linearised mooring system. Added mass for each mode were considered at a period equal to the closest period specified by T_A in table 6.4

6.3.2 Important Modes for Wind and Wind-Driven Sea

In this section, some of the modes that are important for the 100-year wind waves and 100-year wind will be plotted and presented. The former is specified by a sea state with a significant wave height of 3 metres and peak period of 6 seconds, with the main direction from west, 270 degrees [2]. The wind is described as slowly varying and has the same direction as the wind-driven waves. Emphasis will be put on presenting the modes important for dynamic amplifications of the strong and weak axis bending moments, respectively.

The mode shape plots are either presented in the vertical plane, xz, or the horizontal, xy. This is because one of these directions is significantly dominant relative to the other for the mentioned modes. Consequently, when plotted in relative size for each mode, only motion in one direction is visually seen. In the mode shape plots, the pontoons are held fixed in their initial configuration in order to better visualise the motions of the bridge girder and columns. The mode shapes are obtained for the model having the linearised mooring system where added mass coefficients are updated according to table 6.4. For the modes where a T_A value is not specified, the added mass were considered at the closest specified value.

Mode shape plots for the first 75 modes are given in appendix B.2. From these it can be seen that the first 11 mode shapes are coinciding with those obtained by the NPRA. Mode 12 and 13 have switched place. For higher modes, not all mode shapes are coinciding with those obtained by the NPRA.

Strong Axis Bending Moments

The mode shapes given in figure 6.13 are for modes important for the strong axis bending moments due to wind, or more specifically slowly varying gusts. At the first four of these periods, the radiation damping of the pontoons in sway is negligible, as shown in figure 6.3. Especially the same four modes are expected to be dominated by response due to wind because of their high periods, i.e. above those expected for wave loads.

Figure 6.14 shows two modes which are important for the strong axis bending moments due to wind-driven waves, as they are dominated by lateral motions at periods close to the peak period. By studying appendix B.2 it can be seen that several modes around 6 seconds are dominated by roll motion of the bridge girder. These are important for the torsional moments in the bridge girder.

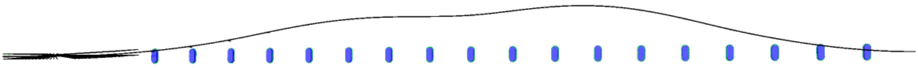

(a) Mode 1, xy-plane

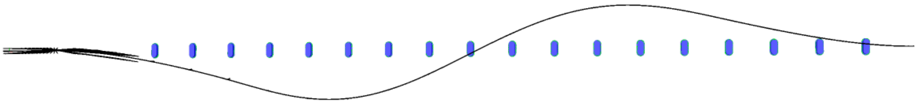

(b) Mode 2, xy-plane

(c) Mode 3, xy-plane

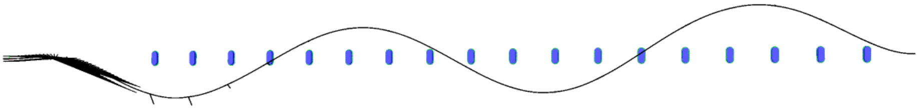

(d) Mode 4, xy-plane

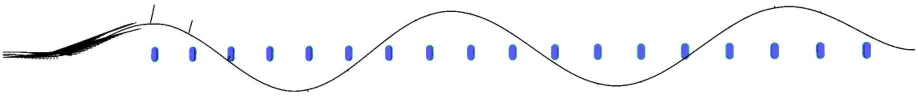

(e) Mode 5, xy-plane

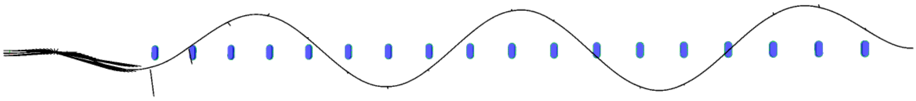

(f) Mode 6, xy-plane

Figure 6.13: Modes important for strong axis bending moments due to wind. Dominated by motion in the lateral direction. The latter three also have some torsional motion of the bridge girder

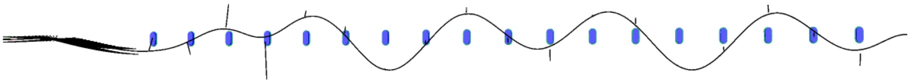

(a) Mode 39, T = 6.01 s, xy-plane

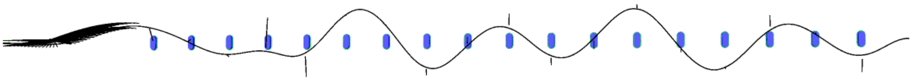

(b) Mode 41, T=5.43s, xy-plane

Figure 6.14: Two of the important modes for strong axis bending moments due to wind-driven waves. Dominated by motion in the lateral direction. Also some torsional motion of the bridge girder.

Weak Axis Bending Moments

In this section, some of the important modes for the weak axis bending moments in the bridge girder are presented. Figure 6.15 shows the initial configuration of the bridge structure in the xz-plane and is included in order to fully understand the following plots. As previously stressed, the model with the linearised mooring system was used for all mode shape plots presented in the thesis.

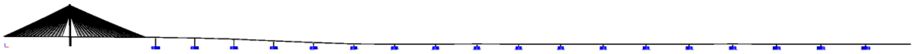

Figure 6.15: Bridge without the catenary mooring system in the initial condition in the xz-plane

Weak axis bending moments in the bridge girder are mainly induced due to surge and heave motions of the pontoons. This is shown in section 6.4.2. Figure 6.16 shows important modes in wind-driven sea dominated by surge motion of the pontoons. These motions are as expected largest for the pontoons attached to the longest columns. Also some heave motions of the pontoons are present.

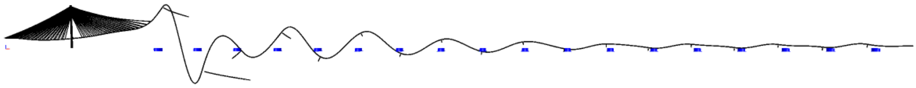

(a) Mode 36, T = 6.71 s, xz-plane

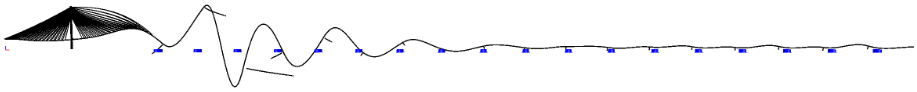

(b) Mode 38, T = 6.07 s, xz-plane

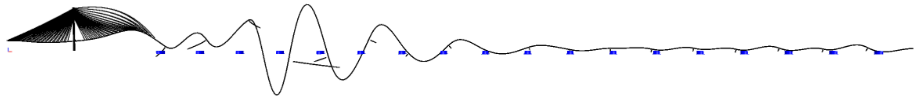

(c) Mode 42, T = 5.63 s, xz-plane

Figure 6.16: Three of the important modes for weak axis bending moments due to wind-driven waves. Dominated by surge motion of the pontoons. Secondary motion in the vertical direction.

Figure 6.17 shows the shortest modes dominated by heave motions. These modes are seen to be outside the range of periods containing the most energy in the Jonswap spectrum for the 100-year wind-driven sea. The first mode dominated by heave motions is mode 12 at a period of 11.09 seconds. This mode is given in figure 6.18. The latter period is below the corresponding period ranges for the 100-year swell sea state, specified by a significant wave height of 0.4 metres and peak periods of 12-14 seconds [2]. The heave dominated eigen periods obtained by the NPRA [28] are in the range of 7.5 to 10.95 seconds compared to 7.52 to 11.09 seconds obtained for the model with the linearised mooring system.

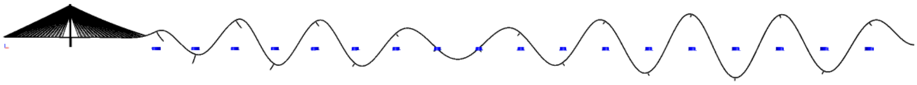

(a) Mode 33, T = 7.65 s, xz-plane

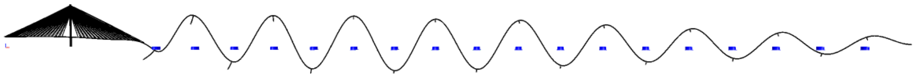

(b) Mode 34, T = 7.52 s, xz-plane

Figure 6.17: The shortest modes dominated by heave motions

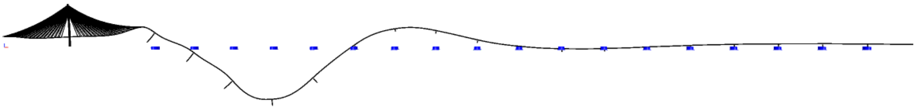

Figure 6.18: Mode 12, T=11.09s. The first mode dominated by heave motions

6.4 Response in Regular Waves

In this section, the global response of the bridge girder and the pontoons in regular waves will be presented and discussed. Analyses in irregular waves were not included due to extremely long simulation time, as a result of the coupled bridge model's complexity. First, the bridge will be subjected to waves at several wave heights for a given period. The focus will be on examining for linearity in response for the given condition. This is done because it can possibly reveal errors done in the modelling, as well as give an impression of the significance of the non-linearity of the mooring system and the total system stiffness. This analysis is done as a screening, not a complete sensitivity analysis.

In the next section the bridge will be subjected to waves at three directions, respectively, and the response described in detail. All dynamic analyses in this thesis were run for the model containing the catenary mooring system in regular waves at a *period of 6 seconds*.

6.4.1 Linearity in Response

In order to check for linearity in response for a certain set of conditions, the bridge was subjected to regular waves at several wave heights for a given period and direction. The period was chosen to 6 seconds, which according to Larsen [2] is the peak period for wind-driven sea for the 100-year storm. The wave direction was correspondingly set to 270 degrees. The wave heights were chosen with equal steps of 2 metres, from 1 to 9 metres.

Strong Axis Bending Moments

Due to the waves coming from west, i.e. normal to the bridge, the dynamic strong axis bending moments in the bridge girder were checked for linearity for the chosen wave heights. This was expected to be the dominating bending moment, as well as the most sensitive to non-linearity in response due to the catenary mooring system.

Figure 6.19 shows the dynamic maximum and minimum bending moments in the bridge girder after the responses have reached a steady state condition. This will be illustrated in the next section. It should be recalled that the strong axis bending moment is negligible in the static condition. From the mentioned figure it is seen that the moments for all wave heights follow the exact same pattern, implying linearity in response. This is proved by figure 6.20 which shows the dynamic range in strong axis bending moments for two locations for the bridge girder. The chosen locations were the girder-column intersection above pontoon 15 at x = 3642 m and at the northern abutment, i.e. the locations with the most significant peaks in the bending moments.

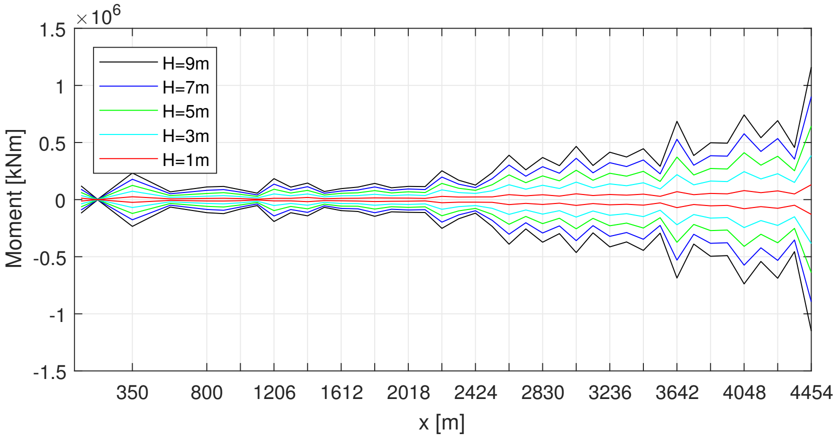

Figure 6.19: Dynamic maximum and minimum strong axis bending moments in the bridge girder due to regular waves with T= 6s, direction = 270 degrees and heights 1, 3, 5, 7 and 9 metres, respectively

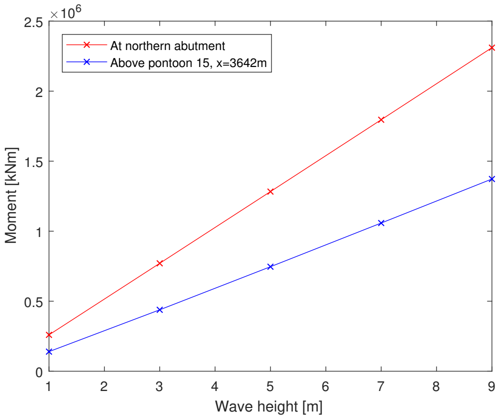

Figure 6.20: Range of dynamic strong axis bending moments in the bridge girder at the northern abutment and above pontoon 15, at x = 3642 m, in regular waves with T= 6s and direction = 270 degrees

Pontoon Motions

In order to justify the linearity in the strong axis dynamic bending moments, as well as checking for linearity in the vertical direction, corresponding plots for the pontoon motions in the lateral and vertical directions were made. Only the odd-numbered wave heights were included in the plots in order to maintain readability.

From figure 6.21 the total lateral motion ranges are visually seen to be linearly related to the wave heights. This is proved in figure 6.23a for the pontoons holding the mooring lines, as well as for pontoon 17 which has the largest dynamic motion range.

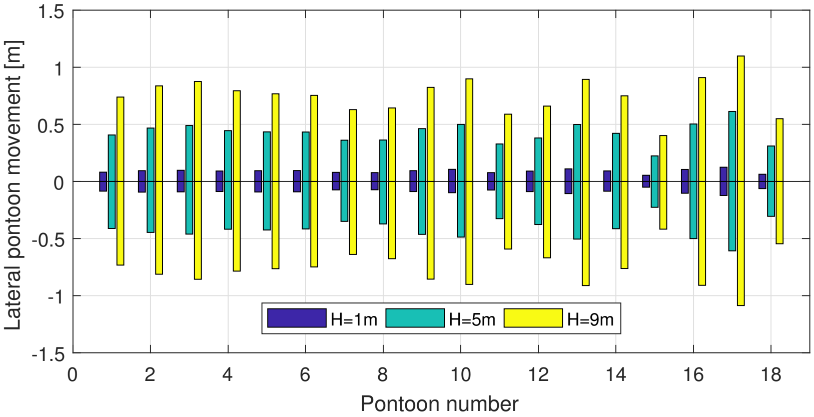

Figure 6.21: Lateral pontoon motions in regular waves with T= 6s, direction = 270 degrees and heights 1, 5 and 9 metres, respectively

By comparing the motions of the pontoons holding the mooring lines, which have a maximum horizontal motion of about 0.9 metres for pontoon 3, with the resulting mooring system forces and moments as presented in figure 6.11 and 6.12, the linearity in the lateral pontoon motions seems reasonable.

Both the mentioned resulting mooring stiffness terms are seen to be close to linear for the first two metres of lateral pontoon displacement. For the first metre, this can be quantified by comparing the mooring stiffness terms in the east-west direction due to east-west pontoon displacements in steps of half a meter, as presented in table 6.2. This yields a difference in stiffness of only 0.9 %. The linearity in the lateral pontoon motion ranges also implies that the significance of the quadratic drag forces on the mooring lines is of small importance for this given case.

In figure 6.22 the vertical pontoon maximum and minimum motions are seen to not be symmetric about the design draft. A possible reason can be due to the way the hydrostatic stiffness terms are implemented in the software. The stiffness references of the pontoons are specified by global coordinates, i.e. the restoring forces are not directly a function of the change in submerged volume of the pontoon. However, as shown in figure 6.23b the total motion ranges are close to linear for the examined wave heights, whereas the ranges increase slightly above linear for the higher wave heights.

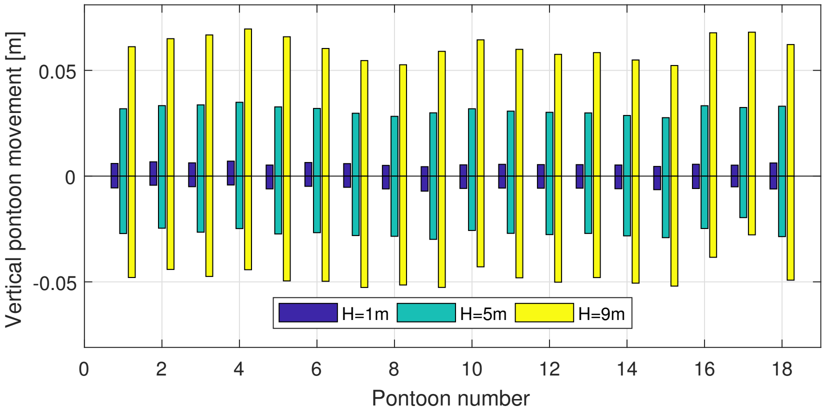

Figure 6.22: Vertical pontoon motions in regular waves with T= 6s, direction = 270 degrees and heights 1, 5 and 9 metres, respectively

Due to the asymmetry in the pontoon motions, non-linearity in the total motion ranges is reasonable. Since the pontoons were moving in phase for the wave direction 270 degrees, as shown in figure 6.24b, the vertical stiffness contributions due to bending of the bridge girder will only be dependent on the relative difference in magnitude of pontoon motions for nearby pontoons. These contributions will therefore also be asymmetric about the design draft. The non-linearity in the vertical mooring stiffness is not expected to be the reason, due to the small magnitudes relative to the vertical hydrostatic stiffness and because this in case should increasingly restrict positive vertical motion with motion amplitude.

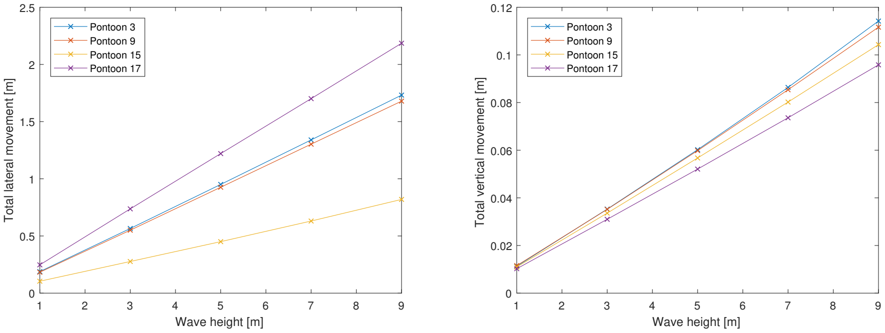

(a) Total lateral motion

(b) Total vertical motion

Figure 6.23: Total lateral and vertical motions of pontoons 3, 9, 15 and 17, respectively, in regular waves with T = 6 s and direction = 270 degrees

6.4.2 Global Response in Different Wave Directions

In the following section characteristic global responses of the bridge structure are analysed in regular waves from the directions 270, 240 and 225 degrees, respectively. The period and wave height were chosen to 6 seconds and 3 metres, respectively, which as mentioned correspond to the peak period and the significant wave height for wind-driven waves for the 100-year storm [2]. In addition, the directions 255 and 210 degrees were analysed, but the former directions were chosen as these show some of the characteristic response patterns, and to maintain readability of the graphs. First, the pontoon motions will be presented, followed by the dynamic equivalent of the plots given in the static analysis.

The plots in this section will be on the same form as in section 6.4.1, i.e. as envelope plots. This means that the graphs show the maximum and minimum response magnitudes subtracted for the static value. Consequently, information on the time dependency is lost. The minimum and maximum values are found after the responses have reached steady state, which for all responses are seen to occur within 200 seconds. Examples of responses as function of time are given in figure 6.24a and 6.24b.

All values related to the bridge girder are found at the nodes located at the girder-column intersections and at the mid-spans. This will be commented on for the plots where this lead to significant underestimations or if the exact shapes of the responses are of importance.

Pontoon Motions

In this section, the pontoon motions will be briefly described. These will primarily be used as a tool in order to describe the responses in the bridge girder.

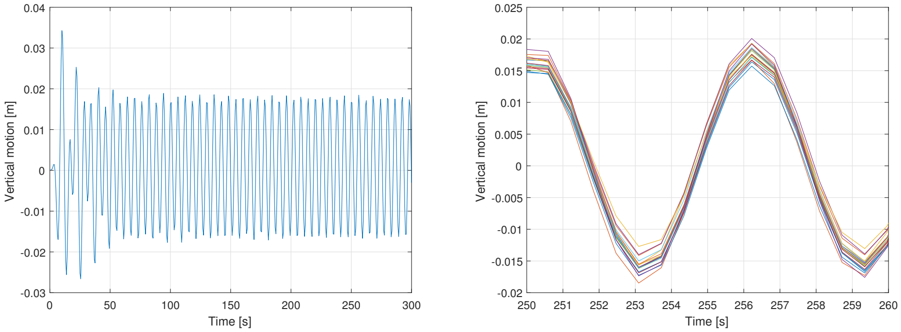

(a) Pontoon 1

(b) All pontoons

Figure 6.24: Vertical pontoon motions as function of time in regular waves with H = 3 m, T = 6 s and direction = 270 degrees

Figure 6.24a shows the vertical motions of pontoon 1 plotted as function of time. For this case, the transients effects are seen to be dominant in about the first 60 seconds. From figure 6.24b it is seen that all pontoons move in phase with the response period equal to the wave period, i.e. 6 seconds, when the bridge is subjected to the mentioned waves from west. The former is expected since the waves hit the pontoons simultaneously. For the other wave directions the pontoons are moving out of phase, but with the response period equal to the wave period of 6 seconds.

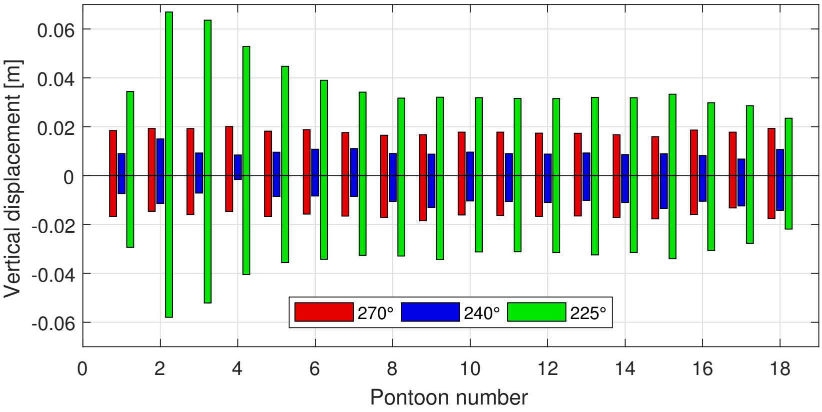

Figure 6.25: Vertical pontoon motions in regular waves with H = 3 m, T = 6 s and directions 225, 240 and 270 degrees, respectively

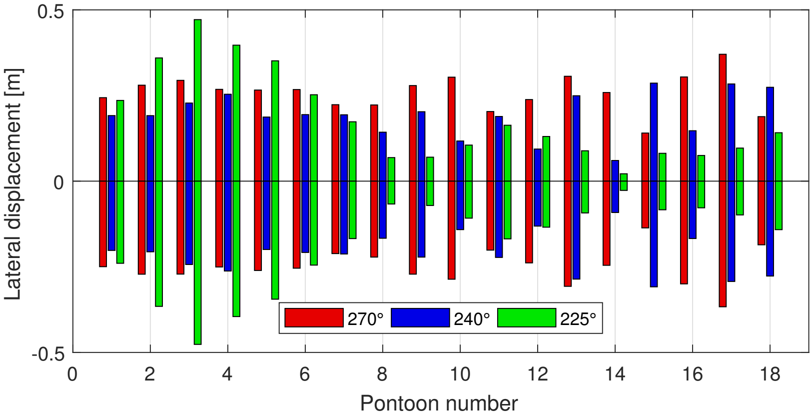

Figure 6.26: Lateral, west-east, pontoon motions in regular waves with H = 3 m, T = 6 s and directions 225, 240 and 270 degrees, respectively

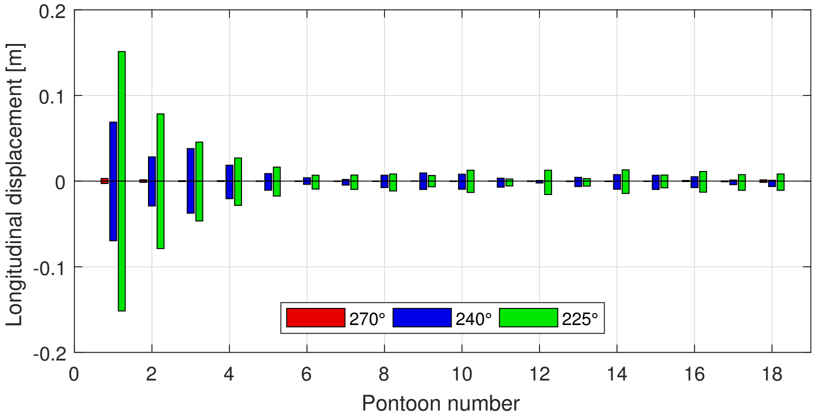

Figure 6.27: Pontoon motions along the bridge girder (surge) in regular waves with H = 3 m, T = 6 s and directions 225, 240 and 270 degrees, respectively

Figure 6.25, 6.26 and 6.27 show the maximum and minimum pontoon displacements in the vertical, lateral and longitudinal directions, respectively. Some characteristic motion patterns are seen.

Waves from 225 degrees led to the highest vertical displacements of the pontoons despite the first order wave force transfer functions in heave being about 530 kN/m, 400 kN/m and 460 kN/m for the wave directions 270, 240 and 225 degrees, respectively. The out off phase and surge motions induced by the direction 225 degrees are therefore seen to be of importance, as the pontoons are exited in a motion pattern similar as for the pendulum modes 36 and 38, as shown in figure 6.16.

For the lateral pontoon displacements in the wave direction 240 degrees, every second pontoon from number 7 to 17 are seen to have significantly larger displacement ranges. For the two other directions, there are wave-like patterns in the displacement. These observations will be commented on in the *Bending Moments* section.

Bridge Girder Motions

The maximum and minimum bridge girder motions are identical to the corresponding magnitudes of the bridge girder accelerations when subjected to regular waves. This is because the girder motions are sine functions with constant period equal to the wave load period. These plots are given in figure 6.34 and 6.35 in the *Bridge Girder Accelerations* section and will therefore be referred to when the bridge girder motions are used to describe responses.

Bending Moments

In this section, both the dynamic weak and strong axis bending moments in the bridge girder are presented.

The weak axis bending moments, as given in figure 6.28, are seen to increase as the wave direction is put closer to the bridge longitudinal axis. By comparing these moments with the pontoon motions, it is observed that the vertical motions for the direction 270 degrees are larger than for the direction 240 degrees, despite the latter direction inducing larger bending moments. Therefore, it is evident that the surge motions of the pontoons, i.e. pontoon motions along the bridge girder longitudinal axis, give a significant contribution to the weak axis bending moments. This is seen clearly for the direction 240 degrees: the vertical motions of pontoon 2, at x=1003m, are larger than for the adjacent pontoons while the longitudinal smaller, leading to the weak axis bending moment being smaller in this girder-column intersection.

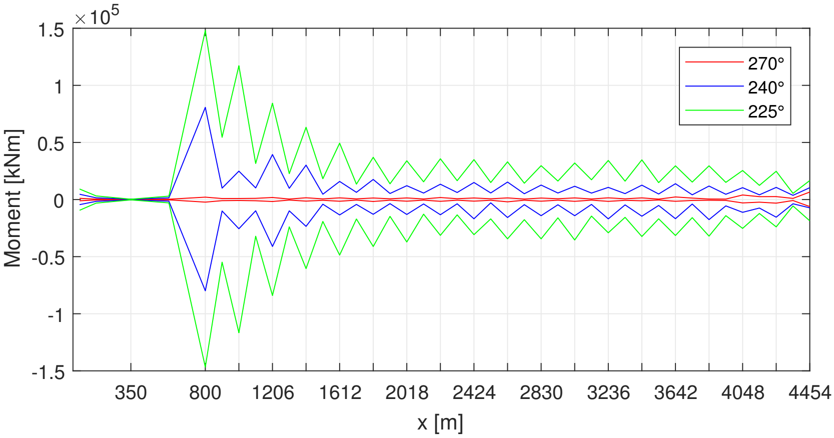

Figure 6.28: Dynamic max and min weak axis bending moments in regular waves with H = 3 m, T = 6 s and directions 225, 240 and 270 degrees, respectively

From figure 6.28 it is also seen that the largest dynamic moments occur at the girder-column intersections, which are at the same locations as the maximum static weak axis bending moments. The maximum dynamic weak axis bending moment for the bridge girder is found to be $1.5 \cdot 10^5$ kNm for the examined wave conditions. This corresponds to 19 % of the largest static bending moment, which in section 6.2.2 was found to be $7.9 \cdot 10^5$ kNm. However, these maxima are not at the same location. The largest combined weak axis bending moment is $9.1 \cdot 10^5$ kNm, and is found at the girder-column intersection above pontoon 2, i.e. at x=1003m. For this intersection, the dynamic bending moment consists of 15 % of the total moment.

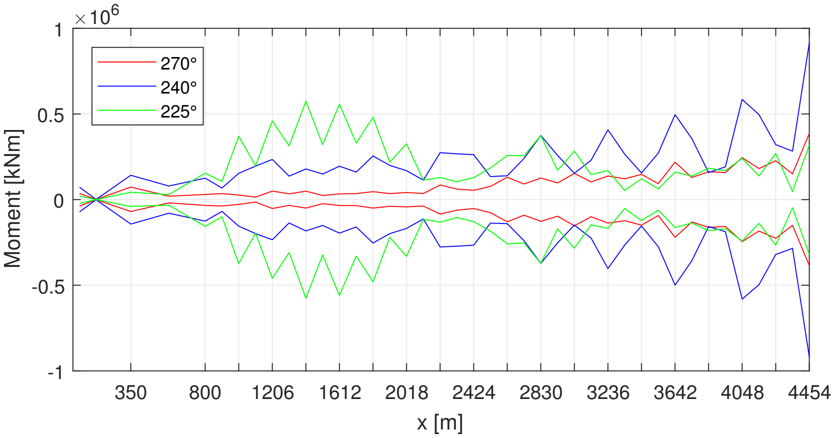

Figure 6.29: Dynamic max and min strong axis bending moments in regular waves with H = 3 m, T = 6 s and directions 225, 240 and 270 degrees, respectively

As for the characteristic patterns observed for the lateral pontoon motion ranges, also corresponding patterns are present for the strong axis bending moments, as given in figure 6.29. The largest bending moments are found in the northern end of the bridge for the wave direction 240 degrees. For this direction, the pontoons have the previously mentioned displacement pattern where every second lateral pontoon displacement is significantly larger, which induces large strong axis bending moments. The magnitudes of the lateral pontoon motions for the waves from 240 degrees are smaller than those for 270 degrees. However, for the latter, the bridge girder moves more evenly in the same direction, thus resulting in smaller bending moments. This is seen in figure 6.35.

The direction 225 degrees is observed to impose large strong axis bending moments in the part of the bridge holding the first 6 pontoons. This is reasonable as it corresponds to the pontoons having the largest lateral movements at this part of the bridge.

Shear Forces

The maximum and minimum shear forces are as expected distributed along the bridge girder in similar patterns as the bending moments. For the vertical shear forces, figure 6.30, it is seen that the largest values for the direction 225 degrees and some values in the southern end for the direction 240 degrees are found at the midspans.

Since the forces are stored only for the nodes at the midspans and the girder-column intersections, the true largest values can be slightly shifted towards one side. This can be the case for the spans which have large differences between the shear forces in the given span's intersections, such that small underestimations of the maxima can be present.

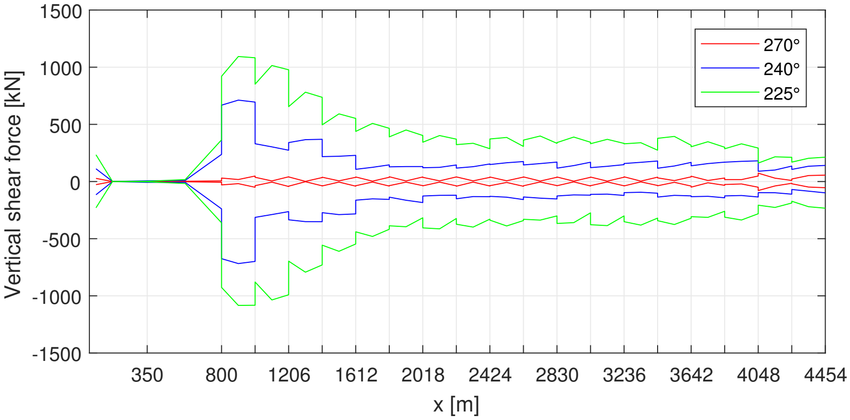

Figure 6.30: Dynamic max and min vertical shear forces in regular waves with H = 3 m, T = 6 s and directions 225, 240 and 270 degrees, respectively

For the shear forces in the lateral direction, as given in figure 6.31, the non-linear shape of the shear forces in the spans are less obvious, since the gravitational acceleration does not contribute in this direction. On the other hand, the steps of the shear forces in the girder-column intersections are larger. This is because the relative magnitudes of the lateral pontoon motions are larger than for the vertical direction.

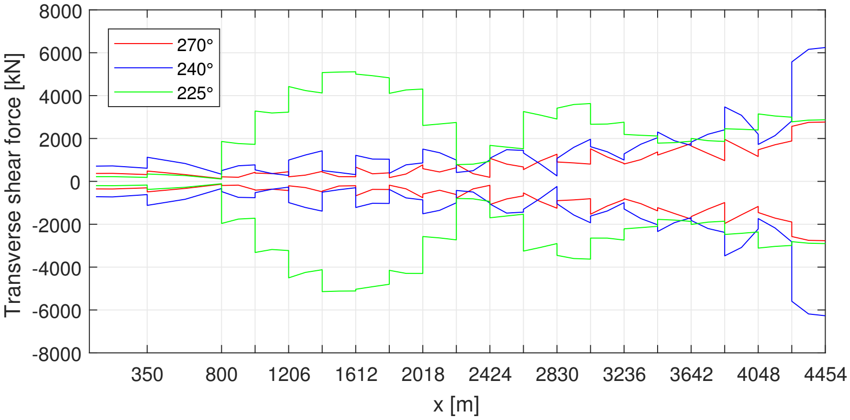

Figure 6.31: Dynamic max and min shear forces transverse to bridge axis in regular waves with H = 3 m, T = 6 s and directions 225, 240 and 270 degrees, respectively

Axial Forces

From figure 6.32 it is seen that the tower is not absorbing axial forces from the bridge girder. By also studying the plots of the vertical and lateral bridge girder motions and strong and weak axis bending moments, the approximate boundary conditions are proved to function as intended.

For the wave direction 270 degrees, it is clear that the axial forces are small compared to the other directions, as well as close to evenly distributed along the bridge girder. This can be explained by the fact that the surge motions of the pontoons are small, as well as due to the pontoons moving in phase and the displacements of the bridge girder being small compared to its dimensions.

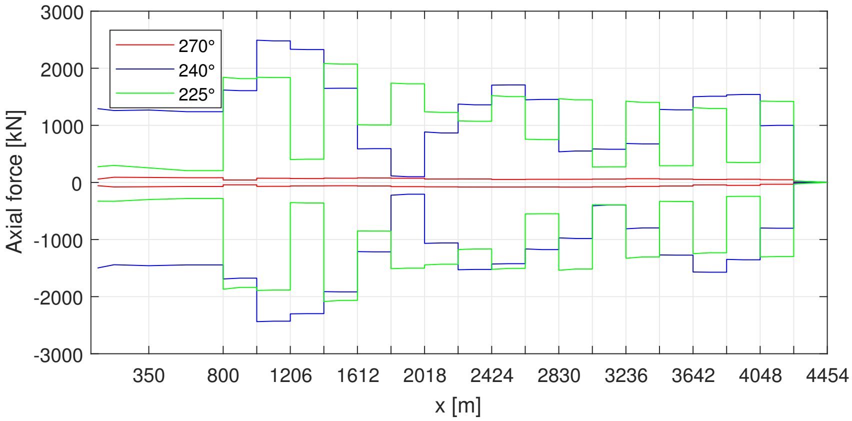

Figure 6.32: Dynamic max and min axial forces in regular waves with H = 3 m, T = 6 s and directions 225, 240 and 270 degrees, respectively

For the other two directions, the axial forces are seen to vary significantly along the bridge girder. This is because the pontoons do not move in phase for these directions, but with constant relative phase. By running several waves with different directions, respectively, and thereby changing the phase of the pontoon motions, the average maximum and minimum values would be more continuous along the bridge.

Torsional Moments

Also for the maximum and minimum torsional moments, large differences are present between the respective wave directions. It should be recalled that the torsional moment is negligible in the static configuration. Common for the responses is that the torsional moments are small in the cable-stayed bridge for all wave directions, due to the large lateral distances of the stay cable intersections in the bridge girder.

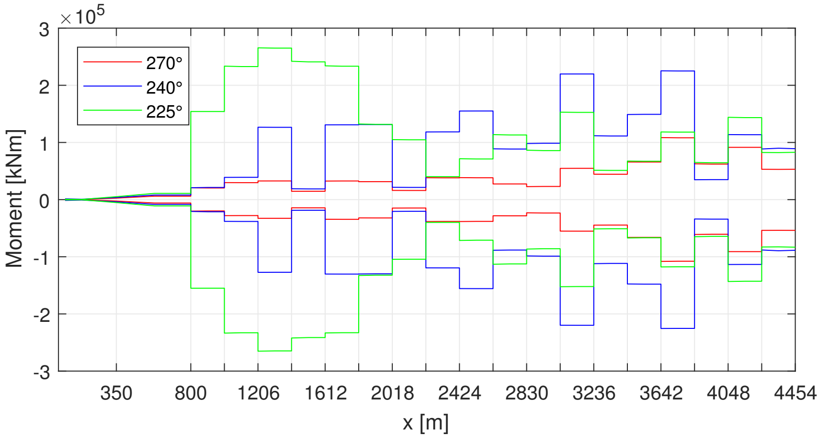

Figure 6.33: Dynamic max and min torsional moments in regular waves with H = 3 m, T = 6 s and directions 225, 240 and 270 degrees, respectively

The direction 240 degrees proves to induce the largest torsional moments in the northern half of the bridge, despite the lateral pontoon motions being larger for the normal direction. This is reasonable due to the large differences between the maximum and minimum displacements for the adjacent pontoons for this wave direction.

Also the wave direction 225 degrees induces larger extreme values of the torsional moments in the northern end than the wave direction normal to the bridge. This can be explained by examining the extremes of the lateral girder motions relative to the pontoon motions. For the normal wave direction, these motions are closer in magnitude.

The lateral motions of the pontoons relative to the motions of the bridge girder are therefore seen to drive the torsional moments in the bridge girder. This is clearly the case for the largest torsional moments, i.e. for the wave direction 225 degrees in the southern part of the bridge. For this part, the pontoons have large lateral motions and the girder small lateral motions.

Bridge Girder Accelerations

The final set of properties to be included in the directional screening analysis are the bridge girder accelerations in the horizontal and vertical directions.

For all figures presented in the dynamic results section, the responses have been obtained for the nodes located in the girder-column intersections and in the midspans. For the other properties investigated the maxima and minima have been located at the girder-column intersections. The exceptions are the shear forces, but here the potential underestimations from the values at the midpoints or intersections are small.

For the bridge girder accelerations, significant underestimations are present for the main span in the cable-stayed bridge. This is because of the reduced rotational stiffness about the first girder-column intersection, as discussed in section 6.2.1. This allows larger deflections of the girder, as well as the extreme value being closer to the mentioned girder-column intersection.

For the floating bridge spans the underestimations are minimal because of the close to evenly distributed loads, including inertia effects, about the girder-column intersections. From both figure 6.34 and 6.35 it is seen that the highest possible accelerations of the main span in the cable-stayed bridge are lower than the overall largest acceleration in the respective directions, such that re-running analyses with increased details of the main span accelerations were not deemed necessary.

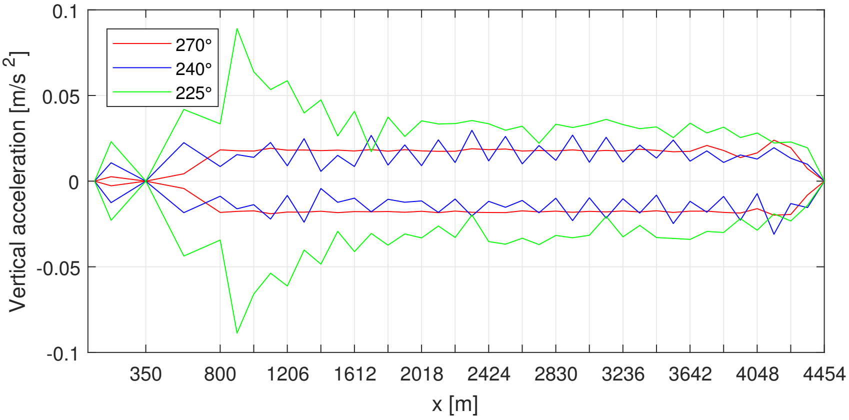

Figure 6.34: Dynamic max and min vertical accelerations of the bridge girder in regular waves with H = 3 m, T = 6 s and directions 225, 240 and 270 degrees, respectively

From figure 6.34 there are seen different patterns in the maximum and minimum vertical accelerations for the different directions. For the direction 225 degrees most of the maximum accelerations for the floating bridge spans are found at the girder-column intersections, while for all spans for the direction 240 degrees, the maxima are found at the midspans. This can be explained by the phase differences for the pontoon motions, where the former implies that adjacent pontoons oscillate at least one-quarter period out of phase and the latter that adjacent pontoons oscillate less than one-quarter period out of phase. This can be verified by geometrical considerations. For the direction 270 degrees, the maximum and minimum accelerations are close to constant along the bridge, which can be explained by the pontoons moving perfectly in phase and with small deviations in amplitude.

The girder lateral accelerations, as given in figure 6.35, can also be explained by comparing relative phase and amplitudes of the pontoon motions and will therefore not be done in further detail.

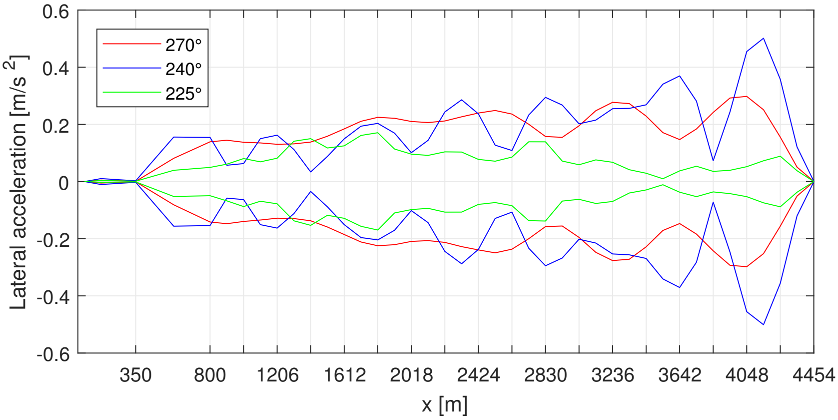

Figure 6.35: Dynamic max and min lateral accelerations of the bridge girder in regular waves with H = 3 m, T = 6 s and directions 225, 240 and 270 degrees, respectively

In table 6.6 the largest accelerations of the bridge girder for the wave directions examined are compared with criteria specified by the NPRA. The criteria are given for a 1-year storm, defined by a significant wave height of 1.5 metres, a peak period of 6 seconds, wave direction 270 degrees and wind from the same direction [2]. The results can therefore not be directly compared, but quantifies the magnitudes observed.

Table 6.6: Maximum girder accelerations compared to criterion specified by the NPRA [2]

Motion	Criterion [m/s^2]	Max NPRA [m/s^2]	Max direction screening [m/s^2]
Vertical acceleration	0.5	0.7	0.089
Lateral acceleration	0.3	0.44	0.50

For the examined wave directions, the extreme values of the vertical accelerations are seen to be small compared to the criterion. This is reasonable since dynamic wind was found to govern the vertical accelerations in the reference report [2].

The extremes of the lateral accelerations are larger than both the criterion and the value obtained by the NPRA. For the direction 270 degrees, the extremes are within the criterion when the accelerations are calculated at mid-spans and girder column intersections. From the shape of this plot, the largest value is expected to be slightly underestimated.

Chapter 7

Conclusion

From the analyses carried out in this thesis, it is clear that a large number of aspects have not been included, as the purpose has been to illustrate modelling aspects and calculation procedures, hence not verifying the bridge concept in detail. However, during this procedure several characteristics of the response have been found.

From the static analysis, it was shown that the vertical displacements of the pontoons due to 70 % of the characteristic distributed traffic loads were well within the criterion specified by the project team for the concept. The pontoons also proved to have significant excess buoyancy, where the pontoons not holding the catenary mooring lines needed a minimum of 21.3 % of their self-weight in ballast to obtain their design draft. Additionally, the self-weight of the pontoon is a large fraction of the pontoon displacement, i.e. 11 300 tons/18 300 tons $\approx$ 62 %. The former results and observations make it clear that from a hydrodynamic point of view, the pontoons are not fully optimised with respect to the global response in the structure.

In the eigenvalue analyses, an important limitation was identified in the calculation codes in SIMO-RIFLEX. The fact that the catenary mooring systems were not properly included in the eigenvalue calculations introduced challenges in the evaluations of the original bridge model. However, the implementation of a linearised mooring system for a second model led to good agreement for the eigen periods and mode shapes compared to those obtained by the NPRA, where the first 30 eigen periods were differing with a mean value of 3.9 % when only the infinite-frequency added mass matrix was considered. By updating the added mass at the periods specified, differences of less than about 2 % were obtained, implying that the stiffness and mass properties of the bridge girder and pontoons, as well as the boundary conditions, were modelled correctly. This also implies that the simplification of the tower mainly affects the response locally.

Furthermore, the eigenvalue calculations revealed several modes that can be triggered by environmental loads. Laterally dominated modes at high periods with negligible damping, which can be important for the response in slowly varying wind and second order difference frequency wave forces, and laterally dominated modes close to the peak period for the 100-year wind waves were identified. Additionally, modes dominated by longitudinal pontoon motions close to this period were found, possibly important for dynamic weak axis bending moments in the high bridge. These findings make it evident that thorough assessments of the bridge in the actual environmental conditions must be performed to fully evaluate the concept.

However, the results from the dynamic analyses in regular waves showed important response patterns, where some were seen to be related to the modes identified. As the wave directions were put closer to the bridge longitudinal axis, displacement patterns related to the pendulum dominated modes were present. This led to large weak axis bending moments in the high bridge relative to the remaining part of the bridge. Despite this, the magnitudes of the dynamic weak axis bending moments were found to be small compared to the static bending moments, i.e. less than about 15 % for the wave conditions examined, implying possible room for girder height to span length ratio optimisation.

Chapter 8

Recommendations for Further Work

To fully assess the bridge concept there are a lot of aspects that need to be accounted for, such as stress analyses, fatigue, accidental loads, etc. Within the aspects examined in this thesis, the model is considered a good starting point for further analyses.

Firstly, the differences between the eigen periods for higher modes for both models in SIMO-RIFLEX and those obtained by the NPRA should be further evaluated.

Furthermore, extensive analyses for examining for linearity in response should be done if linear time domain analyses are to be performed. Care should be taken for which conditions this is reasonable to assume, especially regarding the effect of the non-linear mooring system. The reason for the asymmetry in the vertical pontoon motions should also be further assessed.

The main recommendation for further work is to perform dynamic analyses in the actual environmental conditions for Bjørnafjorden. This will include analyses in wind-driven waves and swell waves, both long- and short-crested. These should also be evaluated in combination with wind. Emphasis should be put on further studies of the items stated in the conclusion, where dynamic amplification of the response related to the identified modes should be thoroughly assessed. Due to extremely long simulation time, the dynamic analyses were limited to regular waves in this thesis.

In addition, the modelling of the pontoons can be done in more detail by including second order forces and quadratic drag forces. These can be important for resonance in response for the first laterally dominated modes. Finally, also the modelling of the bridge structure could have been done in more detail: the exact properties of the tower and the vertical curvature of the bridge girder in the high bridge were not included.

Bibliography

[1] Statens Vegvesen. *The E39 Coastal Highway Route.* Accessed from: `https://www.vegvesen.no/en/roads/Roads+and+bridges/Road+projects/e39coastalhighwayroute`

[2] Larsen, P. N. (2016) *Straight bridge concept.* Accessed from: `https://www.vegvesen.no/_attachment/1605065/binary/1145263?fast_title=Bj%C3%B8rnafjorden+Sideforankret+flytebru+-+oppsumering+av+analyser.pdf`

[3] Washington State Department of Transportation (2017). *SR 520 Floating Bridge and Landings Project.* Accessed from: `http://www.wsdot.wa.gov/sites/default/files/2017/05/16/SR520-Booklet-FB042017.pdf`

[4] Statens Vegvesen. *E39 Stord- Os (Hordfast) blir 8 milliardar billigare.* Accessed from: `https://www.vegvesen.no/Europaveg/e39stordos/nyhetsarkiv/e39-stord-os-hordfast-blir-8-milliardar-billigare`

[5] Statens Vegvesen (2012). *Delprosjekt Fjordkryssing.* Accessed from: `https://www.vegvesen.no/_attachment/435447/binary/731803`

[6] Lwin, M. M. (2000). *Floating Bridges, Bridge Engineering Handbook.* CRC Press

[7] Moe, G. (1997). *Design philosophy of floating bridges with emphasis on ways to ensure long life.* Accessed from: `https://link.springer.com/article/10.1007/BF02489809?no-access=true`

[8] *Bergsøysundbrua - 153 SVV NVP Brunr 15-2221.* Accessed from: `https://kulturminnesok.no/minne/?queryString=https://data.kulturminne.no/askeladden/lokalitet/110598`

[9] Statens Vegvesen (1994). *Nordhordalandsbrua.* Accessed from: `https://www.nb.no/items/URN:NBN:no-nb_digibok_2014081906042`

[10] NRK. *Photo of the Norhordaland Bridge.* Accessed from: `https://www.nrk.no/hordaland/_-nordhordlandspakken-har-falt-1.12218946`

[11] Statens Vegvesen. *Rogfast.* Accessed from: `https://www.vegvesen.no/Europaveg/e39rogfast/Nyhetsarkiv/na-er-vi-igang-med-verdas-lengste-og-djupaste-undersjoiske-tunnel`

[12] Larsen, P. N. (2016) *Curved bridge concept.* Accessed from: `https://www.vegvesen.no/_attachment/1605060/binary/1145259?fast_title=Bj%C3%B8rnafjorden+Endeforankret+flytebun+-+Oppsumering+av+analyser.pdf`

[13] Statens Vegvesen. *Fjordkryssing - Bjørnafjorden.* Accessed from: `https://www.vegvesen.no/Europaveg/e39stordos/fjordkryssing-bjornafjorden`

[14] British Standards (2003). *Eurocode 1: Actions on structures — Part 2: Traffic loads on bridges.* Accessed from: `https://www.rail.co.il/Development/Documents/gsharim/02EN1991_BS%20EN%201991-2_2003_Eurocode%201_Actions%20on%20structures%20-%20Part2_Traffic%20load%20and%20briges.PDF`

[15] Det Norske Veritas (2010). *Recommended practice, DNV-RP-C205* Accessed from: `https://rules.dnvgl.com/docs/pdf/dnv/codes/docs/2010-10/rp-c205.pdf`

[16] Pettersen, B. (2007). *Marin teknikk 3: Hydrodynamikk.* Department of Marine Technology, NTNU

[17] Statens vegvesen (2017). *Design Basis Bjørnafjorden Side- and end anchored floating bridge.* Accessed from: `https://www.vegvesen.no/_attachment/2088822/binary/1221883?fast_title=Bj%C3%B8rnafjorden+design+basis+rev.pdf`

[18] Faltinsen, O. M. (1993). *Sea Loads On Ships And Offshore Structures.* Cambridge University Press

[19] SINTEF Ocean (2017). *RIFLEX 4.10.1 Theory Manual*

[20] Amdahl, J., Larsen C. M, Syvertsen, K, et al. (2010). *Compendium in TMR 4167: Marine Technology 2.* Department of Marine Technology, NTNU

[21] Moan, T. (2003). *TMR 4190 Finite Element Modelling and Analysis of Marine Structures.* Department of Marine Technology, NTNU

[22] Langen, I. and Sigbjørnsson, R. (1979). *Dynamisk analyse av konstruksjoner.* Tapir.

[23] SINTEF Ocean (2017). *SIMO 4.10.1 Theory Manual*

[24] COWI, Johs Holt, Aas-Jakobsen and Global Maritime (2016). *Bilag B - Input to NovaFrame and OrcaFlex*

[25] Larssen, R. M., Larsen, P. N., Strømsem, K. and Sørby, B. (2016). *Design Basis - RAP-GEN-001.* Accessed from: `https://www.vegvesen.no/_attachment/1605052/binary/1145248?fast_title=Bj%C3%B8rnafjorden+Flytebru+Design+Basis.pdf`

[26] Statens vegvesen (2016). *Floating bridge - E39 Bjørnafjorden.* Accessed from: `https://www.vegvesen.no/_attachment/1545428/binary/1135143?fast_title=14+Flytebru.pdf`

[27] DNV GL (2015). *Sesam User Mannual - Wadam*

[28] Larsen, P. N. (2016). *Straight bridge concept - Appendices.* Accessed from: `https://www.vegvesen.no/_attachment/1605064/binary/1145262?fast_title=Bj%C3%B8rnafjorden+Sideforankret+flytebru+-+vedlegg+til+oppsumering+av+analyser.pdf`

[29] Statens Vegvesen (2014). *Håndbok N400 Bruprosjektering* Accessed from: `https://www.vegvesen.no/_attachment/115441`

[30] Myrhaug, D. (2004). *Compendium in TMR4180 Marine Dynamics.* Akademika forlag

[31] SINTEF Ocean (2017). *RIFLEX 4.10.1 User Guide*

Appendix A

Hydrodynamic Results for the Pontoon

A.1 Added Mass

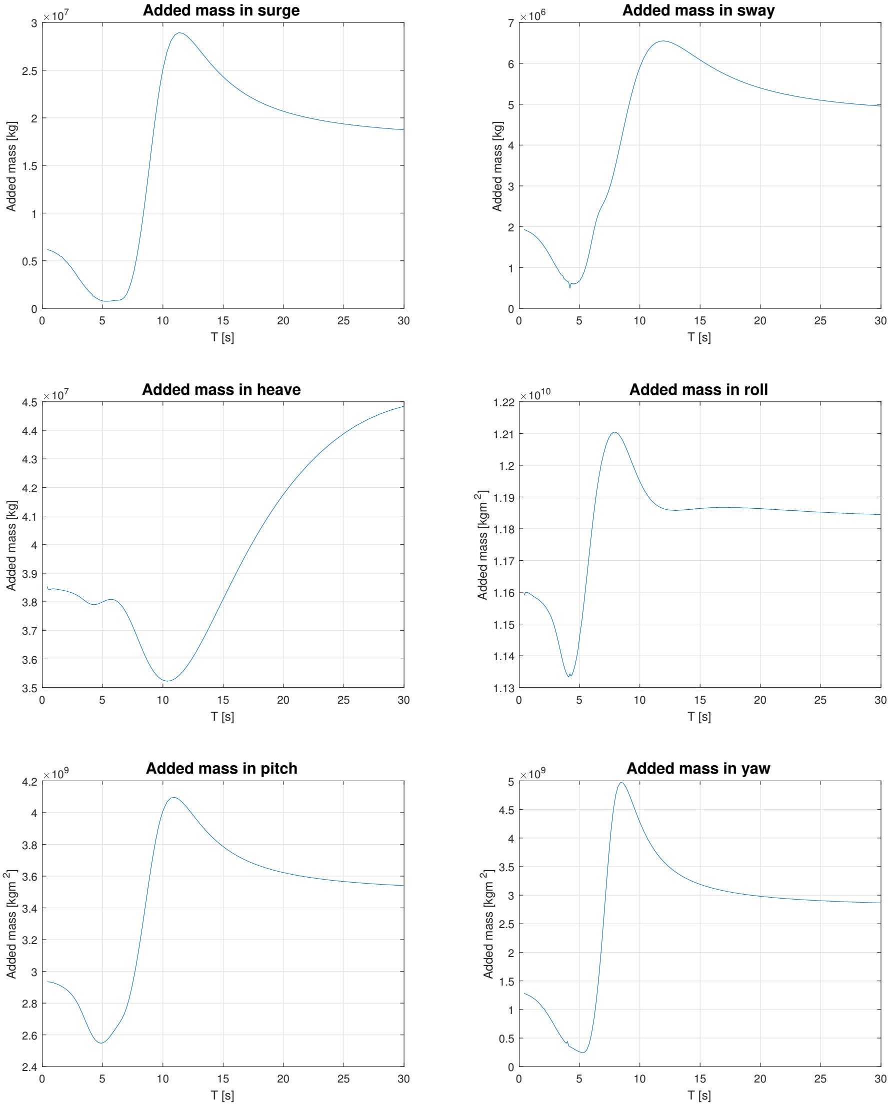

Figure A.1: Radiation added mass for pontoon at mesh size 0.5 m x 0.5 m

A.2 Radiation damping

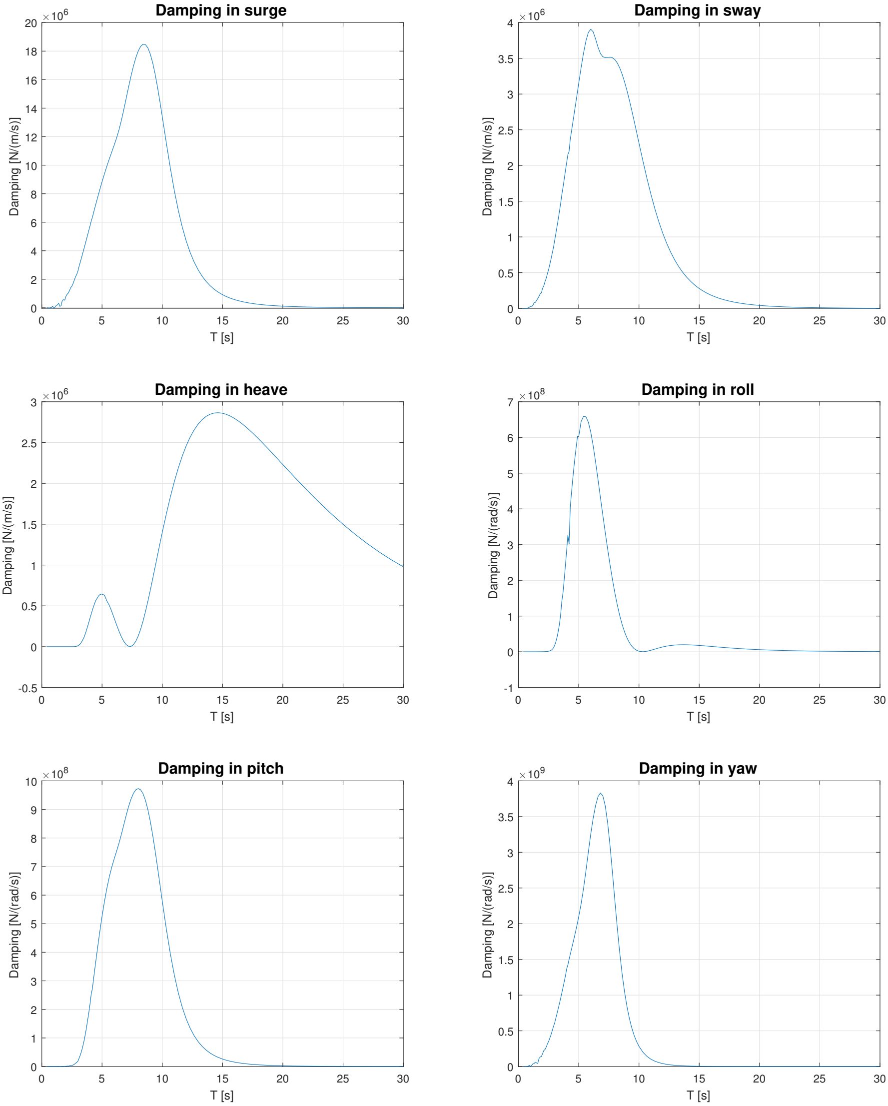

Figure A.2: Radiation damping for pontoon at mesh size 0.5 m x 0.5 m

A.3 First Order Wave Force Transfer Functions

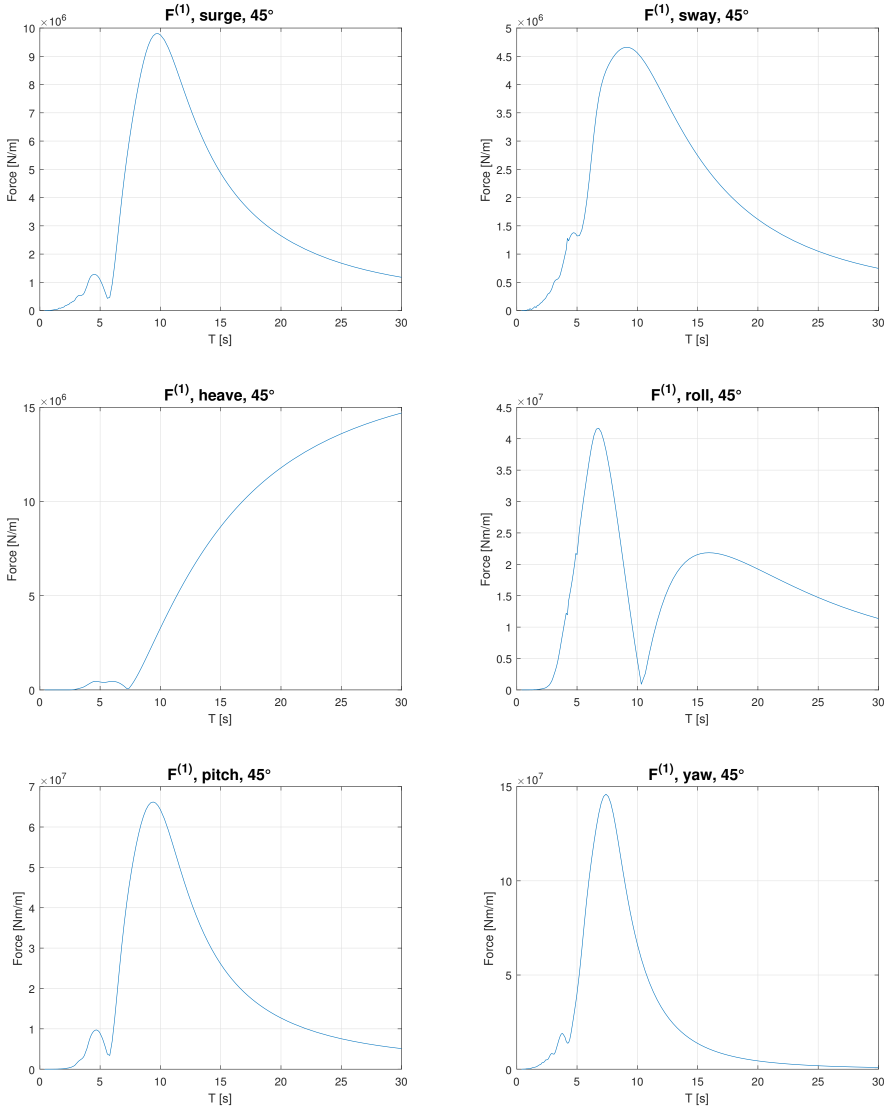

Figure A.3: First order wave force transfer functions for a wave direction of 45 degrees for pontoon at mesh size 0.5 m x 0.5 m

Appendix B

Eigenvalue Analysis

B.1 The first 75 eigen periods compared to values obtained by the NPRA

	NPRA	Cat. mooring		Lin. mooring		Added mass iterated		
Mode	T [s]	T [s]	Diff [%]	T [s]	Diff [%]	T [s]	Diff [%]	T$_A[s]$
1	78.25	74.66	−4.7	74.83	−4.5	77.52	−0.9	78.25
2	71.21	68.23	−4.3	68.48	−3.9	70.92	−0.4	78.25
3	40.78	39.85	−2.3	38.94	−4.6	40.32	−1.1	78.25
4	32.48	31.51	−3.0	30.91	−5.0	31.95	−1.6	78.25
5	23.44	22.72	−3.1	22.49	−4.1			
6	17.69	16.95	−4.3	16.90	−4.6			
7	14.09	16.24	14.2	13.16	−6.8	14.22	0.9	14.09
8	14.09	16.23	14.1	12.33	−13.3	13.82	−2.0	14.09
9	13.06	16.23	21.6	12.15	−7.3			
10	11.45	16.22	34.5	11.59	1.2			
11	11.32	16.22	35.6	11.57	2.2			
12	10.92	16.22	39.1	11.54	5.5	11.09	1.5	10.88
13	10.89	13.33	20.1	11.54	5.8	11.06	1.5	10.88
14	10.88	13.10	18.5	11.49	5.4	11.03	1.4	10.88
15	10.87	13.08	18.5	11.45	5.2	11.01	1.3	10.88
16	10.87	13.08	18.4	11.29	3.8	10.99	1.1	10.88
17	10.84	13.08	18.7	11.11	2.4	10.97	1.2	10.88
18	10.76	13.07	19.4	11.04	2.6	10.85	0.8	10.88
19	10.66	13.07	20.3	11.01	3.3	10.83	1.6	10.88
20	10.50	13.07	21.8	10.84	3.2	10.72	2.1	10.88

	NPRA	Cat. mooring		Lin. mooring	
Mode	T [s]	T [s]	Diff [%]	T [s]	Diff [%]
21	10.32	13.06	23.5	10.55	2.2
22	10.02	13.06	26.4	10.26	2.4
23	9.79	13.06	28.6	10.23	4.4
24	9.73	13.06	29.2	9.84	1.2
25	9.51	13.06	31.5	9.51	0.0
26	9.08	12.66	32.9	9.50	4.5
27	8.85	12.13	31.2	9.10	2.8
28	8.61	11.73	30.7	8.70	1.0
29	8.33	11.68	33.5	8.64	3.7
30	8.21	11.63	34.4	8.30	1.1
31	7.84	11.58	38.6	8.16	4.0
32	7.62	11.54	40.9	8.02	5.2
33	7.45	11.48	42.6	7.65	2.7
34	7.08	11.35	46.3	7.52	6.1
35	6.49	11.25	53.7	7.08	8.7
36	6.42	11.22	54.4	6.71	4.4
37	6.18	11.19	57.6	6.23	0.8
38	5.65	10.85	63.1	6.07	7.2
39	5.41	10.60	64.8	6.01	10.6
40	5.04	10.44	69.8	5.54	9.5
41	4.80	10.25	72.4	5.43	12.2
42	4.73	9.94	71.0	5.33	11.9
43	4.54	9.79	73.3	4.98	9.3
44	4.31	9.56	75.7	4.76	9.9
45	4.18	9.17	74.8	4.69	11.6
46	4.11	8.76	72.2	4.59	11.0
47	4.04	8.71	73.3	4.35	7.5
48	3.85	8.69	77.2	4.27	10.3
49	3.78	8.69	78.7	4.16	9.5
50	3.76	8.69	79.2	4.07	7.9
51	3.68	8.69	81.0	4.07	10.0
52	3.46	8.66	85.8	3.94	12.9
53	3.43	8.65	86.4	3.82	10.8
54	3.36	8.36	85.4	3.76	11.3
55	3.30	8.32	86.4	3.67	10.7
56	3.20	8.32	88.9	3.54	10.0
57	3.01	8.32	93.7	3.48	14.4
58	3.00	8.32	94.0	3.39	12.2
59	2.84	8.32	98.2	3.39	17.6
60	2.67	8.32	102.8	3.20	18.1
61	2.65	8.21	102.4	3.19	18.5
62	2.54	8.08	104.3	3.18	22.3
63	2.40	7.80	105.9	3.07	24.5
64	2.35	7.68	106.3	3.06	26.4
65	2.25	7.60	108.6	3.06	30.4
66	2.18	7.60	110.8	3.06	33.5
67	2.09	7.60	113.7	3.03	36.7
68	2.06	7.60	114.7	3.02	37.7
69	2.04	7.59	115.3	2.95	36.3
70	2.02	7.59	116.0	2.94	37.2
71	1.94	7.59	118.6	2.93	40.7
72	1.93	7.59	118.9	2.92	41.0
73	1.93	7.59	118.9	2.91	40.3
74	1.86	7.57	121.1	2.90	43.6
75	1.77	7.45	123.2	2.84	46.4

B.2 Mode Shape Plots

Vertical grid lines at tower and at initial locations of girder-column intersections

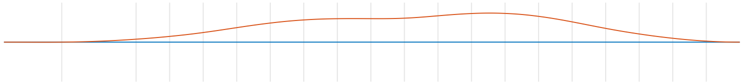

Mode 1, xy-plane

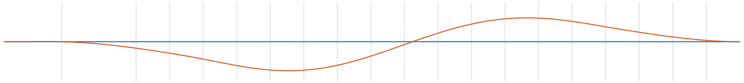

Mode 2, xy-plane

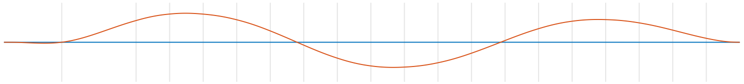

Mode 3, xy-plane

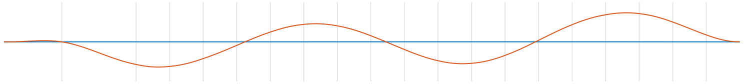

Mode 4, xy-plane

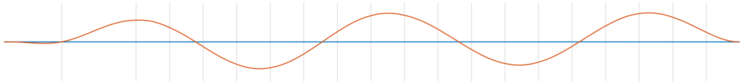

Mode 5, xy-plane

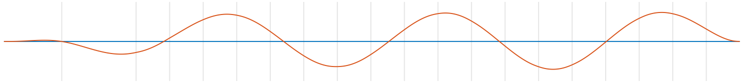

Mode 6, xy-plane

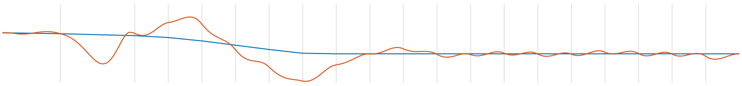
Mode 7, xz-plane

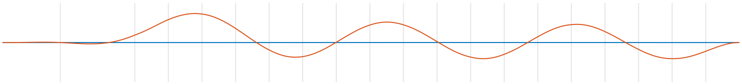
Mode 8, xy-plane

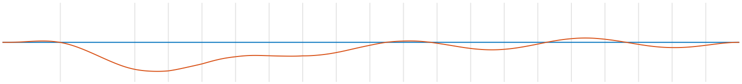
Mode 9, xy-plane


Mode 10, xz-plane

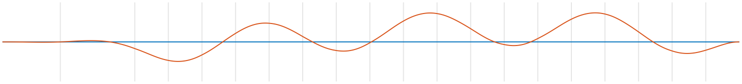
Mode 11, xy-plane

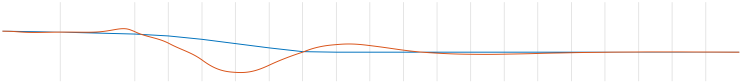
Mode 12, xz-plane

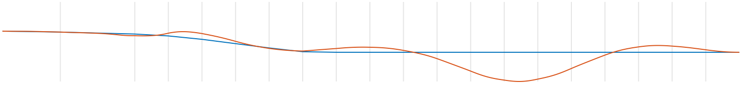
Mode 13, xz-plane

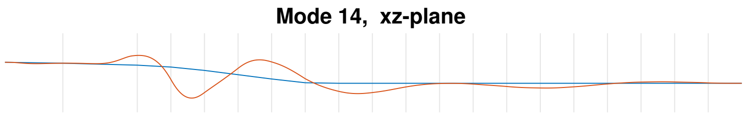
Mode 14, xz-plane

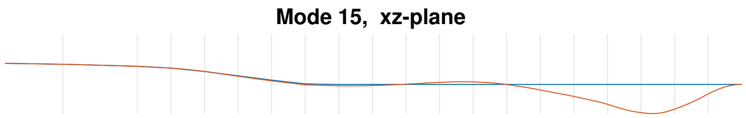
Mode 15, xz-plane

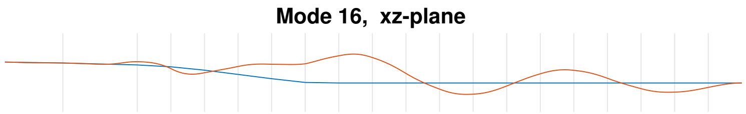
Mode 16, xz-plane

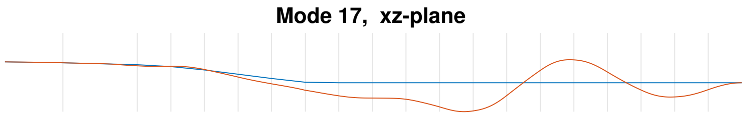
Mode 17, xz-plane

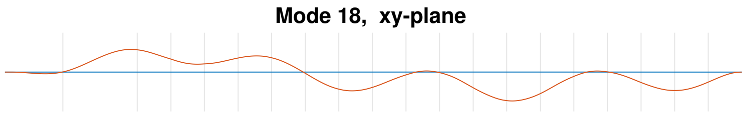
Mode 18, xy-plane

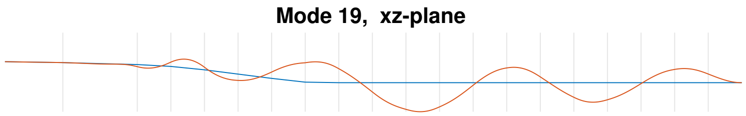
Mode 19, xz-plane

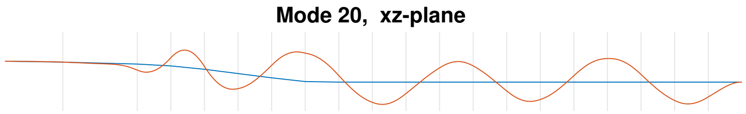
Mode 20, xz-plane

Mode 21, xz-plane

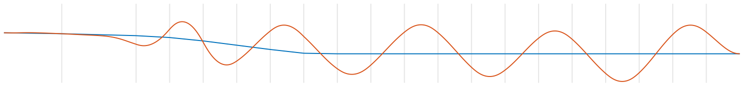

Mode 22, xz-plane

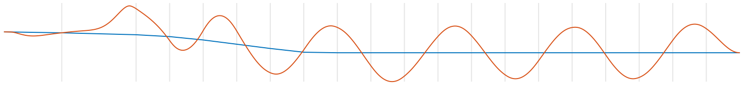

Mode 23, xz-plane

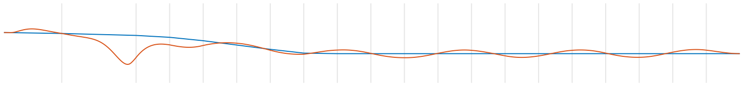

Mode 24, xz-plane

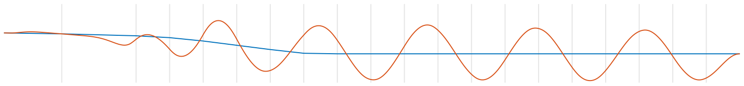

Mode 25, xy-plane

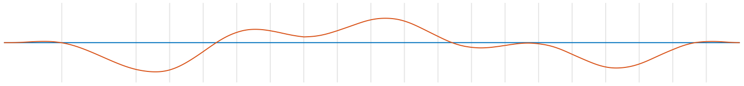

Mode 26, xz-plane

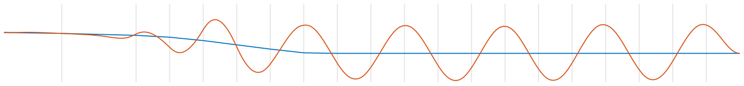

Mode 27, xy-plane

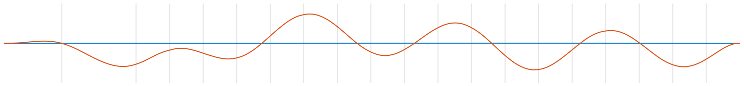

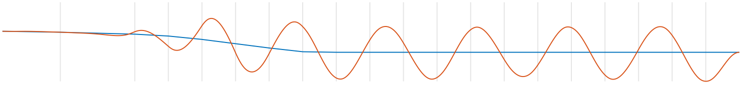
Mode 28, xz-plane

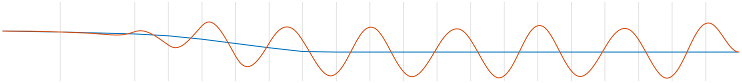
Mode 29, xz-plane

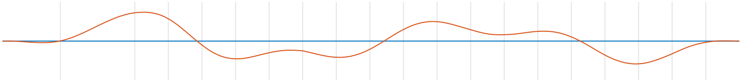
Mode 30, xy-plane

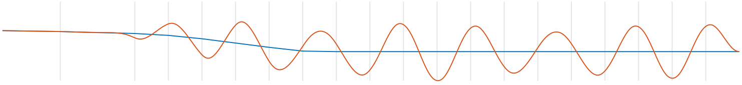
Mode 31, xz-plane

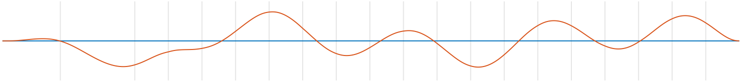
Mode 32, xy-plane

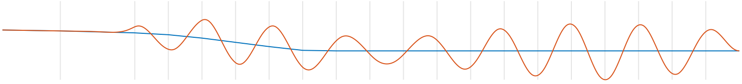
Mode 33, xz-plane

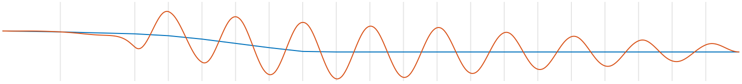
Mode 34, xz-plane

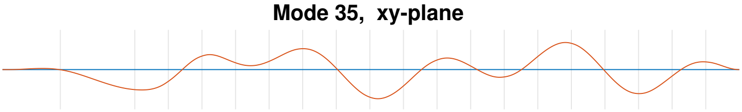
Mode 35, xy-plane

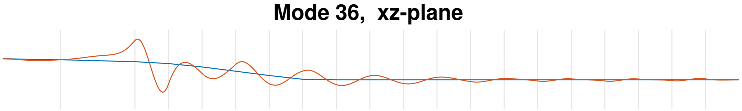
Mode 36, xz-plane

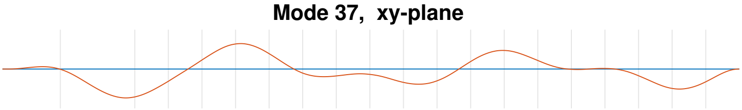
Mode 37, xy-plane

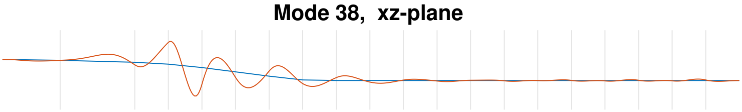
Mode 38, xz-plane

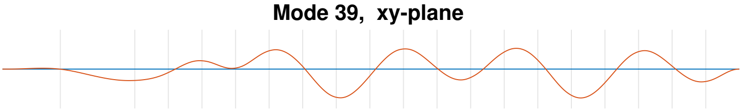
Mode 39, xy-plane

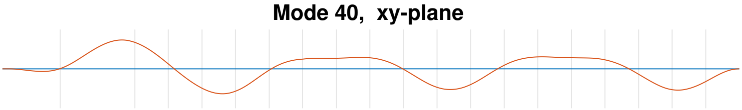
Mode 40, xy-plane

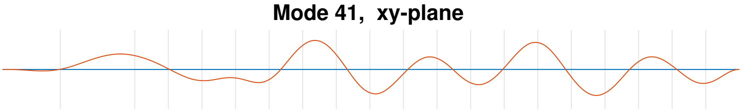
Mode 41, xy-plane

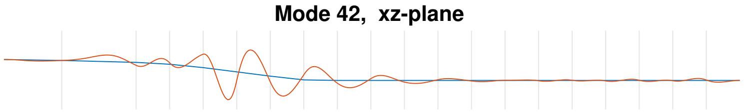
Mode 42, xz-plane

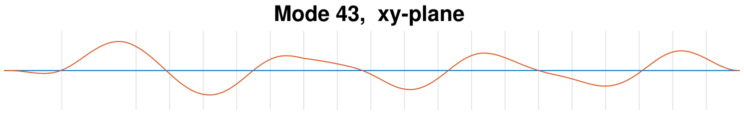
Mode 43, xy-plane

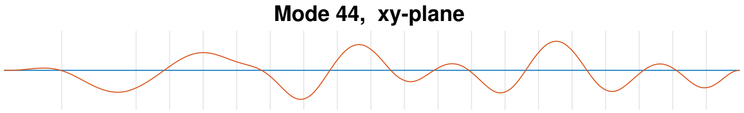
Mode 44, xy-plane

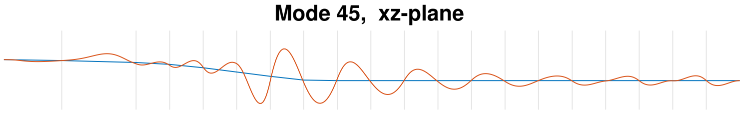
Mode 45, xz-plane

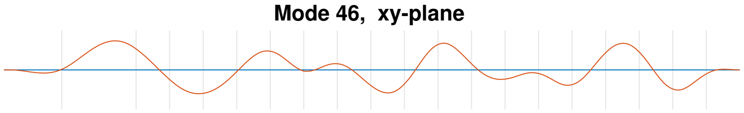
Mode 46, xy-plane

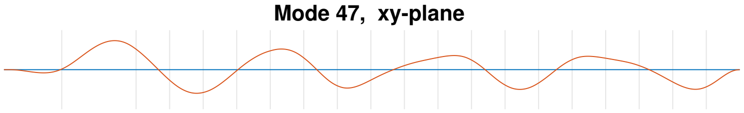
Mode 47, xy-plane

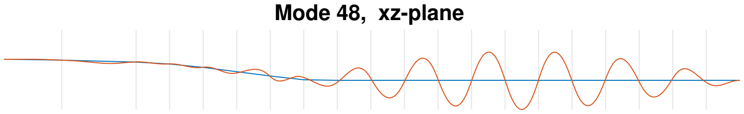
Mode 48, xz-plane

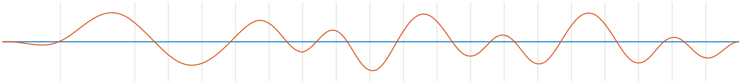

Mode 49, xy-plane

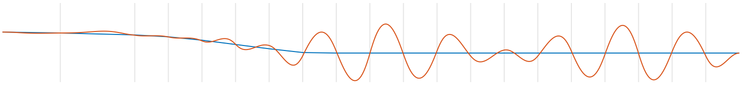

Mode 50, xz-plane

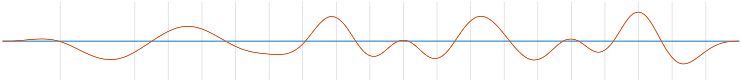

Mode 51, xy-plane

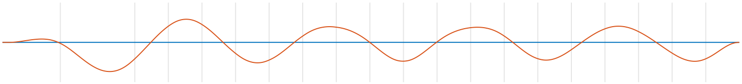

Mode 52, xy-plane

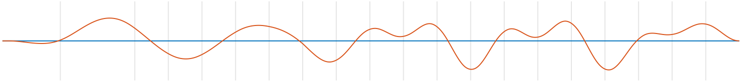

Mode 53, xy-plane

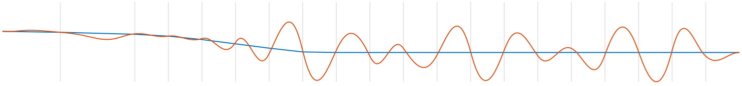

Mode 54, xz-plane

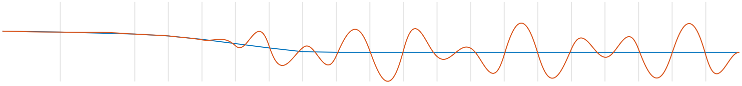

Mode 55, xz-plane

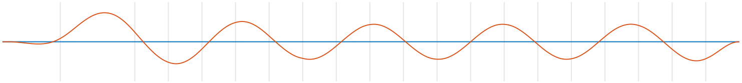
Mode 56, xy-plane

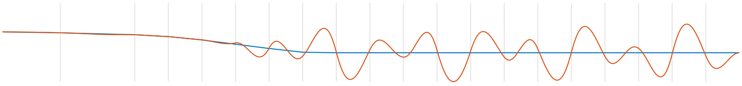
Mode 57, xz-plane

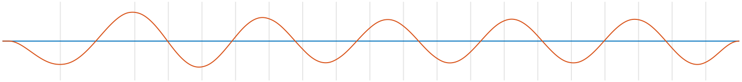
Mode 58, xy-plane

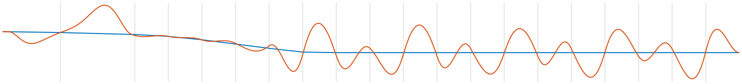
Mode 59, xz-plane

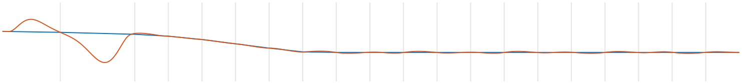
Mode 60, xz-plane

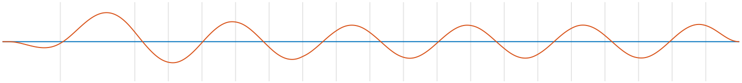
Mode 61, xy-plane

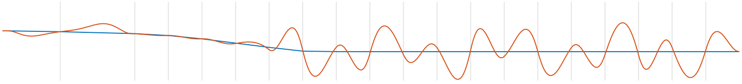
Mode 62, xz-plane

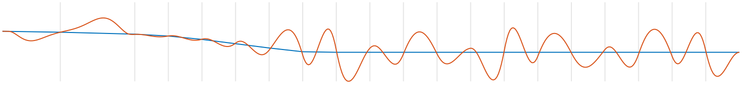

Mode 63, xz-plane

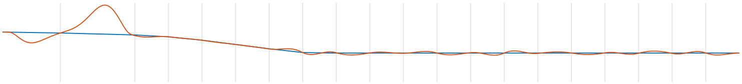

Mode 64, xz-plane

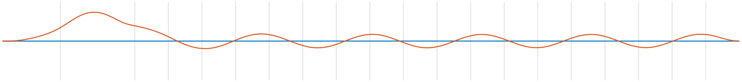

Mode 65, xy-plane

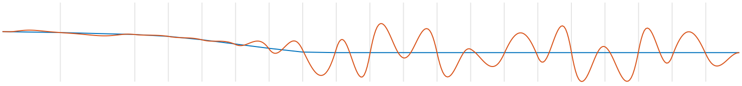

Mode 66, xz-plane

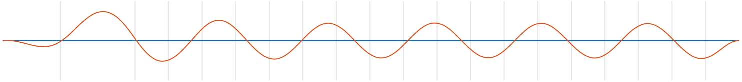

Mode 67, xy-plane

Mode 68, xy-plane

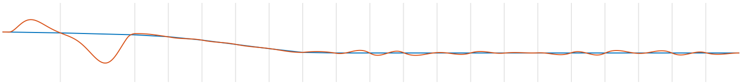

Mode 69, xz-plane

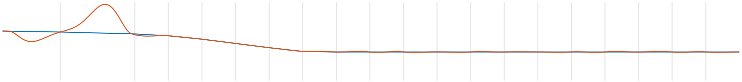

Mode 70, xz-plane

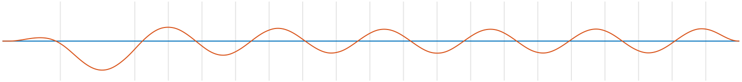

Mode 71, xy-plane

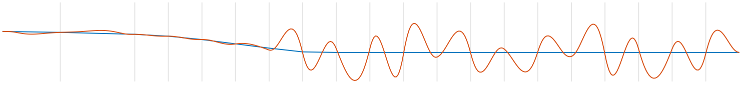

Mode 72, xz-plane

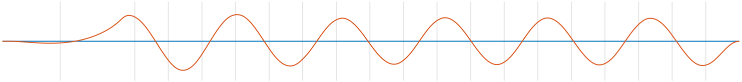

Mode 73, xy-plane

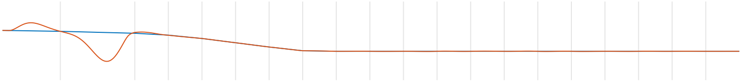

Mode 74, xz-plane

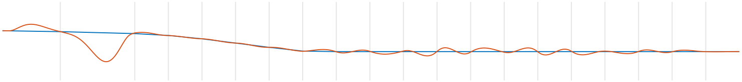

Mode 75, xz-plane